LATVIAN
JOURNAL
of
PHYSICS
and TECHNICAL
SCIENCES

ISSN 0868 - 8257

3

(Vol. 59)

2022

CONTENTS

LATVIAN JOURNAL of PHYSICS and TECHNICAL SCIENCES

LATVIJAS FIZIKAS un TEHNISKO ZINĀTŅU ŽURNĀLS

ЛАТВИЙСКИЙ ФИЗИКО-ТЕХНИЧЕСКИЙ ЖУРНАЛ

Published six times a year since February 1964
Iznāk sešas reizes gadā kopš 1964. gada februāra
Выходит шесть раз в год с февраля 1964 года

3 (Vol. 59) • **2022**

RĪGA

Language Editor: O. Ivanova
Computer Designer: I. Begicevs

INDEXED (PUBLISHED) IN

www.scopus.com
www.sciendo.com
EBSCO (Academic Search Complete, www.epnet.com), INSPEC (www.iee.org.com).
VINITI (www.viniti.ru), Begell House Inc/ (EDC, www.edata-center.com).

Issuers: Institute of Physical Energetics,
Institute of Solid State Physics, University of Latvia
Registration Certificate Number: 000700221

Editorial Contacts:
14 Dzerbenes Street, Riga, LV - 1006
Ph.: + 371 67551732
E-mail: leo@lza.lv
www.fei-web.lv

LATVIAN JOURNAL OF PHYSICS
AND TECHNICAL SCIENCES
2022, N 3

DOI: 10.2478/lpts-2022-0013

MULTIFOCAL NEAR-EYE DISPLAY: TIMING OF OPTICAL DIFFUSER ELEMENTS AND SYNCHRONIZATION TO DLP-BASED PROJECTION MICROUNIT

R. Ruskuls[1], K. Slics[1], R. Ozolins[2], R. Fenuks[3],
E. Linina[3*], K. Osmanis[1], I. Osmanis[1]

[1] Hansamatrix Innovations Ltd., 1 Ziedleju Str., Marupe, LV-2167, LATVIA
[2] Hansamatrix Ventspils Ltd., 1 Ventspils Augsto tehnoloģiju parks,
Ventspils, LV-3602, LATVIA
[3] LightSpace Technologies, 1 Ziedleju Str., Marupe, LV-2167, LATVIA
*e-mail: elza.linina@lightspace3d.com

The paper present the key technical details of a multifocal near-eye display concept. Along with an overview of the basic architecture, a particular implementation that utilises a digital light processing (DLP®) based spatial light modulator as the image source is provided in the study. The investigated approach involves the utilisation of a small-scale volumetric screen formed by a stack of fast-switching optical diffuser elements based on liquid crystal technology. The volumetric screen is illuminated by a rear image projector. To make the whole system functional and small, the challenge lies within the development of integrated control board for the projection modules as well as the synchronization of the DLP® projector image output to the optical diffuser element switching-cycle.

The main difficulty of the development process is accounting for the peculiarities of in-house developed diffuser elements and the off-the-shelf DLP®, which is the main focus of this paper. There is no direct control over the full set of DLP® operational parameters, an indirect method for adjusting frame dead time is proposed, showing that an increase in dead time close to 0.3 ms (from 0.3 ms to 0.6 ms in the particular setup) can be achieved without significantly sacrificing image colour depth or quality. Tuneable dead time mitigates the limitations set by the non-instantaneous switching of liquid crystal diffuser elements as longer dead times allow for the removal of image bleeding between frames.

Keywords: *Digital light processing, digital micromirror device, liquid crystal diffuser, multifocal display, near-eye display.*

1. INTRODUCTION

For decades it has been claimed that virtual reality (VR) and augmented reality (AR) are slowly but surely entering everyday life. Even though its use in everyday life is currently far from what had been imagined in the 1980s, in 2020 AR was removed from the Gartner hype cycle as, according to Gartner, AR has matured so rapidly that it is no longer considered an "emerging technology" [1].

Currently the predominant form of AR is achieved through the use of various smart device-based applications. Through the camera of a smartphone or a tablet, one can visualize interior and exterior design, virtually try on clothing, explore different hairstyle options and make-up products. In the professional front – a medical professional can overlay x-ray or tomography imaging data directly onto a patient's body to more easily interpret visual information. While useful, looking though a screen of a handheld smart device is not convenient nor is it immersive. An alternative to handheld video see-through devices is an optical see-through head-mounted display (OST HMD) commonly referred to as smart glasses [2]. OST HMDs present additional challenges in creating an immersive experience, but improvements in electronic components and computing power over the past years have made such devices more feasible.

For certain applications it is important to be able to view content close-up, but the conventional way of creating a 3D image is relaying on binocular disparity – providing each eye with a different 2D image that is processed together by the brain into a 3D scene [3]. For objects close to the viewer (up to 1 m from the viewer) this presents a problem – the human visual system relies on both vergence and accommodation to determine the distance to an object. In the case of a near-eye display with a single focal plane these cues do not match and this gives rise to a phenomenon known as the vergence-accommodation conflict (VAC) that can cause blurred vision (out-of-focus image), eyestrain, visual fatigue and in some cases even nausea [4], [5]. A straight-forward approach to mitigating the adverse effects of VAC is providing the eye with additional focal planes for content at different depths. This is the type of OST HMD architecture pursued and developed at *LightSpace Technologies* [6].

This paper examines the challenges of integrating the operation of a custom method for creating virtual focal planes (by using liquid crystal switchable diffusers) and an off-the-shelf solution for projecting an image (a DLP microprojection unit provided by *Texas Instruments Inc.*).

2. MATERIALS AND METHODS

Instead of showing image on a single focal plane, multifocal display architecture approximates depth with multiple focal planes, for which either multiple displays are required or a single display can be, for example, mechanically swept. This allows for the splitting of a 3D scene into "slices" of which each is shown on a corresponding focal plane. Consequently, the utilization of even just a few focal planes can substantially mitigate the VAC.

In the case of the proposed display

architecture by *LightSpace Technologies*, it is formed by a stack of liquid-crystal (LC) based optical diffuser elements and a rear microprojector. Essentially it is a tiny volumetric display which is imaged through an eyepiece – thus resulting in multiple virtual focus planes. The optical diffuser elements forming the stack have two distinct optical states – highly transparent and highly scattering. The transparent state virtually does not interfere with the incident visible light due to very low haze values (<0.2 %). In the highly light-scattering state, the LC element acts as an image receiving screen. Thus, a single projection unit (considering image-forming module for one eye) is sufficient to address all image planes time-sequentially. Essentially, the architecture is entirely solid-state and the "scanning" of the projection volume is executed electronically. Key optical characteristics of optical diffuser elements for applications in HMDs have been described previously [7].

Rapid diffuser element switching (<0.8 ms) has been shown previously on a direct-view volumetric display having 20 discrete depth planes [8]. Thus, the challenging component concerning a near-eye display is a microprojector that is as small as possible but with a high enough image refresh rate to support multiple focal planes. For this purpose, the digital light processing (DLP) technology from *Texas Instruments Inc.* was found to be the most fitting. In particular, the *DLP2010* digital micromirror device (DMD) was chosen as the spatial light modulator. This DMD offers an 854×480-pixel resolution within a 0.2" diagonal active region and with a small overall package. The issue design-wise in relation to the high level of integration and overall miniaturization is the bounding condition of dedicated digital light processing controllers (DLPCs) – in particular we chose DLPC3435 due to support of a 240 Hz frame rate. With a 240 Hz overall frame rate it is clear that the highest number of focal planes attainable is four, due to the requirement of at least a 60 Hz volumetric image refresh rate (which for most people should not result in noticeable achromatic flicker [9], [10]).

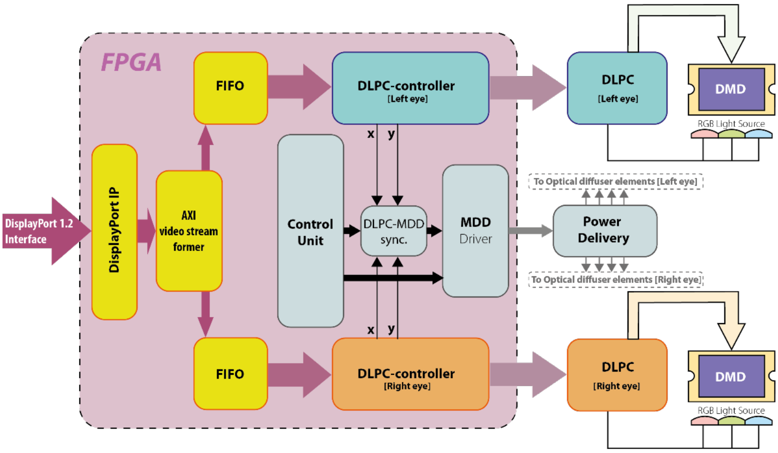

Fig. 1. Simplified block diagram of the integrated control module developed for an OST HMD produced at LightSpace Technologies.

The DLPC3435 is a proprietary DLP controller; thus, there is virtually no control options over internal processes or the way it interacts with the spatial light modulator (a digital micromirror device). The only freedom accessible by the designer is configuration of the frame rate, white balance adjustments and image orientation. Thus, it is of crucial importance, when tuning the multifocal prototype near-eye display device, to take into account specifics of the DLPC3435 operation and ensure the image output is well synchronized with the operation and switching of the optical diffuser elements.

The simplified block diagram of the integrated control module is depicted in Fig. 1. The data processing and main functionality are ensured by a *field-programmable gate array* (FPGA). The data host is a connected computer device, which interfaces through a USB-C and uses a DisplayPort 1.2 interface. The FPGA handles DisplayPort data stream decoding and formation of an *advanced extensible interface* (AXI) video stream. The DisplayPort data are split into two AXI video streams for each eye, which are buffered within a *First In-First Out* (FIFO) buffer of low capacity. Further the FIFO buffer is connected to a DLPC controller (symmetrical for both eyes). The DLPC controller reformats data to feed a steady video stream over digital video graphics array (VGA) to DLPC (more precisely the DLPC3435), which takes in a 240 Hz video feed. Furthermore, the DLPC controller incorporates a counter – to identify the image row and the pixel in each row transmitted. These X-Y coordinates are sent to DLPC-*multi diffuser driver* (MDD) synchronization module. The DLPC-MDD sync module calculates the order of diffuser elements to be activated from the received X-Y coordinates. The DLPC-MDD sync. module further is coupled to the MDD driver and sends the diffuser ID (to be activated) and enable pulse, whereas MDD driver then configures the diffuser driving circuitry to energize or discharge the given diffuser element. In parallel to switching of diffuser elements, a constant 240 Hz video feed is provided to corresponding DLPC modules, which by proprietary inner workings then output this information to DMD spatial light modulator as well as synchronously control the RGB light-source of the micro projection unit. The image output by DLPC-DMD obviously is carried out field-sequentially.

The DLPC controller was modelled to provide coordinates of the pixel row and number to enable synchronization between the DLPC driven projector images and switching of diffuser elements.

To know the synchronization constants, a test setup was assembled (Fig. 4). Two channels of a multi-channel oscilloscope were used to register output from the microprojector and optical switching of optical diffuser element. The switching of optical diffuser element was monitored by a photodetector, which captured light from a constant white LED emitter. In contrast, the second photodetector monitors projector output directly.

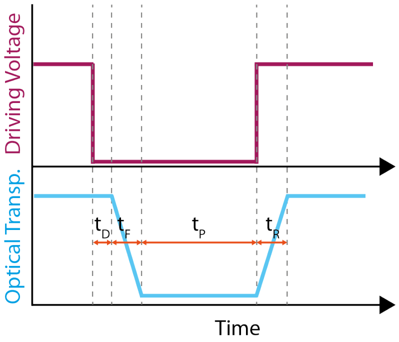

Fig. 2. Optical transparency of an optical diffuser element in response to an electric driving signal Transparency shown over visible spectrum (420 nm –700 nm). Distinct response times – t_D (delay time); t_F (fall time); t_P (projection time); t_R (rise time).

It must be noted that the switching cycle of an optical diffuser element has four distinct segments (Fig. 2). In the energized state, the diffuser element is transparent and does not interact with the incident light (Fig. 3a). Upon the removal of voltage, the first segment t_D is when the optical transparency remains unchanged. Typically, this period is in the range of 200–400 microseconds [11]. Then, the local field starts to collapse and the diffuser enters a transition from transparent to light-scattering state. This period is denoted by a fall time t_F, which is followed by the highly light-scattering state, in which the diffuser enters "screen-mode" – this is denoted by t_P and corresponds to a period, in which the projected image can be visualized (Fig. 3b). After the projection period t_p, an external electric field is applied again, the diffuser is energized and in response to the electric field undergoes transition from screen-mode to transparent mode – this is denoted as t_R or rise time.

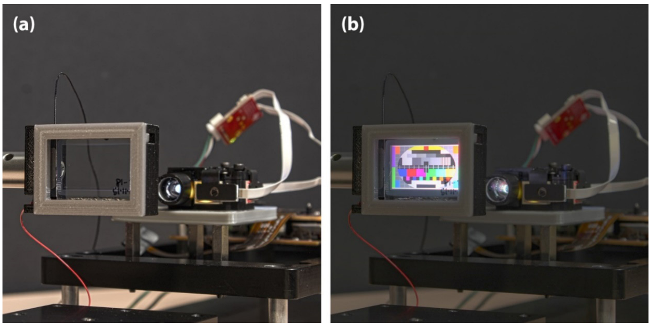

Fig. 3. Electrically driven optical diffuser element (acting as a switchable screen) in the transparent (a) and diffuse (b) state.

When considering image output, it is necessary to show the whole frame within the projection period of a diffuser element when it is in the highly light-scattering state. In case of utilised DLPC controller, it can be hard to achieve precise alignment of the projection and switching of diffuser element. Partly, this is also associated to the transitional periods – t_F and t_R, which are not instantaneous, and inability to explicitly control dead time of the projection unit, as this is predetermined.

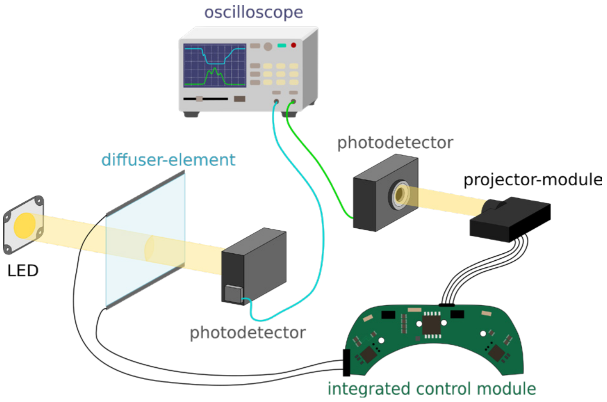

Fig. 4. Experimental setup for determining the frame output timeslot with respect to diffuser switching.

With the setup of Fig. 4, different colour frames were projected by the projector – white –, and primary-coloured frames (red, green, blue). Thus, it was established how the DLPC deals with image output. In the first part, we looked only at the output of the projector, which was receiving a feed of 240 Hz video stream, which contained a pattern of repeating white screen for a duration of one frame followed by three black-screen (blank) frames. Similar pattern was repeated using primary colours – red, green and blue.

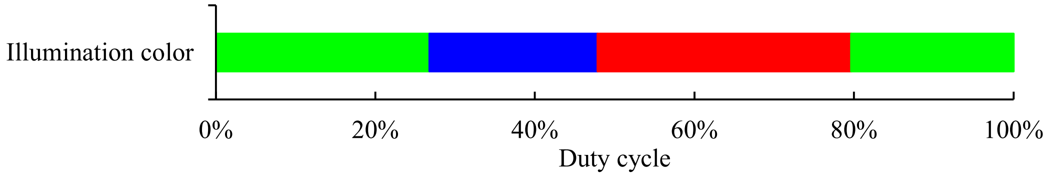

Fig. 5. DMD matrix illumination colour during one frame (dead time excluded) for a neutral white-point (zero offsets).

To reduce the appearance of colour artefacts, the DLPC3435 does not simply allocate one timeslot for displaying each colour. Even though the duty cycles are retained close to the nominal RGB 30,50,20 for a neutral white-point, the green LED imaging period is split into two sub-periods and displayed at the beginning and end of each frame (Fig. 5).

Typically, the different shades of a colour with a DMD are achieved by some combination of pulse width modulation (PWM) and light source intensity modulation (LSIM) [12]. This is due to the physical limitations of how fast a micromirror can switch from one state to another and be addressed again (usually about 20–30 μs [13]); thus, a true 8-bit colour depth at a 60 Hz volumetric refresh rate (corresponding to 240 Hz projector refresh rate) cannot be achieved by PWM alone, as this provides only about 4.1 ms for all three colours that each need to be further split into 255 shade gradations. However, the particular implementation of how shades are achieved is quite complex, as peculiarities of human visual system are often exploited to achieve a better perceived image, such as adjusting the colour output through colour dithering (this can be executed both spatially and temporally).

As previously mentioned, the dead time of an imaging period cannot be tuned directly; however, it could be expected that changing the green encoded bit value might provide an indirect approach – if the bitplanes on either end of the green imaging period can be identified and later removed by adjusting the input image, this might allow for longer dead time (however, at the cost of colour depth). With the increased dead time, the synchronization of diffuser elements to the imaging period can then be more easily adjusted by tuning the operation of the MDD.

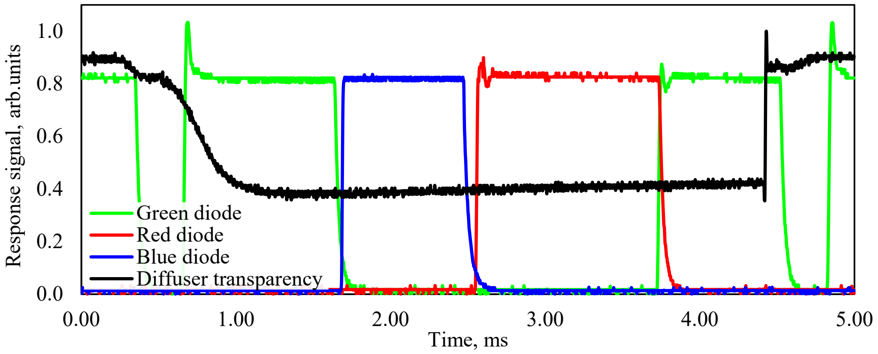

Fig. 6. Detector diode response to light reflected from the micromirror matrix, combined from primary colour (RGB) measurements, with diffuser element transparency as a reference.

In order to fine-tune the timings for switching the optical diffuser elements, a simple experimental setup was used to probe the operation of the DLPC3435 and DLP2010 combination.

First, it can be noted that the DLP2010 does not utilise LSIM – a purely white frame RGB(255;255;255) does not show any periods associated with lower light emitting diode intensity (Fig. 6). The required colour for low luminance shades that cannot be obtained through PWM alone is achieved through colour dithering.

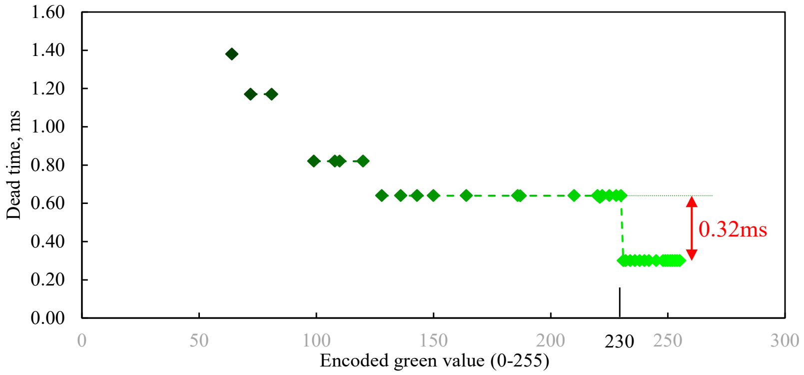

Fig. 7. Dependence of dead time on encoded green value passed to the DMD. A sharp step-wise decrease can be observed below encoded value of 230.

Next, as can be seen in Fig. 7, the total dead time increases in a step-wise fashion as the green encoded value is decreased to 230. Below this value the dead time plateaus – the illumination timeslots associated with these bits lay somewhere in the middle part of green illumination period (Fig. 8). Thus, the dead time remains unchanged until a significant decrease in green value is necessary and the illumination timeslots directly before or after the dead time are removed.

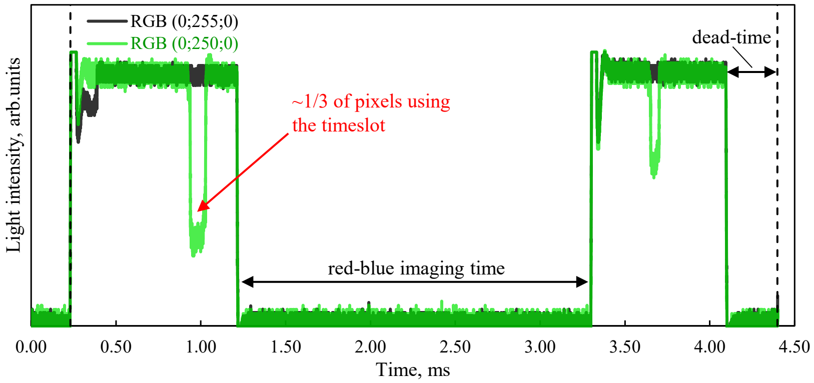

Fig. 8. Comparison of RGB(0;255;0) and RGB(0;250;0) encoded colour outputs from the DMD as detected by the setup in Fig. 4. Dashed lines indicate the beginning and end of one frame.

Notably, the illumination timeslots at the beginning and end of a frame imaging period are not used ever if the green value is below 230. This implies a non-straightforward bit mapping that is not a simple least-significant-bit placed at the beginning or end of an imaging period. What is more – often a given timeslot is used by some fraction of the pixels as can be seen by reduction in light intensity measured by the photodetector (Fig. 8); this, once again, hints that spatial colour dithering is applied to an image before it is displayed by the DMD.

The dead time required for feasibly switching the existing diffuser elements is about 0.6 ms (limited by the rise and fall times of a single diffuser element). As can be seen – by decreasing the encoded green value of each pixel below 230 on the software side, the obtained dead time is increased from 0.3 ms to about 0.64 ms, which is just enough to successfully project images without having to rework the available hardware.

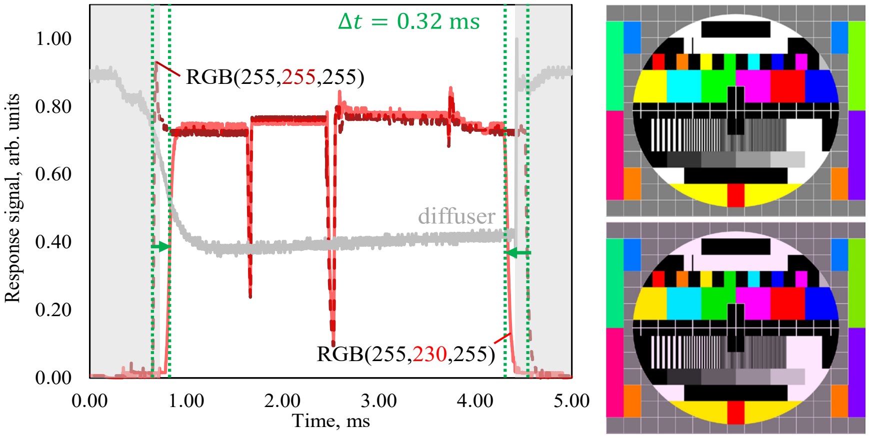

Fig. 9. Left: detector diode response to light reflected from the micromirror matrix, comparison of different green components. Diffuser transparency as a timing reference. An increase in dead time can be observed, achieved through removing green illumination timeslots at both the beginning and the end of a frame. Right: two colour calibration test patterns with full green component (top) and adjusted green component (bottom). A characteristic red tint can be seen.

Whilst the image output on a single diffuser element is well-behaved and reduction of encoded green value allows for the removal of colour bleeding between different image depth planes through increased dead time, the addition of multiple focal planes produces a visual artefact similar to laser speckling. We speculate that this unwanted visual effect, which becomes evident in the case of a multifocal display architecture, is associated with temporal dithering produced internally by the DLPC chipset.

4. CONCLUSIONS

In the paper, we have demonstrated the possible application of DLP technology in creating a multifocal OST HMD. The limited tunability of off-the-shelf DLPCs can be overcome by adjusting the input parameters of an image (namely, the encoded bit value for the green colour channel); however, this comes at a cost of reduced colour depth. One of the major advantages of DMD-based projection systems is the elimination of colour switching artefacts. However, colour dithering for accurate colour perception becomes a challenge. When the images are output time-sequentially on different image depth planes at a lower frame rate, the image quality suffers due to visual artefacts similar to speckling.

ACKNOWLEDGEMENTS

The research has been supported by the European Regional Development Fund project No. 1.2.1.1/18/A/006 study No. 1.2 "Development of Electronics for Multifocal Augmented and Virtual Reality Displays".

REFERENCES

1. Cearley, D. W. (2020). *Top 10 Strategic Technology Trends for 2020*. Available at https://emtemp.gcom.cloud/ngw/globalassets/en/publications/documents/top-tech-trends-2020-ebook.pdf
2. Rauschnabel, P. A., & Ro, Y. K. (2016). Augmented Reality Smart Glasses: An Investigation of Technology Acceptance Drivers. *International Journal of Technology Marketing*, *11* (2), 123. https://doi.org/10.1504/IJTMKT.2016.075690.
3. Vishton, P. M., & Cutting, J. E. (1995). Perceiving Layout and Knowing Distances: The Integration, Relative Potency, and Contextual Use of Different Information about Depth. *Perception of Space and Motion*, 5, 69–117. San Diego, CA: Academic Press.
4. Hoffman, D. M., Girshick, A. R., Akeley, K., & Banks, M. S. (2008). Vergence-Accommodation Conflicts Hinder Visual Performance and Cause Visual Fatigue. *Journal of Vision*, *8* (3), 1–30. https://doi.org/10.1167/8.3.33.
5. Shibata, T., Kim, J., Hoffman, D. M., & Banks, M. S. (2011). Visual discomfort with stereo displays: Effects of viewing distance and direction of vergence-accommodation conflict. In A. J. Woods, N. S. Holliman, & N. A. Dodgson (Eds.), *Stereoscopic Displays and Applications XXII* (vol. 7863, p. 78630P). https://doi.org/10.1117/12.872347.

6. Zabels, R., Osmanis, K., Narels, M., Gertners, U., Ozols, A., Rutenbergs, K., & Osmanis, I. (2019). AR Displays: Next-Generation Technologies to Solve the Vergence-Accommodation Conflict. *Applied Sciences (Switzerland)*, *9* (15). https://doi.org/10.3390/app9153147.
7. Ozols, A., Zutis, E., Zabels, R., Linina, E., Osmanis, K., & Osmanis, I. (2021). Fast-switching liquid crystal diffusers: Outlook on optical properties and applicability in volumetric display architecture. In: C. Peroz & B. C. Kress (Eds.), *Digital Optical Technologies 2021* (p. 26). SPIE. https://doi.org/10.1117/12.2594147.
8. Osmanis, K., Valters, G., Zabels, R., Gertners, U., Osmanis, I., Kalnins, L., … & Ozols, A. (2018). Advanced multiplanar volumetric 3D display. In: I. Muševič, L.-C. Chien, D. J. Broer, & V. G. Chigrinov (Eds.), *Emerging Liquid Crystal Technologies XIII* (vol. 1055510, p. 36). SPIE. https://doi.org/10.1117/12.2297629.
9. de Lange Dzn, H. (1954). Relationship between Critical Flicker-Frequency and a Set of Low-Frequency Characteristics of the Eye. *Journal of the Optical Society of America*, *44* (5), 380. https://doi.org/10.1364/JOSA.44.000380.
10. Brown, A., Corner, M., Crewther, D. P., & Crewther, S. G. (2018). Human Flicker Fusion Correlates with Physiological Measures of Magnocellular Neural Efficiency. *Frontiers in Human Neuroscience*, *12*, 1–7. https://doi.org/10.3389/fnhum.2018.00176.
11. Zabels, R., Osmanis, K., Narels, M., Smukulis, R., & Osmanis, I. (2019). Integrated Head-Mounted Display System Based on a Multi-Planar Architecture. *Advances in Display Technologies IX*, 1094208. https://doi.org/10.1117/12.2509954.
12. Anderson, C. H. (2000). *DMD Modulated Continuous Wave Light Source for Imaging Systems.* United States Patent.
13. Texas Instruments. (2020). *DLPC3430 and DLPC3435 Display Controller Datasheet*. Available at https://www.ti.com/lit/ds/symlink/dlpc3430.pdf

LATVIAN JOURNAL OF PHYSICS
AND TECHNICAL SCIENCES
2022, N 3

DOI: 10.2478/lpts-2022-0014

SCENARIO-BASED MODELLING OF RESIDENTIAL SECTOR CONSUMPTION: A CASE STUDY IN LATVIA

E. Kairisa[1*], A. Mutule[1], I. Drovtar[1], T. Korotko[1], O. Borscevskis[2],
H. Wilkening[3], Ch. Troyer[3]

[1]Institute of Physical Energetics, Smart Grid Research Centre
14 Dzerbenes Str., Riga, LV-1006, LATVIA
[2]Sadales tīkls JSC, 1 Smerla Str., Riga, LV-1160, LATVIA
[3]European Commission, DG JRC Joint Research Centre, Dir C Energy, Transport and Climate, C03 Energy Security, Distribution and Markets Unit
P.O. Box: 2, NL-1755 ZG Petten, The NETHERLANDS
*e-mail: evita.kairisa@edi.lv

Promoting the development of energy communities is one of the planned development areas mentioned in the Latvian National Energy and Climate Plan (NECP). Even though energy communities do not yet exist in Latvia, they could improve the quality of the environment and stimulate the local economy. In any case, it is expected that the structure of household energy consumption in Latvia will change as households start to adopt new technologies such as electric cars and heat pumps, as well as participate in energy production and demand response.

Often the starting point for the development of an energy community is the geographic location of consumers. Therefore, for this study, a microdistrict was chosen in one of the most developed suburbs of Riga in Latvia, in which 76 households are located. The study identified five milestones on the path from mere neighborhood to the energy community. The resLoadSIM Residential Load Simulation tool was chosen to simulate realistic energy consumption with a 1-minute time resolution, as well as to model the future solar energy consumption and generation in the community on its way to becoming an energy community and meeting these goals. The network constraints associated with the transformer and lines are taken into account and it is assumed that the district will not invest in the development and expansion of the network.

Based on the results of the modelling, an analysis was made of the impact of the development of the energy community in Latvia and how each stage of development will affect energy consumption, the amount of renewable energy, the energy sent to the grid, the power consumed directly, and the share of solar energy in energy consumption.

Keywords: *Energy community development, scenario-based modelling, resLoadSIM, RES.*

1. INTRODUCTION

To address household contribution to climate change and to reduce greenhouse gas emissions, the introduction of local generation and expansion of new demand types (such as electric vehicles (EV) and heat pumps (HP)) are inevitable. The EU Roadmap for Moving to a Competitive Low Carbon Economy in 2050 establishes a long-term vision to cut domestic greenhouse gas emissions by at least 80 % by 2050 compared to 1990. The Winter Package "Clean energy for all Europeans" aims at transition to a more sustainable energy system by placing citizens at the centre of energy policies. According to the Winter Package, the expansion of renewables has a key role in meeting GHG reduction targets.

To achieve the above-mentioned sustainability goals, citizens are creating and joining energy communities that give them the power to engage in clean energy transition. It is a form of social movement in which citizens voluntarily participate in renewable energy projects allowing for more inclusive and democratic processes. Energy communities often start their activities by only producing energy, as it brings many positive benefits to residents. An increasing number of energy communities provide additional services, such as electro-mobility, energy efficiency initiatives (i.e., building renewal, energy audits, consumption monitoring, etc.), the flexibility of uses, energy storage and smart grid integration, energy monitoring and grid management, as well as financial services and consultation services to develop community initiatives [1]. For example, energy efficiency initiatives are a great way to gain expertise and trust in the community, especially in the beginning, whereas an electric car-sharing scheme is a great activity for existing community energy projects [2], [3]. The report [4] focused on an analysis of 24 energy communities and found that, although some communities performed only generation activities, 10 of them participated in energy efficiency activities (such as the renovation of buildings and replacement of inefficient households appliances), and 8 of them offered electro-mobility services.

The residential sector in Latvia shares a significant portion (28.4 % in 2019) of total energy consumption [5]. According to Latvia's NECP, Latvia is planning to increase the share of renewable energy sources (RES) in the production of electricity by significantly increasing the installed capacity of wind and solar energy. The electricity produced by photovoltaic (PV) systems in Latvia is showing an upward trend. In 2019, solar power plants produced 3 GWh of electricity – three times more than in 2018. PV installation to the residential sector is offered by electricity traders, on average installing 5–6 kW systems, which turns residential consumers into prosumers. [6], [7]. The current policy is based on the use of the net settlement system. When energy is transferred from a household to the power grid, this amount is deducted by the household invoice for the next billable month. To support the improvement of energy efficiency in private homes, the Ministry of Economics has approved a programme that supports the installation of solar panels and small wind generators. It must be ensured that the reduction in primary energy is at least 20 %, and produced energy is used for self-consumption [8]. The Ministry of Environmental Protection and Regional Development has developed a support programme for the use of renewable energy resources in households. One of the supported activities is the purchase of new renewable energy equipment for electricity production [9].

Although the number of EVs is not large in Latvia, it is expected to reach significant levels in the future. In total, at the beginning of 2022, almost 2200 EVs were registered in Latvia (only 0.3 % of the total passenger vehicle fleet). In 2020, the number of EVs in Latvia increased by 85 % [10]. One of the reasons why people in Latvia still prefer internal combustion engines is the unavailability of charging stations. By September 2020, 316 public charging points have been built, but the ratio to land area is still low [11]. Even though some measures have been introduced to promote the use of EVs (free parking, the possibility of using public transport lanes, etc.), the EV infrastructure is developing slowly and is not always accessible to residential users. Since 2022, grants for the purchase of EVs have been available in Latvia. The amount of support is 4500 EUR for a new EV and 2250 EUR for a used car. Given the amount of funding available, it was forecast that the total number of electric vehicles and externally chargeable hybrids purchased could reach 3800 [12].

Potential method that can mitigate unfavourable side effects of intermittent generation is demand response (DR). In the context of this paper, DR is intended to efficiently use the energy surplus produced by the PV panels for self-consumption by shifting high consumption appliances to off-peak hours. By reducing the amount of solar electricity injected into the grid, self-consumption provides benefits on the grid side. Energy communities also have a social objective, so avoiding grid failure, increasing the stability of the electricity system, reducing energy losses in grids and transformers, improving the quality of voltage, and postponing upgrading work, undoubtedly have a positive impact on the whole community [13]. DR is still at the early stage in Latvia and has not been widely researched. However, the Electricity Market Law and the Law on Regulators of Public Utilities, which are in force in Latvia, allow for the use of DR.

The motivation for this paper is to study the realistic development of the energy community in Latvia, considering that Latvia has significant room to expand new social movements and novel technology adoption and would benefit from a planning framework and research findings. The research has been conducted by scenario-based modelling to identify five checkpoints on the path from a simple neighbourhood to an energy community, assuming that the community will increase its generation capacity gradually while increasing the number of collective energy initiatives.

2. RATIONALE FOR SCENARIO DEVELOPMENT

Good quality electrical load modelling tools allow for more accurate prediction of future scenarios. In particular, statistical models can be beneficial to predict building occupancy and thence consumption patterns [14]. Consumption of each appliance is constructed by investigating their frequency of use, turn-on time, operating time, etc. The total load profile is composed of summing up the load of each appliance. The statistical modelling results indicate what is likely to happen rather than revealing an optimal course of action. In this paper, five scenarios are simulated, with the resLoadSIM modelling tool, which simulates the load profiles of individual households by predicting the switching on/off of each appliance using a probabilistic approach. Each scenario corresponds to a different energy community development step, starting from a simple neighbourhood, and ending with an energy-efficient energy community that offers its residents electro-mobility services.

In this paper, three assumptions are made about the goals of the energy community. Firstly, the community chooses solar energy as a source of their energy production. The paper [15] states that solar PV power should be 25 % of the total generation mix to achieve Paris Climate targets. Also, it is expected that almost half of EU households will produce renewable energy in 2050 [16]. It is assumed that the community aims to reach those two targets.

Secondly, the community chooses to join in EV car-sharing activities and improve energy efficiency while still considering grid restrictions. Energy communities have the potential to provide direct benefits to citizens by advancing energy efficiency and lowering their electricity bills. Likewise, electric mobility services can be used to improve efficiency and sustainability in energy communities. Integration of renewable power generation with electric mobility infrastructures is a way to alleviate the massive connection of numerous fleets of EVs to power grids. The possible advantages are reduction of electricity generation and charging costs, energy efficiency increase (in terms of reduction of renewable energy curtailment), and environmental benefits (increased renewable share in power systems) [17]. However, it is necessary to consider the grid restrictions when planning new energy activities in the community. For instance, the replacement of inefficient household appliances can lead to decreased consumption, which results in increased energy delivered through the grid. An increase in load during peak hours can cause lines to exceed their capacity limits, resulting in increased thermal loads and potential damage. Also, increased share intermittent generation and additional EV charging stations might lead to voltage problems in the existing grid, which require additional investments for solving [18].

The rationale for the first and second assumptions is the new state support mechanisms that support the installation of PV panels and the purchase of EVs by Latvian households. Energy efficiency activities have been selected because one of the targets of Latvia’s NECP for 2030 is that society has become more aware of energy efficiency issues and there has been an increase in involvement and the desire to ensure energy efficiency in daily life of the community.

Thirdly, we assume that the energy community will not invest in grid development and expansion but will only take into account the restrictions of the grid. Very high penetration of solar PV can lead to operational and reliability challenges (voltage variations and congestions in the electrical network) and reduction in environmental benefits [19], [20]. In [21], a real distribution feeder is analysed, utilising a residential load profile, against various PV penetration levels. Results show that an increase in PV penetration reduces the instances of under-voltage, yet the occasions of overvoltage increase substantially. Further, DR smooths daily load variations by moving a fraction of consumption from peak to off-peak period and reduces the effects of load fluctuations caused by the increased amount of intermittent energy injected into the grid.

3. METHODOLOGY

This section introduces the method for predicting the future development of energy communities in realistic Latvian conditions. Firstly, load identification was performed to find a suitable location for the development of the energy community in Latvian conditions. Secondly, the load profile was generated for the selected location to obtain electricity consumption in high time resolution for a full year. Thirdly, a scenario-based simulation was performed to describe five scenarios that identify a path from a simple neighbourhood to an energy community.

Load identification was performed to select a location in Latvia where the development of energy communities could be most suitable. As a result, a neighbourhood in a suburban area with 76 households was selected and modelled. The main objectives for the selected location are that residents live there permanently with constant electricity consumption (in contrast to summer houses, where consumption is seasonal) and the electricity network is relatively new and would not require investments in the near future.

The load profile generation process for a selected location consisted of collecting site-specific information (data about annual energy consumption, daily load curves and solar irradiation values) and statistical data on the use of household appliances in Latvian households. Statistical and site-specific data were used with the resLoadSIM tool [22], developed by EC JRC to simulate the base-case that represented the selected location. Later, modelling parameters were adjusted to represent the selected location as accurately as possible. ResLoadSIM is a stochastic bottom-up simulation tool that predicts electric residential load profiles of households with a high time resolution. The resLoadSIM modelling tool was used because it allowed obtaining realistic load profiles by adjusting a wide variety of parameters so that the resulting load profiles were as close as possible to the real ones. Some benefits of this tool are that it is very flexible and allows for the evaluation of the potential of certain energy community development steps.

For the purpose of this paper, five different scenarios were described that combined different deployment levels of solar PV, EVs and energy efficiency initiatives. The scenarios were made by adding new energy technologies to the modelling tool, changing household energy control strategies, and changing parameters and usage patterns of household appliances. All developed scenarios were simulated using resLoadSIM and compared to the base-case simulation. The results were analysed to identify what energy communities would look like in Latvia.

4. CASE STUDY AND DATA COLLECTION

In this study, a residential district located in Latvia was chosen as a testbed. The selected area is suburban and consists of 76 clients, with more than 450 thousand kWh annual consumption. From this area, hourly load curve, number of clients and annual electricity consumption are known. In Fig. 1, the service area of the selected location is shown.

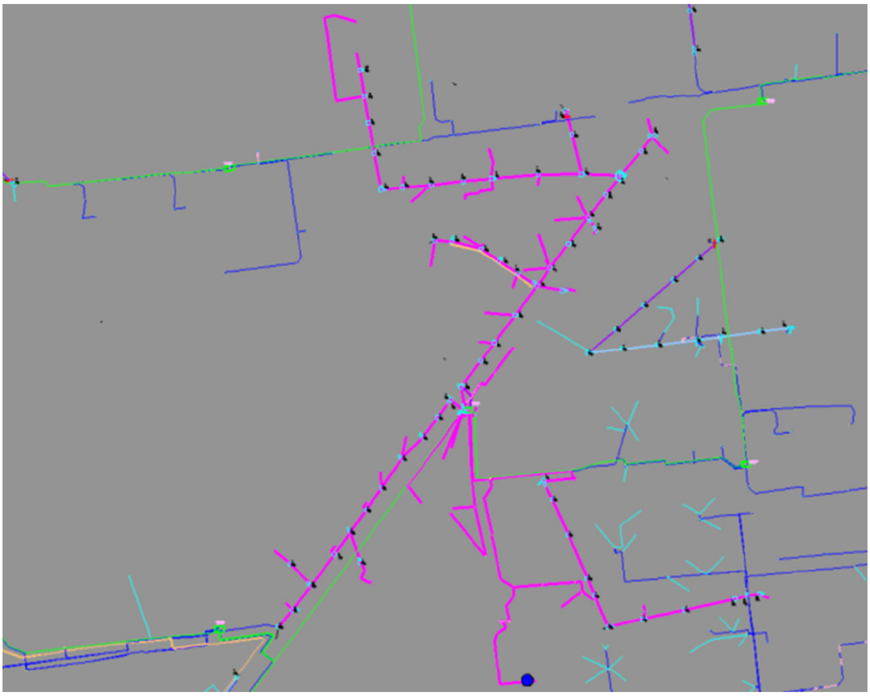

Fig. 1. The service area of existing 20/0.4kV transformer substation.

Full time series of hourly values of temperature and solar irradiation at a given location and year are obtained from the PVGIS [23] database. At first, resident characteristics and appliance usage patterns are selected, based on statistical data from Latvia. Later, they are adjusted to match consumption in a chosen residential location.

5. MODELLING PARAMETERS AND CONSTRAINTS

To model electrical consumption with resLoadSIM, household characteristics (household size, number of residents, etc.) and electrical appliance usage patterns (percentage of houses using each appliance, energy class, etc.) are needed. Before performing scenario-based modelling, it is also necessary to determine parameters for a PV system and EV systems, and rules for DR. Between sunrise and sunset, the power output of a PV system is determined using its nominal power and solar irradiation values, which are obtained from the PVGIS database. To perform PV system modelling, additional information about PV system is needed – information about the estimated system losses of a PV installation, the minimum and maximum size of a solar module per household resident, minimum and maximum efficiency of a solar module.

For EV modelling, the type of location (urban or rural) is required, as well as the energy consumption of the car, the battery capacity, and self-charging rate. ResLoadSIM provides an opportunity to include smart e-vehicles that try to charge their batteries when there is a solar energy surplus. Lastly, to model peak shaving, the peak shaving threshold needs to be specified. This threshold refers to the maximum peak value, which has been calculated during the first day of the simulation.

6. SCENARIOS

In this paper, the following scenarios have been created. It should be emphasised that the end goal of the selected community is to increase its renewable energy share to 25 % of annual energy consumption and increase its energy efficiency while considering existing grid restrictions.

(S1) The first scenario simulates the real neighbourhood of 76 households. The daily load curve and annual energy consumption are known beforehand. The annual energy consumption of all households is approximately 453 thousand kWh. The residents use household appliances with a large variety of energy classes, drive with vehicles that run on traditional petroleum fuels, and heat their houses from district heating. In the resLoadSIM modelling tool, parameters are adjusted to represent the selected location as accurately as possible. The grid restrictions associated with the transformer and lines are taken into account, and an assumption is made that the neighbourhood will not make investments in grid development and expansion. Based on these restrictions, the maximum amount of energy sent to the grid is 128 kW.

(S2) In the second scenario, the abovementioned neighbourhood starts to form an energy community. The energy communities often start with energy production, for example, by installing PV panels. The not-for-profit nature of energy communities suggests that the profit from energy production is returned to the community, for example, by increasing the number of PV panels. In this scenario, we are looking at the point in community development where approximately a half of the grid restrictions is met. More specifically, the maximum power sent to the grid is 61 kW. On this occasion, 18 households have installed PV panels on their rooftops. On average, 59 % of solar energy is used immediately, and the rest is sent to the grid. Annual solar generation is 17 % of total annual energy consumption. The community aims at increasing the share of solar energy production to 25 % of annual energy consumption, as well as engaging in various energy activities, such as collective self-consumption and electro-mobility, in a way that does not violate grid restrictions.

(S3) In the third scenario, the community begins to implement a peak-shaving control strategy while continually adding new PV panels on their territories. The appliances are not changed in this step, and load shifting is based on the wiring of these appliances. In this step, 26 households have installed PV panels. Due to peak shaving, average energy consumption has decreased a little. 56 % of solar energy is used immediately, and solar production accounts for 23 % of annual energy consumption.

(S4) In the fourth scenario, the community is launching an EV car-sharing initiative, as well as continuing to increase their PV assets. The number of households with PV panels has increased to 38 households and 50 % of households are using EV car-sharing possibility. In this step, the maximum power sent to the grid is 97 kW.

61% of solar energy is used immediately and solar production accounts for 22% of annual energy consumption.

(S5) In the fifth scenario, appliances with low energy class are replaced, and the number of PV panels is increased to a maximum based on grid restrictions. We assume that all appliances below the efficiency class D are changed to class A. The rest of the appliances are used as previously. As a result, 39 households have installed PV and the maximum power sent to the grid is 124 kW. 53 % of solar energy is used immediately and solar production is 31 % of annual energy consumption.

Table 1. Summary of Scenarios.

Scenario	Households with PV	EV car-sharing	Energy efficiency initiatives	Share of PV power	% of solar used immediately	Max power sent to grid
S1	-	-	None	-	-	-
S2	18	-	None	17 %	59 %	61 kW
S3	26	-	Peak shaving	23 %	56 %	80 kW
S4	38	50 %	Peak shaving	22 %	61 %	97 kW
S5	39	50 %	Peak shaving + New appliances	31 %	53 %	124 kW

From Table 1 it can be seen that the community was able to meet its goals. In each step, the community increased its production of solar energy. When new energy efficiency initiatives were introduced, the percentage of immediately used solar energy decreased. The introduction of EV sharing increased the percentage of immediately used energy but decreased the share of PV power as a result of increased energy consumption. In the last step, the share of solar energy was 31%, and more than half of households had PV on their rooftops. The goals were achieved without exceeding grid restrictions.

7. MODELLING RESULTS

This section provides a more detailed analysis of each scenario. In Fig. 2, a load curve of typical daily electricity consumption is presented. The shape of the consumption curve is similar in all five scenarios. However, it can be seen that changes associated with different scenarios affect the evening peak much more than the morning peak. It is evident that EV charging in S4 has a powerful effect on electricity consumption. Moreover, the replacement of low-efficiency household appliances in S5 decreased this consumption.

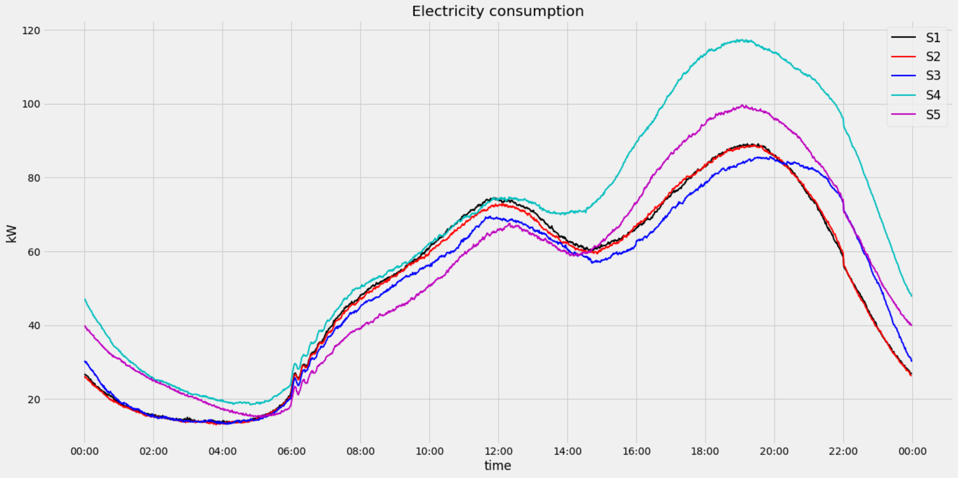

Fig. 2. Electricity consumption for all scenarios.

In Fig. 3 it can be seen that the highest amount of energy used immediately is in the middle of the day and does not change much between 8 am and 2 pm. It is noticeable that S2, S3, and S4 scenarios are quite similar, and only S5 differs the most from the others as the line is much lower.

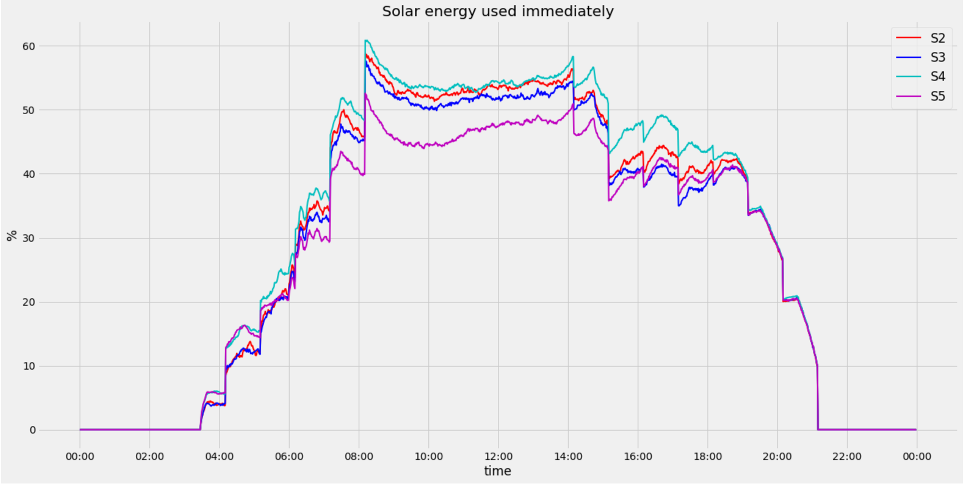

Fig. 3. The amount of solar energy used immediately for S2–S5 scenarios.

Figure 4 shows one week in July for all scenarios with PV generation. It can be seen that S3 produces more solar energy than S2 and uses a load shaving strategy. S4 increased consumption and solar generation compared to S2 and S3 due to an increase in the number of PV installed and the ongoing EV car-sharing initiative, while S5 reduced consumption compared to S4 because of the replacement of low-efficiency appliances.

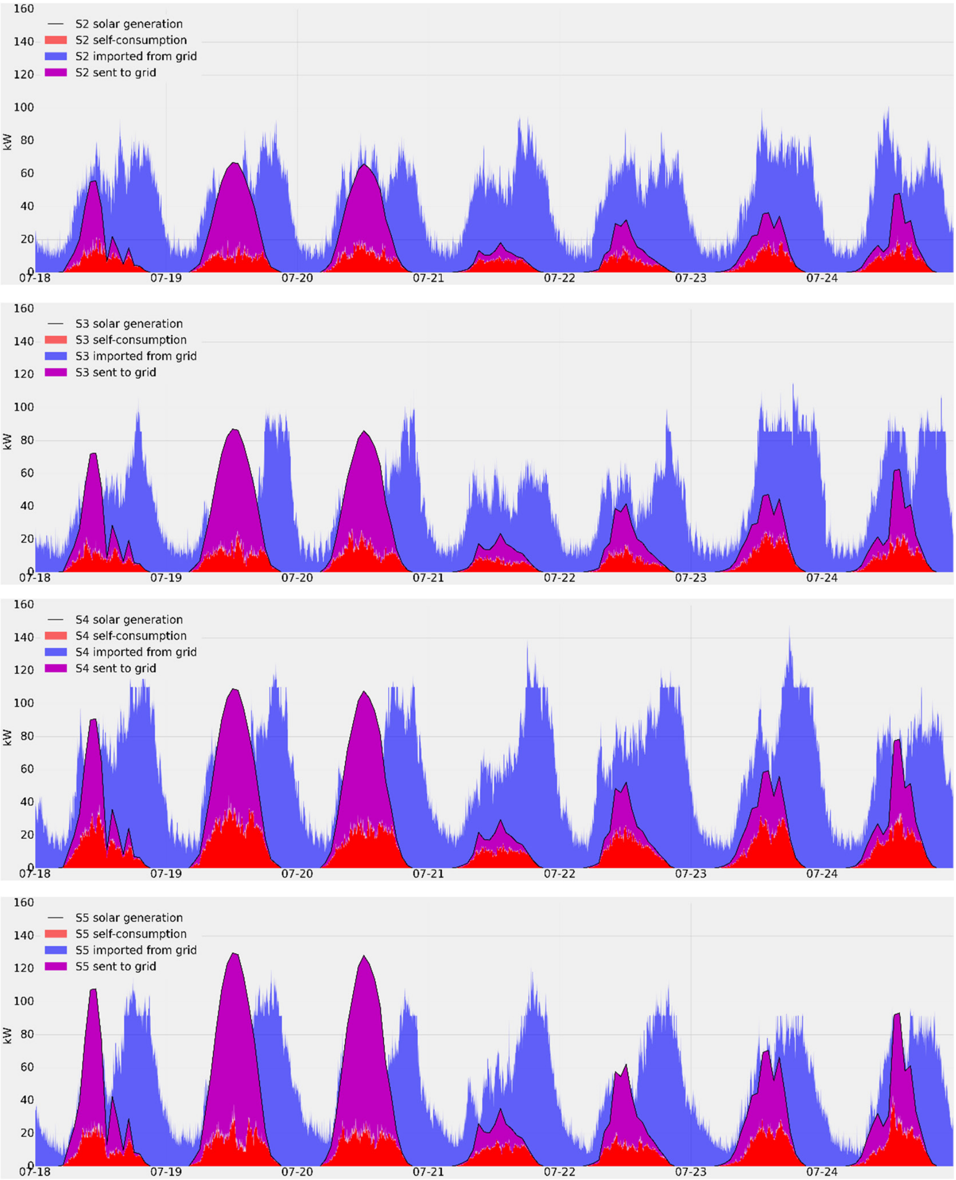

Fig. 4. Energy consumption and solar generation over one week for S2–S5 scenarios.

8. CONCLUSIONS

Energy communities can help achieve various sustainability goals and enable citizens to engage in the clean energy transition. It is a form of social movement, which does not exist yet in Latvia, but could be relevant in the future. This paper has studied what the realistic development of the energy community could look like in Latvia since there is significant room to expand new technology adoption, and research findings can be beneficial. Energy communities provide a wide variety of services; for the purpose of this paper, we have considered only energy efficiency and electro-mobility services. Additionally, new state support instruments have recently been introduced in Latvia to promote renewable energy and the purchase of EVs.

We consider that the energy community uses solar energy as their renewable energy source. Generation capacity is increasing gradually as the not-for-profit nature of local energy communities suggests that the profit from energy production is returned to the community by increasing the number of PV panels. In the selected location, half of the households can install PV panels, before grid constraints no longer allow for the expansion of the community. The share of solar energy in energy consumption is 31 %, which is higher than initially planned.

Modelling results clearly show the effect of electro-mobility and energy efficiency services on the consumption of the energy community and how it affects the use of solar energy. The next practical steps for the energy community could be investment in the expansion of the internal electricity grid, which will allow the community to increase production capacity, as well as the implementation of energy storage technology and heat pumps.

ACKNOWLEDGEMENTS

The paper emanates from the research supported by the ERA-NET co-fund grant under the CHIST-ERA IV Joint Call on Novel Computational Approaches for Environmental Sustainability (CES), project "Supporting Energy Communities – Operational Research and Energy Analytics" (SEC-OREA).

REFERENCES

1. De Lotto, R., Micciché, C., Venco, E.M., Bonaiti, A., & De Napoli, R. (2022). Energy Communities: Technical, Legislative, Organizational, and Planning Features. *Energies 2022, 15* (5), 1731. doi: 10.3390/en15051731.
2. Walsh, M., Castanie, M., & Giovannini, S. (2020). *Community Energy: A Practical Guide to Reclaiming Power*. Available at https://www.rescoop.eu/toolbox/community-energy-a-practical-guide-to-reclaiming-power
3. Ahmadiahangar, R., Baharvandi, A., Rosin, A., Haring, T., Azizi, E., Korotko, T., & Shabbir, N. (2020). Energy storage expansion planning in microgrid. In: *2020 IEEE 14th Int. Conf. Compat. Power Electron. Power Eng. CPE-POWERENG 2020*, (pp. 433–437), 8–10 July 2020, Setubal, Portugal. doi: 10.1109/CPE-POWERENG48600.2020.9161502.
4. Caramizaru, A., & Uihlein, A. (2020). *Energy Communities: An Overview of Energy and Social Innovation*. Luxembourg: Publications Office of the European Union.
5. Official Statistics Portal. (2020). *Significant Increase in Electricity Consumption in Transport Sector*. Available at https://stat.gov.lv/en/statistics-themes/business-sectors/energy/press-releases/2176-energy-consumption-2019
6. Lebedeva, K., Krumins, A., Tamane, A., & Dzelzitis, E. (2021). Clean Technologies Analysis of Latvian Households' Potential Participation in the Energy Market as Prosumers. *Clean Technol. 2021, 3* (2), 437–449. doi: 10.3390/cleantechnol3020025.
7. Korotko, T., Rosin, A., & Ahmadiahangar, R. (2019). Development of prosumer logical structure and object modeling. In: *2019 IEEE*

13th Int. Conf. Compat. Power Electron. Power Eng. CPE-POWERENG 2019, (no. 19047010), 23–25 April 2019, Sonderborg, Denmark. doi: 10.1109/CPE.2019.8862390.

8. Ministry of Economics. (2022). *Apstiprināta atbalsta programma privātmāju energoefektivitātes paaugstināšanai un saules paneļu uzstādīšanai*. Available at https://www.em.gov.lv/lv/jaunums/apstiprinata-atbalsta-programma-privatmaju-energoefektivitates-paaugstinasanai-un-saules-panelu-uzstadisanai
9. Ministry of Environmental Protection and Regional Development (2022). *Atbalsta programma atjaunojamo energoresursu izmantošanai mājsaimniecībās*. Available at https://www.varam.gov.lv/lv/atbalsta-programma-atjaunojamo-energoresursu-izmantosanai-majsaimniecibas?utm_source=https%3A%2F%2Fwww.google.com%2F
10. CSDD. (2022). *Par 2021. gada 4. ceturksnī reģistrētajiem elektrotransportlīdzekļiem*. Available at http://www.e-transports.org/index.php/statistika/33-elektro-transportlidzekli
11. European Court of Auditors. (2021). *Special Report 05/2021: Infrastructure for Charging Electric Vehicles: More Charging Stations but Uneven Deployment Makes Travel across the EU Complicated*. Available at https://www.eca.europa.eu/Lists/ECADocuments/SR21_05/SR_Electrical_charging_infrastructure_EN.pdf
12. lsm.lv (2021). *State to Issue Grants for Purchase of Electric Vehicles*. Available at https://eng.lsm.lv/article/economy/transport/latvian-state-to-issue-grants-for-purchase-of-electric-vehicles.a435503/
13. Di Silvestre, M.L., Ippolito, M.G., Sanseverino, E.R., Sciumè, G., & Vasile, A. (2021). Energy Self-Consumers and Renewable Energy Communities in Italy: New Actors of the Electric Power Systems. *Renew. Sustain. Energy Rev.*, *151*, 111565. doi: 10.1016/J.RSER.2021.111565.
14. Rae, C., Kerr, S., & Maroto-Valer, M.M. (2020). Upscaling Smart Local Energy Systems: A Review of Technical Barriers. *Renew. Sustain. Energy Rev.*, 131, 110020, doi: 10.1016/J.RSER.2020.110020.
15. International Renewable Energy Agency. (2019). *Future Of Solar Photovoltaic Deployment, Investment, Technology, Grid Integration and Socio-Economic Aspects*. Available at www.irena.org/publications
16. Kampman, B., Blommerde, J., & Afman, M. (2016). *The Potential of Energy Citizens in the European Union*. Available at www.cedelft.eu
17. Piazza, G., Bracco, S., Delfino, F., & Siri, S. (2021). Optimal Design of Electric Mobility Services for a Local Energy Community. *Sustain. Energy, Grids Networks*, *26*, 100440. doi: 10.1016/J.SEGAN.2021.100440.
18. Rosin, A., Drovtar, I., Molder, H., Haabel, K., Astapov, V., Vinnal, T., Korotko, T. (2022). Analysis of Traditional and Alternative Methods for Solving Voltage Problems in Low Voltage Grids: An Estonian Case Study. *Energies 2022, 15* (3). doi: 10.3390/EN15031104.
19. Cerna, F.V. (2022). A Hybrid PV Scheme as Support to Relieve Congestion in the Domestic Supply Network. *Int. J. Electr. Power Energy Syst.*, *134*, 107413. doi: 10.1016/J.IJEPES.2021.107413.
20. Padhee, M., & Pal, A. (2018). Effect of solar PV penetration on residential energy consumption pattern. In: *IEEE North American Power Symposium (NAPS)*, (pp. 1–6), 9–11 September 2018, Fargo, ND.
21. Sharma, V., Aziz, S.M., Haque, M.H., & Kauschke, T. (2020). Effects of High Solar Photovoltaic Penetration on Distribution Feeders and the Economic Impact. *Renew. Sustain. Energy Rev.*, *131*. doi: 10.1016/J.RSER.2020.110021.
22. Joint Research Centre. (2022). *Our Models Portfolio. JRC Smart Electricity Systems and Interoperability*. Available at https://ses.jrc.ec.europa.eu/power-system-modelling
23. European Commission. (2019). *JRC Photovoltaic Geographical Information System (PVGIS)*. Available at https://re.jrc.ec.europa.eu/pvg_tools/en/tools.html#PVP

LATVIAN JOURNAL OF PHYSICS
AND TECHNICAL SCIENCES
2022, N 3

DOI: 10.2478/lpts-2022-0015

DEVELOPMENT OF THE DISTRICT HEATING SYSTEM ON THE LEFT BANK OF THE DAUGAVA RIVER IN RIGA

E. Dzelzitis, N. Talcis, I. Pilmanis, I. Bode, L. Jansons, L. Zemite*

Riga Technical University,
Faculty of Civil Engineering, Institute of Heat, Gas and Water Technology,
6B/6A Kipsalas Str., Riga, LV-1048, LATVIA
*e-mail: laila.zemite@rtu.lv

In Latvia, heat supply is provided in three different ways: using district heating (*hereinafter* – DH), local heating and individual heating systems. Heat energy consumption consists of heat energy consumption for heating, hot water and heat energy technological processes. The structure of DH consumers has not changed in recent years and the largest consumers of heat are households – 70 % of the total energy consumption. The district heating system accounts for approximately 29 % of the total consumption. There is also the so-called tertiary sector, which is made of municipal and state buildings with a minor total heat consumption of about 1 %.

It should be noted that 65–70 % of energy is used for heating needs, and 30–35% for hot water preparation. In Latvia, heat of DH consumers is produced both in boiler houses (*hereinafter* – BHs) and cogeneration plants (*hereinafter* – CHPs). The latter also produce electricity. Over the past 10 years, the distribution of heat produced in BHs and CHPs has changed significantly. The heat supply of the Latvian energy sector is a system consisting of three main elements – heat source, transmission and distribution networks, and end consumer. Low efficiency of heat supply system elements creates risks to security of heat supply, resource sustainability and competitiveness. Increasing energy efficiency in the system as a whole, or in individual elements of the system, will promote the enhancement of the heat supply sector, while promoting economic growth as well. The research attempts to evaluate the energy efficiency of DH systems in the so-called left bank (*hereinafter* – LB) DH area (located on the left bank of the Daugava River in Riga).

***Keywords**: District heating, heat sources, heat supply systems, left bank of the Daugava River in Riga, weather conditions.*

1. DESCRIPTION OF RIGA SUPPLY SYSTEM

1.1. Characteristics of Heat Supply System Operation and Heat Sources

Riga is the capital of Latvia and the largest industrial and financial centre in the Baltics, as well as an important port city. With a population of 621,120 (in 2020), it is the largest city in the Baltic States and the third largest city (after St. Petersburg and Stockholm) in the entire Baltic Sea region [1]. The area of the city is 307.17 km^2. About one third of all population of Latvia live here, and 0.94 million people in Riga agglomeration (Riga and surrounding areas, including the nearest municipalities), which is almost half of the total population of Latvia. Riga is located in the central part of the country, on the southern coast of the Gulf of Riga, in the lowlands of the Central Latvia – plains of Riga and Tireli, on both banks of the Daugava River. Riga is a typical lowland town with separate hills, the highest of which is Dzeguzkalns – 26 meters above sea level. The average surface height is about 6 meters above sea level [2].

In Latvia, 65–70% of energy is consumed for heating needs, but 30–35% for hot water preparation [3]. In Latvia, heat of DH consumers is produced both in boiler houses (*hereinafter* – BHs) and cogeneration plants (*hereinafter* – CHPs). The latter also produce electricity. Over the past 10 years, the distribution of heat produced in BHs and CHPs has changed significantly [4].

DH system of LB started to develop in the 1960s, when the construction of the multi-storey buildings in the residential area of Agenskalns began, soon followed by the construction of the Grivas Street district, Ilguciems, Imanta and other neighbouring residential areas. Heat supply, including to industrial facilities, was provided from CHP “Zasulauks” (boilers in operation since 1961) and several BHs, which currently are long out of the operation and decommissioned [5].

In the 1970s, due to expansion of Imanta residential area, construction of CHP “Imanta” begun. The plant was commissioned in the early 1980s. Also, due to expansion of Ziepniekkalns residential area and the construction plans of the Robot Factory, CHP “Ziepniekkalns” was constructed as well. In these heat sources, the natural gas and fuel oil were used as fuel. Currently, CHP “Imanta” is the third largest heat source in Riga after Riga CHP-1 and Riga CHP-2 owned by JSC Latvenergo. As both Riga CHPs are located on the right bank of the Daugava River, CHP “Imanta” is the largest heat source in LB DH area. It is also the largest LB DH supply system.

The second largest LB DH supply system is the one of Bolderaja, where BH Gobas 33A and BH Keramikas 2A are combined. The next largest system is LB DH supply system of CHP “Daugavgrīva”. The smallest LB DH supply system is the one centred around BH Bauskas 207A.

The heat energy market with the entry of independent producers in LB DH supply system has not been developed yet.

Table 1. Heat Energy Balance in Riga Region

	Year									
Heat energy balance in Riga region	2010	2011	2012	2013	2014	2015	2016	2017	2018	2019
Heat energy produced, GWh	4225	3484	3709	3833	3739	3598	3929	4151	3412	3377
Grid loss, GWh	512	454	466	452	423	400	425	438	445	400
Heat energy delivered to consumers, GWh	3686	3006	3217	3366	3225	3129	3674	4027	2916	2900
Heat energy delivered to households, GWh	2529	2229	2382	2238	2165	2083	2302	2356	2342	2313
Number of BHs	65	66	67	64	63	65	67	64	68	68
Total installed heat capacity, MW	665, 9	621, 2	616, 4	422, 2	421, 2	419, 4	421, 2	339, 6	374, 4	257
Number of CHPs	14	15	16	20	19	21	21	21	19	20
Total installed heat capacity, MW	876.3	877.8	881.0	1059	1055.9	1060	1059.9	1059.3	1059.5	1059.5

JSC Rīgas Siltums (*hereinafter* – RS) is the largest district heating company in Latvia and the Baltic States, which produces heat, provides its transmission, distribution and sales. RS offers heat energy users some additional services like maintenance of internal heating systems of buildings. RS is also the largest supplier of heat energy in Riga. 93 % of the total revenue of RS is obtained from sales of heat energy. 76 % of all heat energy required in Riga is produced, transmitted and distributed by RS. 77 % of the heat supplied by the company is used for residential heating and hot water supply [6]. RS produces heat in 45 heat sources: 5 CHPs and 40 BHs, which provide 32 % of the total heat transferred in Riga DH networks. The remaining 68 % of the heat energy is purchased from other producers. In the financial year of 2019/2020, RS purchased heat energy from six independent producers. 65.9 % of the purchased heat energy was supplied from JSC Latvenergo TEC-1 and TEC-2, but the remaining 34.1 % from other heat energy producers: 12 % from Ltd Rīgas BioEnerģija, 8.2 % from Ltd Rīgas enerģija, 7 % from Ltd Energia Verde, 3.7 % from Ltd Eco Energy and 3.2 % from Ltd Juglas jauda [7].

In line with heat production, electricity is produced in the cogeneration process, a part of which is used by RS in its production sources, but the rest is sold [10]. Revenue from electricity sales accounts for about 6.4 % of its total revenue. Electricity cogeneration took place in six heat sources, but in three of them electricity production took place only for needs of the company itself [11].

RS mainly uses natural gas and wood chips for heat energy production, the share of the natural gas is 65 % of the total fuel consumption. Fuel oil or labelled diesel fuel is intended to be used as a reserve fuel for heat production.

2.1. Technical Condition of DH Network

The reliability of DH and sustainability of the heat supply depend on the technical condition of heating networks. RS uses heating networks with an approximate length of 818 km for heat supply. The total length of the heating networks owned by the company is 684 km, including 280.82 km of ductless heating network [2]. In financial year 2019/2020, several sections of the heating network, which were characterised by a large number of leaks and caused interruptions in the heat supply, were renovated. In total, 15.91 km of heating networks were renovated, including 13.92 km using industrially insulated pipelines. Implementing the goals of RS to attract new customers, 3.4 km long new DH networks were built in Riga. In financial year 2018/2019, 9.38 km of DH networks and 8.31 km of industrially insulated pipelines were built and renovated. 2.9 km of them were built, using ductless technology, which helped increase the efficiency of the heat supply system and reduce the heat energy losses. In financial year 2019/2020, heat energy losses were 374 thousand megawatt-hours (*hereinafter* – MWh) or 11.77 % of total heat energy supply.

RS transmits and sells heat energy to users in Riga and Dreiliņi, Stopiņi municipality. The heat supply area of RS is 307.30 km^2. In financial year 2019/2020, RS started delivering heat energy to 61 new users with a total planned heat load of 29.7 MW [10]. It provides heat supply in Riga to almost 8 thousand objects, including more than 5.5 thousand homes.

RS invests in innovations and aims at reducing the cost of heat production by rationally using all types of available energy resources. The task of RS is to provide Riga with a safe, high-quality, environmentally friendly and sustainable DH. In financial year 2019/2020, it continued to increase the security of heat supply. CHP “Imanta” control system of water pumps and water heating boilers were modernized, CHP SC “Zasulauks” water chemical treatment system was upgraded and CHP “Ziepniekkalns” performed the reconstruction of the ash discharge system. BH Gobas 33A modernized the water heating boiler control system and boiler burners as well [10].

2. THE HEAT DEMAND AND HEAT LOADS IN LB DH AREA

As mentioned above, LB district heating system is divided into four DH zones, which are rather different in their size and complexity [11].

In order to estimate the amount of energy consumed for heating in cases where the assessment period is less than five full years, the measured energy consumption can be adjusted for climatic conditions to ensure that the energy consumed during the measurement period corresponds to the average local climatic conditions. Climatic data framework of this work was taken from the Latvian construction standard LBN 003 “Construction climatology” (*hereinafter* – LBN 003) [12], [13].

To calculate the maximum heating load, the coldest five-day average air temperature from the Latvian construction LBN 003 was used. It should be noted that in the assessment period from 2010 to 2020, the above-mentioned standard was changed twice – in 2015 and 2019. The main parameters for the operation of the heat supply system approved in 2001 and 2015, however, remained the same: the average air temperature in the coldest five days in Riga was -20.7 °C, the heating period was 203 days (4872 hours) and the average outdoor temperature was 0.0 °C during the period. In 2019, the data of LBN 003 were corrected: the average air temperature in the coldest five days in Riga was -20.0 °C, the heating period was 192 days (4608 hours) and the average outdoor temperature during the heating period was 1.1 °C [12].

To estimate the amount of heat demand, a correction for heat consumption was performed using the equation:

$$Q_{apk} = Q_1 \cdot \frac{T_1 - T_2}{T_2 - T_3}$$

where Q_{apk} – the adjusted heat consumption (MWh);

Q_1 – heat energy consumption in the assessment period (MWh);

T_1 – standard indoor temperature of the building (18 °C);

T_2 – average outdoor temperature, according to LBN 003 (°C);

T_3 – actual average outdoor temperature during the assessment period (°C).

Correction of the produced heat energy was performed taking into account the actual and normative outdoor temperatures.

Table 2. Duration of Heating Season and Average Outdoor Temperature, 2010–2020

Heating season	Beginning of the season	End of the season	Duration of the season	Average outdoor t °C
2010/2011	October 12	April 21	192	-0.4
2011/2012	October 14	April 23	193	1.4
2012/2013	October 12	April 23	194	-0.3
2013/2014	October 11	April 28	200	3.4
2014/2015	October 6	April 30	207	3.1
2015/2016	October 6	April 28	206	2.7
2016/2017	October 10	April 15	218	2.2
2017/2018	October 5	April 26	204	2.0
2018/2019	October 5	April 24	202	2.9
2019/2020	September 26	May 7	225	5.7
Average			204	2.3

The calculations were made with an adjustment, assuming that the amount of heat energy for hot water production was 15 % of the total volume and that changes in the outdoor temperature during the lowest temperature period did not affect the amount of heat energy consumed for hot water production.

3. EVALUATION OF DATA ACQUIRED OVER A TEN-YEAR PERIOD

The amount of the heat energy produced and transferred to customers is determined by several factors: to the greatest extent it is influenced by climatic conditions during the heating season, affecting the consumption of the heat for heating, ventilation and hot water preparation; smaller effect is produced by the heat energy consumed during the summer, taking into account the differences in cold water temperature during cold and hot summer; by amount of heat loads connected to the DH system [14].

The authors of the research analysed the volume of heat produced in the past 10 years and data on the average and maximum outdoor temperatures of the heating season.

The maximum outdoor temperatures were assessed and trends in heat load changes noted. In addition, information was provided for 2020/2021, as after several years, the average outdoor temperature actually came close to the coldest five-day average air temperature of -20.0 °C specified in 003-19.

The trends of the past 10 years are as follows:

- an increase in the average temperature of the heating season to a record warm temperature in the heating season of 2019/2020;
- the absence of the lowest outdoor temperature (reaches the normative temperature of the coldest 5 days), last established in 2012;
- extension of the duration of the heating season.

For comparison, the lowest average daily temperature over the past 10 years was -23.7 °C on 20 January 2006, in the heating season of 2005/2006, where the average outdoor temperature reached -1 °C with a heating period of 193 days.

3.1. Maximum Heat Load of LB Heating Systems

For the analysis of changes in heat load over a 10-year period, recalculation must be performed according to the algorithm, recalculating the actual lowest daily average heat loads for the 5 coldest days of the standard outdoor air calculation. For the comparison of loads, the average heat loads of the coldest 4 days of the 10-year period were selected:

- 27 January 2010 -20.3 °C;
- 3 February 2012 -21.2 °C;
- 8 January 2016 -17.7 °C;
- 17 January 2021 -15.1 °C.

Table 3. Average Daily Heat Load of LB Heat Supply Systems and Separate Heat Sources on the Coldest Days of Winter in 2010–2021

Heat source	**Heat load, MW**				
CHPs					
Imanta	445.10	254.88	265.43	224.19	221.83
Zasulauks	195.09	-	-	1.63	-
Ziepniekkalns	112.00	48.91	53.00	53.6	47.30
Daugavgriva	24.14	16.05	16.35	14.34	13.07
Automated natural gas BHs with installed capacity above 1 MW					
Gobas 33A	20.00	9.47	9.78	10.74	10.35
Keramikas 2A	12.97	9.38	9.77	6.52	6.35
Kugu 26A	18.00	17.80	13.34	16.23	15.22
Bauskas 207A	6.00	2.77	2.81	2.39	2.97
Svīres 15	1.60	0.50	0.50	0.61	-
Automated natural gas BHs with installed capacity below 1 MW					
Kalnciema 106F	0.53	0.28	0.24	0.25	0.21
Atgazenes 26	0.30	0.16	0.15	0.14	0.16
Biesu 6	0.30	-	-	-	0.14
Baldones 8	0.19	0.11	0.14	0.13	0.11
Ernestines 30	0.18	0.13	0.13	0.11	0.10
Baldones 2	0.17	0.09	0.11	0.10	0.08
Robezas 3/9	0.10	0.04	0.04	0.03	0.04
Kaletu 10A	0.04	0.02	0.03	0.02	0.02

Taking into account that since 2012 the lowest outdoor temperatures have not reached the normative 5 coldest day limit, it is necessary to recalculate the same conditions in order to be able to draw conclusions about the trend of changes in heat load. When performing the comparison, the capacities of heat sources must be grouped according to the heat supply systems:

- CHP “Imanta” connected to the combined heating networks (CHP “Imanta”, CHP “Ziepniekkalns”, CHP “Zasulauks”, BH Kugu 26A);
- Bolderāja combined heating networks: BH Gobas Street 33A and BH Keramikas 2A;
- CHP “Daugavgriva”;
- BH Bauskas 207A and the other 36 automated natural gas BH with a capacity of less than 1 MW do not require such recalculation. These BH supply heat energy mainly to one separate building and the changes in loads are related only to the reconstruction works of the buildings to be performed in certain cases, during which the load is reduced. Some buildings have been renovated, but no significant changes in heat consumption and load reduction have been observed.

Table 4. Evaluation of Changes in Heat Load for a 10-Year Period (Grid District, MW)

Grid area	**27 January 2010**	**3 February 2012**	**8 January 2016**	**17 January 2021**
	Heat load, MW	Heat load, MW	Heat load, MW	Heat load, MW
United Grids of CHP “Imanta”	320	322.5	315.4	326
United Grids of Bolderaja	18.8	19	18.4	19.2
CHP “Daugavgriva”	16	15.9	15.3	15
BH Bauskas 207A	2.7	2.6	2.5	3.4

Analysing the recalculation of heat loads to the coldest five-day average temperature in Riga, the trend of increasing heat loads is seen, except for CHP “Daugavgrīva”:

- CHP “Imanta” combined heating networks: + 2.2 %,
- Bolderaja heating networks: + 2.1 %
- CHP “Daugavgriva” - 6.3 %,
- BH Bauskas 207A + 26 %.

The increase in heat load of BH Bauska 207A is the largest one and can be explained by the connection of new residential buildings [8].

In order to examine the trends in heat load, an additional comparison was made for the time period between 2010 and 2021 with similar outdoor temperatures, looking for the longest possible period of time with a low stable outdoor temperature. Selected periods are summarised in Table 5.

Table 5. Outdoor Temperatures for Heat Load Comparison Periods (Meteorological Station of CHP “Imanta”)

Date	**Average temperature, meteorological station, CHP “Imanta”**	**Date**	**Average temperature, meteorological station, CHP “Imanta”**
9 January 2010	-10.9	6 February 2021	-10.1
10 January 2010	-11.9	7 February 2021	-11.5
11 January 2010	-10.7	8 February 2021	-11.8
12 January 2010	-13	9 February 2021	-9.3
13 January 2010	-10.1	10 February 2021	-12.5
14 January 2010	-11.8	11 February 2021	-11
Average	-11.6	Average	-11

Table 6. Comparison of Heat Loads in the Heat Supply System of CHP "Imanta" in 6-Day Periods in 2010 and 2021

Heat source	**Average heat load, 9 January 2010 – 14 January 2010, MWh**	**Average heat load, 6 February 2021 – 11 February 2021, MWh**
CHP Imanta	193.4	197.3
CHP Zasulauks	0	2
Kuģu 26A	16.7	7.4
CHP Ziepniekkalns	37.8	47.2
Total	248	253.9
Total (with conversion to the same air temperature (k = 1.0152))	248	257.7 (an increase by 3.9 %)

Table 7. Heat Loads of LB Heat Supply Systems

Heat source	**Heat load, MW**	**Actual average daily heat load, 17 January 2021, MW**	**Heat load recalculation and calculated temperature, -23.9 °C, MW**	**Heat load recalculation and calculated temperature, -20 °C, MW**
United Grids of CHP Imanta				
CHP "Imanta"	445.1	221.8	276.9	254.7
CHP "Zasulauks"	195.05	0	0	-
CHP "Ziepniekkalns"	112	47.8	59.7	54.9
BH Kugu 26A	18	15.2	19	17.5
Grid of CHP Daugavgriva				
CHP "Daugavgriva"	24*	13.1	16.3	15
United Grids of Bolderaja				
BH Gobas 33A	20	10.4	12.9	11.9
BH Keramikas 2A	12.97	6.35	7.9	7.3
United Grids of BH Bauskas 207A				
BH Bauskas 207A	6	2.4	-	2.7
BH Svires 15	1.6	0	-	0
BH not included into united grids of LB				
BH Kalnciema 160F	0.530	0.21	-	0.24
BH Sampetera 98	0.340	0.12	-	0.14
BH Atgazenes 26	0.300	0.16	-	0.18
BH Biesu 6	0.300	0.14	-	0.16
BH Baldones 8	0.199	0.11	-	0.13
BH Ernestines 30	0.180	0.10	-	0.11
BH Baldones 2	0.170	0.08	-	0.09
BH Robezu 3/9	0.100	0.04	-	0.05
BH Kaletu 10A	0.042	0.02	-	0.02

*- CHP "Daugavgriva" installed capacity after reconstruction, assuming that the steam boiler DKVR 10/13 is out of service

The calculation shows that the differences in heat loads are minimal. Over 10 years, the increase in heat load compared to a 6-day period in 2010 and 2021 (see Table 6) is 3.9 %.

Such a comparison should be considered more accurate than a comparison of the individual coldest winter days. It can be concluded that in the heat supply system of LB during 10 years there is a slight tendency towards an increase in heat loads, with exception of CHP "Daugavgriva" and small automated BH. This trend is related to the connection of new customers to the DH system. In CHP "Daugavgriva" and in the small automated gas BH, the connection of new customers has not taken place.

To assess the heat load of the LB heat supply system from the point of view of safety of heat energy supply and the adequacy of reserve capacities, the operation data of the coldest day of January 2021 (17 January 2021) with an average temperature of -15.1 °C were used. It was converted to the average temperature of the five coldest days specified in LBN 003-19. The results are provided in Table 7.

3.3. Principles for Evaluating Heat Production Capacity Reserves

Capacity must be reserved in the heat supply in order to meet the demand for heat production during the coldest 5-day average period by disconnecting one of the most powerful heat production facilities.

Table 8

Heat capacity, MW	**Minimum number of boilers**	**Power reserve when the boiler with the highest capacity stops**
Over 10 MW	3	100 %, outdoor temperature, -23.9 °C
4 to 10 MW	3	100 %, outdoor temperature, -20 °C
1 to 4 MW	2	100 %, outdoor temperature, -20 °C
0.5–1 MW	2	100 %, outdoor temperature, -10 °C
0.2–0.5 MW	2*	
Less than 0.2 MW	1	

* in range of heat sources from 0.2 MW to 0.5 MW it is allowed to install one condensing boiler, if the boiler consists of several modules equipped with separate burners.

In addition, there must be a reserve of power so that, at the lowest outdoor temperature, when a more powerful installation is switched off, the heat generating installations can restore the parameters required for the heat supply. If the available capacity of the equipment were equal to the heat load, it would be impossible to increase the temperature of the heat carrier to the required value in the event of a heat supply interruption.

In assumption of the power reserve calculation algorithm, additional conditions were offered:

- biofuel supply crisis is possible in winter due to long-term unfavourable climatic conditions during wood chip accumulation and difficult access to wood resources in forests (last supply crisis in 2018);
- disturbances caused by difficult traffic due to road icing and snow;
- during the winter period, biofuel boilers may malfunction due to freezing chips and cause wood chip supply difficulties, as well as ice pieces may cause damage to the conveyor and burning disturbances, if the ice enters the furnace.

During this period, the natural gas supply disruptions caused by limited natural gas supply are possible, but RS has not encountered such a situation, as it has always purchased natural gas for the entire heating season [15].

The natural gas boilers have a higher level of safety due to the possibility to produce heat with emergency fuel diesel, as the boilers are equipped with combined burners and the heat source is equipped with an emergency fuel system. The capacity of CHP units is not used in the calculation of reserve capacity, as these units operate according to the demand of the electricity market. This does not apply to self-consumption equipment. Recommendation is to calculate the power reserve, taking into account both the shutdown of the most powerful boiler and the reduction of the maximum capacity of biofuel boilers by 50 % during the lowest outdoor temperatures.

3.4. Hydraulic Inspections of Heating Networks and the Pace of Renovation of Heating Networks

Hydraulic testing (*hereinafter* – HT) is the most effective method to ensure the safety of heating networks by reducing the number of possible heating network failures or leaks during the heating season. During HT, each section of the heating network is tested under elevated pressure. In order to find the weakest points and leaks of the heating networks, 13 HT are performed per year, 4 of them in LB. In accordance with RS "Operating Instructions for Water Heating Networks" (28 May 2015), as well as to ensure a continuous supply of heat to its heat energy users during the heating season, This used to check the tightness of pipes, fittings, flange connections and expansion joints. The flow and return pipes for each section of the heating network shall be tested at a pressure 1.25 times the working pressure.

The tests are performed with water from the heating network, the temperature of which does not exceed 45 °C. During the test, the heating units and heating systems of the heat energy users are safely disconnected from the heating networks. HT is carried out in accordance with approved work programs and their results are reported.

Table 9. Number of Leaks Detected as a Result of Hydraulic Inspections of LB Heating Networks in 2016–2020

Heat source	**2016**	**2017**	**2018**	**2019**	**2020**
LB					
CHP "Imanta"	5	9	5	4	8
CHP "Ziepniekkalns"	1	4	7	3	3
CHP "Daugavgriva"	2	4	1	*	*
BH Gobas 33A	-	1	-	-	-
BH Keramikas 2A	-	-	-	*	*
BH Bauskas 207A/ Svires 15	-	-	-	-	-
LB total	8	18	13	7	11

*- according to the decision of the Technical Commission of 9 May 2019, in heating networks, where all pipelines are built in ductless technology, the pipeline alarm is in working order and does not show signs of damage, it is decided to perform a hydraulic inspection of heating networks once every 4 years

The number of leaks in 2019 was the lowest over the last 5 years (see Table 9). Out of 57 leaks in 2020, only 2 leaks were detected in the main heating networks.

4. CONCLUSIONS

From heating season 2010/2011 until heating season 2019/2020, the heat load of the LB heating area did not change a lot [16]. The duration of the heating season increased, the average outdoor air temperature increased and an average required heat load decreased. This overall trend also refers to the processes in LB heating area.

It was also established that development of heat supply infrastructure was positive in the designated period of time, and large parts of LB heating area were subjected to reconstruction and upgrading, which resulted in the increased energy efficiency of heating supply infrastructure and reduced number of leaks and heat energy loss. The data of heating network hydraulic inspections in 2020 performed in heating areas of the biggest heat sources of LB – 3 CHPs and 3 BH show that actual number of leaks reached 11, which is a fairly good result. However, the work continues to reduce the number of leaking incidents even more and keep this reduction stable.

In order to ensure heat energy security of supply in LB heating area, it was proposed to work on further diversification of heat supply sources, focusing more on wooden biomass. The capacity of CHP units was not used in the calculation of reserve capacity, as these units operate according to the demand of the electricity market. This does not apply to self-consumption equipment.

It was noted that over the ten-year period the natural gas supply disruptions caused by limited natural gas supply were theoretically possible, but RS did not encounter such a situation, as it always purchased natural gas for the entire heating season.

ACKNOWLEDGEMENTS

The research has been supported by the National Research Programme, project “Trends, Challenges and Solutions of Latvian Gas Infrastructure Development” (LAGAS) (No. VPP-EM-INFRA-2018/1-0003).

REFERENCES

1. RPR. (2016). Rīgas plānošanas reģiona siltumapgādes attīstības rīcības programma. Available at https://rpr.gov.lv/wp-content/uploads/2018/02/RPR_siltumapg%C4%81des-programma.pdf
2. EM. (2020). Siltumenerģijas ražošana. Available at https://www.em.gov.lv/lv/siltumenergijas-razosana
3. CSP. (2021). Iedzīvotāju skaits gada sākumā, tā izmaiņas un dabiskās kustības galvenie rādītāji reģionos, republikas pilsētās, novadu pilsētās un novados - Rādītāji, Teritoriālā vienība un Laika periods. Available at https://data.stat.gov.lv/pxweb/lv/OSP_PUB/START__POP__IR__IRS/IRS030/table/tableViewLayout1/
4. Krišjāne, Z., & Zira, M. (2018). Rīgas aglomerācija– vai tikai iedzīvotāju mobilitāte? 76th international scientific conference of the University of Latvia. Available at https://www.geo.lu.lv/fileadmin/user_upload/lu_portal/projekti/gzzf/Konferences/EGEA/Krisjane_Zira_Rigas_aglomeracija.pdf
5. RS. (n.d.). History of District Heating in Riga. Available at https://www.rs.lv/en/content/history

6. RS. (n.d.). JSC Rīgas siltums. About Company. Available at https://www.rs.lv/en/content/jsc-rigas-siltums
7. RS. (2021). Starpperiodu pārskats par periodu no 2020.gada 1.oktobra līdz 2021.gada 30.jūnijam. Available at https://www.rs.lv/sites/default/files/page_file/starpperiodu_parskats_par_periodu_no_2020.gada_1.oktobra_lidz_2021.gada_30.junijam.pdf
8. Oleksijs, R., Sauhats, A., & Olekshii, B. (2021). Power Plant Cooperation in District Heating Considering Open Electricity Market. *Latvian Journal of Physics and Technical Sciences, 58* (3), 66–81. doi: 10.2478/lpts-2021-0017
9. Savickis, J., Zeltins, N., & Jansons, L. (2019). Synergy between the Natural Gas and RES in Enhancement of Security of Energy Supply in the Baltic Countries (Problem Statement). *Latvian Journal of Physics and Technical Sciences, 56* (6), 17–31. doi: 10.2478/lpts-2019-0032
10. RS. (2021). Gada pārskats 2020. Available at https://www.rs.lv/sites/default/files/page_file/rs_gada_parskats_2020.pdf
11. Zemite, L., Kutjuns, A., Bode, I., Kunickis, M., & Zeltins, N. (2018). Risk Treatment and System Recovery Analysis of Gas System of Gas and Electricity Network of Latvia. *Latvian Journal of Physics and Technical Sciences, 55* (5), 3–14. doi: 10.2478/lpts-2018-0031
12. Cabinet of Ministers. (2001). *Regulations regarding the Latvian Building Code LBN 003-01 "Construction Climatology"*. Available at http://webcache.googleusercontent.com/search?q=cache:JwM5BK5VWNEJ:www.vvc.gov.lv/export/sites/default/docs/LRTA/Citi/Cab._Reg._No._376_-_LBN_003-01_Construction_Climatology.doc+&cd=1&hl=ru&ct=clnk&gl=lv
13. Cabinet of Ministers. (2019). *Noteikumi par Latvijas būvnormatīvu LBN 003-19 "Būvklimatoloģija"*. Available at https://likumi.lv/ta/id/309453-noteikumi-par-latvijas-buvnormativu-lbn-003-19-buvklimatologija-
14. Paardekooper, S., Lund, R. S., Mathiesen, B. V., Chang, M., Petersen, U. R., Grundahl, L., … & Persson, U. (2018). *Heat Roadmap Europe: Quantifying the Impact of Low-Carbon Heating and Cooling Roadmaps. Aalborg Universitetsforlag. Available at file:///C:/Users/OS00083/Downloads/Attachment_0.pdf*
15. Zemite, L., Nevercika, E., Jansons, L., Bode, I., Koposovs, A., Kondrahins, N., & Jasevics, A. (2021). The Natural Gas Supply of the Latvian Municipality during the Local Energy Crisis. *Latvian Journal of Physics and Technical Sciences, 58* (3), 186–200. doi: 10.2478/lpts-2021-0025
16. RS. (2016). *AS "Rīgas siltums" 20 gadu laikā sasniedzis nozīmīgus rezultātus siltumenerģijas ražošanā, pārvadē un klientu apkalpošanā*. Available at https://www.rs.lv/lv/aktualitates/rigas-siltums-20-gadu-laika-sasniedzis-nozimigus-rezultatus-siltumenergijas-razosana

sciendo

LATVIAN JOURNAL OF PHYSICS
AND TECHNICAL SCIENCES
2022, N 3

DOI: 10.2478/lpts-2022-0016

ON THE ISSUE OF COLLISION OF BALLS IN AN AUTO-BALANCING DEVICE

G. Strautmanis[1], I. Schukin[2], G. Filimonikhin[3], M. Mezitis[4],
I. Kurjanovics[5], I. Irbe[6]*

[1, 5, 6] Latvian Maritime Academy,
5B Flotes Str., LV – 1016, Riga, LATVIA
[2] Riga Technical University,
Riga, LATVIA
[3] Central Ukrainian National Technical University,
Kropyvnytskyi, UKRAINE
[4] Transport Academy,
Riga, LATVIA
*e-mail: ineta.irbe@latja.lv

The paper considers a model of a vertical double pendulum, which includes two balls suspended on rigid non-deformable threads to one centre of the suspension. For the proposed system of pendulums, differential equations of motion and conditions for collision of balls have been recorded. When simulating the motion of the pendulums, the central collision of the balls has been considered for various options of the motion of the suspension point: the suspension point is motionless; the suspension point oscillates in the vertical direction; the suspension point makes rotational motions in the vertical plane. Meanwhile, various conditions for the central collision between the balls have been considered: a perfectly inelastic collision; a perfectly elastic collision; a collision with transformation of collision energy (partially elastic collision). The results of numerical simulation are consistent with the behaviour of pendulums in real physical models, which makes it possible to simulate an elastic collision between balls when studying their acceleration in auto-balancing devices.

Keywords: *Balls, centre of suspension, elastic collision, equations of motion, pendulum.*

1. INTRODUCTION

During the acceleration and deceleration of the rotor with an auto-balancing device, in which the balls can freely move relative to the body, their intense collision occurs. The impact of such interaction between the balls on the transient processes of the rotor has not been sufficiently studied due to the transience of the rotor acceleration process and the difficulty to describe the nature of the motion and collision of the balls. It is known from publications [1] that when balls collide with each other, their elastic deformation occurs. The kinetic energy of the balls is partly converted into potential energy of deformation and partly into the internal energy of the body, which causes an increase in the temperature of the balls. In an auto-balancing device containing several balls, their multiple collisions occur, which gradually equalize their velocity and contribute to the establishment of the auto-balancing mode. At the same time, in publications [2]–[7], where transient modes in auto-balancing devices (hereinafter ABD) with several balls are considered, an assumption is made that during acceleration the balls move with the ability to pass through each other and the collisions between balls are not taken into account.

There is also a known model of a pendulum with a suspension point oscillating in a vertical plane, described in [8] and called the Kapitza's pendulum. In [9], the study of the motion of a pendulum with an oscillating suspension point was carried out by computer simulation. This ensured obtaining numerous modes of the pendulum behaviour. The studies in these papers showed that with an increase in the amplitude of the angular oscillations of the pendulum, the period of its natural oscillations increased.

In the proposed paper, a model of a double pendulum in the form of identical balls suspended on an inextensible thread, with one common suspension point, is considered. When pendulums oscillate, a collision, either elastic or perfectly inelastic, occurs between the balls. In the case of an elastic collision, the balls might stick together, as a result of which the double pendulum system begins to behave as a simple pendulum. The suspension point of the pendulums can also be motionless or perform various motions: oscillate in the vertical plane [8] or make rotational motions. Similarly, the centre of the ABD makes circular motions in the horizontal or vertical plane, which makes the model of a double pendulum with an oscillating suspension identical in terms of the issue on studying the impact between the balls in the ABD [12], [13]. In order to refine computer modelling in the study of collision, it is proposed to consider a model of a double pendulum with various options for the motion of the suspension point: fixed point; oscillating along the vertical axis; rotating in the vertical plane.

The study of the issue of multiple collision of the balls is of certain interest for modelling transient processes in the ABD. In this paper, the central collision between the balls is studied on the basis of a mathematical model of a double pendulum with a common suspension point.

2. MECHANICAL MODEL OF A DOUBLE PENDULUM

The physical model of a system of two balls is shown in Fig. 1. The balls have the same mass m and radius r, and are suspended on an inextensible rigid thread of length l. The suspension point of the balls can remain at rest or make circular motions in the vertical plane along a trajectory in the form of a circle of radius e, while a dissipative momentum acts at the suspension point of the pendulums, with a dissipation coefficient b.

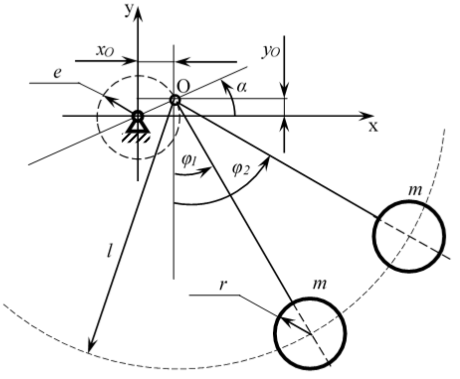

Fig. 1. A calculation model of a double pendulum with a rotating suspension point.

Let us choose a fixed coordinate system xOy and associate it with a fixed point around which the suspension point of the pendulum system (point O) rotates. The equations of motion of the centres of mass of the balls that make up a system of the pendulums are derived on the basis of Lagrange's equations of the second kind:

ddt∂Tqi-∂Tqi+Rdqi+qi=Qi, (1)

where
T – kinetic energy of the rotor system;
Π – potential energy of the system;
Rd – dissipative function in generalized coordinates;
Qi = 0 – generalized strength.

The coordinates of each pendulum are determined by the angle of deviation of the thread from the vertical (angles φ1 and φ2) and the coordinate of the suspension point O.

xi=x0+l·sin i =e·cos +l·sin i ; (2)

yi=y0-l·cos i =e·sin -l·cos i. (3)

The velocity of the motion of the centres of ball masses is determined using the expressions:

xi=-e·sin +l·icos i ; (4)

yi=e·cos +l·i. (5)

To determine the kinetic energy of the system, we determine the squares of the velocities of each oscillating mass:

Vi2=xi2+yi2=e22+l2i2+2elisin i-α. (6)

The kinetic energy of the system is determined from the known expression, and after transformation is

T=miVi22=me22+ml212+222+mel1sin 1-α +2sin 2-α. (7)

The potential energy of the system arises due to the vertical displacements of the centre of load masses:

=mgl-lcos 1 +esin +mgl-lcos 2 +esin =
=2mgl-mglcos 1 +cos 2 +2mgesin. (8)

The impact of dissipative forces in the pivot suspension of pendulums is taken into account by introducing equivalent viscous friction. According to the hypothesis of dissipative forces, the resistance in the pivot is assumed to be proportional to the angular velocities of the oscillatory motions of the pendulums. In accordance with the hypothesis, the dissipative function at the suspension point is as follows:

R=kil2i22, (9)

where k_i – dissipation coefficient of the i-th ball at the suspension point.

The partial derivative of the kinetic energy with respect to velocity 1 and 2 is as follows:

∂Ti=ml2i+melsin i-α; (10)

ddt∂Ti=ml2i+melsin i-α -mel2cos i-α +melicos i-α. (11)

The partial derivative of the kinetic energy with respect to coordinates 1 and 2 is as follows:

∂Tqi=melicos i-α. (12)

The partial derivative of the potential energy with respect to coordinates 1 and 2 is as follows:

qi=mglsin i. (13)

The partial derivative of the dissipative energy with respect to angular velocities 1 and 2 is as follows:

Rqi=kil2i. (14)

When solving Eq. (1) taking into account Eqs. (11)–(14) provided that bi=ki/m, we obtain the differential equations of motion of the pendulum system with unsteady motion of the suspension point of the balls:

1+elsin 1-α -el2cos 1 cos +sin 1 sin +b11+glsin 1 =0; (15)

2+elsin 2-α -el2cos 2 cos +sin 2 sin +b22+glsin 2 =0. (16)

If we assume that the suspension point of the pendulums O rotates at a constant velocity, i.e. the motion of the suspension point is fixed (= 0; = = const; α=ωt), then the equations of motion are as follows:

1-el2cos 1 cos ωt +sin 1 sin ωt +b11+glsin 1 =0; (17)

2-el2cos 2 cos ωt +sin 2 sin ωt +b22+glsin 2 =0. (18)

Let us consider the motion of a pendulum system with a vertically oscillating suspension point. The physical model of such a system is shown in Fig. 2.

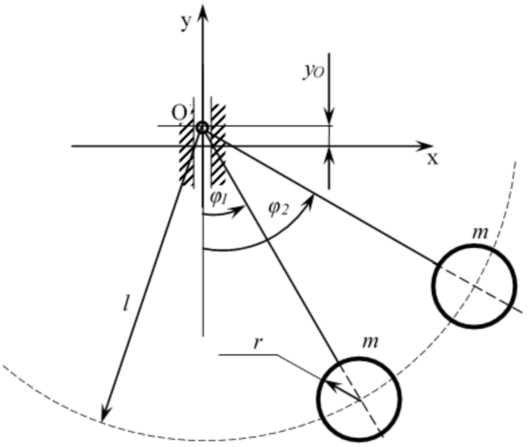

Fig. 2. A calculation model of a double pendulum with an oscillating suspension point.

The coordinates of each pendulum in this case are determined by the following dependencies:

xi=l·sin i; (19)

yi=y0-l·cos i =e·sin ωt -l·cos i. (20)

Having carried out all the transformations, provided that the dissipation coefficients are equal to zero (bi = 0), we obtain a system of differential equations consistent with the Kapitza’s equation [8] for a pendulum with an oscillating suspension point:

1+glsin 1 -el2sin ωt sin 1 =0; (21)

2+glsin 2 -el2sin ωt sin 1 =0. (22)

It turns out that for the transition from equations with a rotating suspension point Eqs. (17) and (18) to equations with a suspension point oscillating in the vertical plane Eqs. (21) and (22), it is necessary to exclude from the former the expressions containing the projection of the eccentric on the horizontal axis x – ecos ωt.

If we assume that the suspension point of the pendulums is fixed (the radius of the trajectory of motion of the point O e = 0), then the system of equations (21)–(22) as well as the system of equations (17)–(18) in the absence of dissipation (b1 = b2 = 0), is as follows:

1+glsin 1 =0; (23)

2+glsin 2 =0. (24)

3. BALL COLLISION

The authors of the paper consider the following cases of collision between the balls:

1. Central perfectly inelastic collision of two balls at a fixed suspension point;
2. Central perfectly elastic collision of two balls at a fixed suspension point;
3. Central partially elastic collision of two balls at a fixed suspension point;
4. Central perfectly elastic collision of two balls at a movable suspension point.

When the balls collide, the velocity of the balls changes almost instantly (in a very short period of time). Changes in angular velocities depend on the nature of the collision and in the case of equality of the ball masses are expressed by the equations [2]:

1=10+202-kd10-202; (25)

2=10+202+kd10-202, (26)

where
10, 20 – angular velocity of the balls before the collision;
1, 2 – angular velocity of the balls after the collision;
kd – a coefficient of restitution at a perfectly inelastic collision kd = 0; at a perfectly elastic collision kd = 1; at a partially elastic collision kd < 1.

As the initial conditions of motion, the initial angle of deviation of the ball from the vertical position and its initial angular velocity are set. In this case, two types of collisions can occur:

- the balls are moving towards each other;
- one ball is gaining on another.

4. NUMERICAL SIMULATION

Numerical simulation of systems with instantaneous interactions, which can lead to a change in the structure of the model, has several features. These features require changes in the classical methods of integration adopted when solving systems of ordinary differential equations (for example, in the Runge-Kutta method [10]). In the system under consideration, the following features must be taken into account:

- the balls can collide during motion, which leads to an instant change in phase coordinates; in this case the time of such a collision cannot be calculated, but must be specified during the numerical simulation;
- after an elastic collision, the balls can stick together, which leads to a change in the number of phase coordinates of the system, since in fact, after sticking together, one body moves;
- also, one cannot ignore the fact that balls stuck together can separate as a result of the impact of an external driving force [12].

Numerical integration used to solve ordinary differential equations is usually performed step by step: based on the current state of the system, a new state is calculated after a certain time step (integration step) [11]. This approach assumes that the structure of the system does not change during one integration step. However, the last condition is not met when the bodies collide, and especially if this collision leads to their sticking together. Figure 3 shows an example of an incorrect phase trajectory obtained by numerically solving differential Eq. (17)–(18) using the Runge-Kutta method. At the instant of collision of bodies, their velocities were changed in accordance with Eq. (25)–(26). Since the coefficient of restitution kd in this case was chosen equal to zero, the bodies stopped after the collision, as it should be expected at a perfectly inelastic collision. At the same time, further integration led to the fact that, under the impact of the gravitational force, the balls continued to move, entering each other.

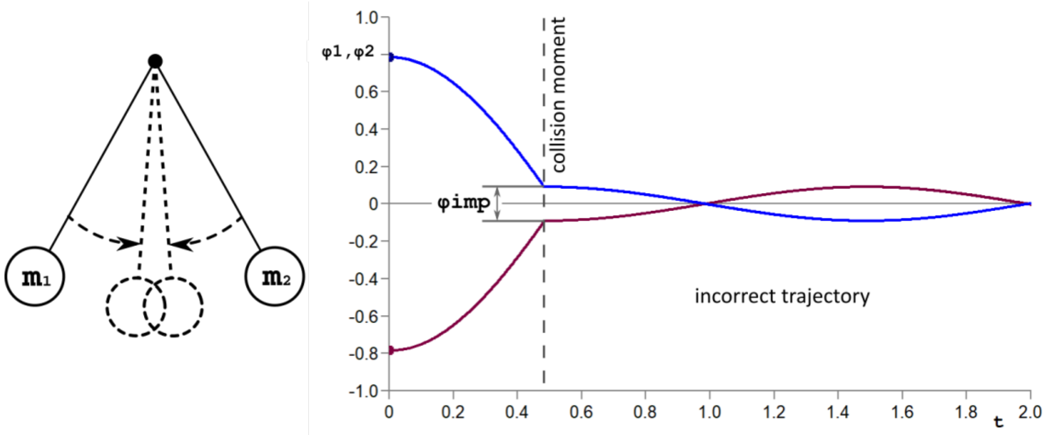

Fig. 3. Incorrect phase trajectory obtained by numerical simulation when bodies stick together after the collision. The example is calculated for: 10 = -π/4, 20 = π/4, kd = 0.

To exclude incorrect results, it is proposed to check after each integration step and, if necessary, correct the phase coordinates. In Fig. 4, a diagram of one integration step is given. The points of two phase trajectories 1(t) and 2(t) at the instant of collision and sticking of bodies are shown. Normal integration gives incorrect coordinates 1- and 2-, which need to be corrected to 1+ and 2+.

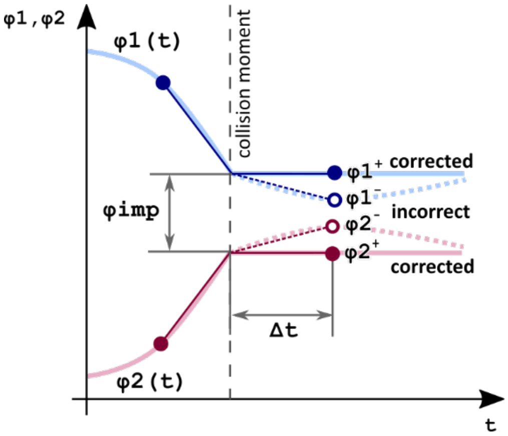

Fig. 4. Correction of a numerical integration step when bodies stick together after the collision.

To correct the phase coordinates, it is assumed that their change within the integration step is linear. This assumption does not introduce noticeable inaccuracies at a small integration step. To eliminate incorrect phase coordinates, there is a return along the phase trajectory from the incorrect point – to the instant of collision of the bodies:

1t=1--1-t
2t=2--2-t. (27)

The instant of collision of the balls is determined from the condition:

1t-2t=imp
1t-2t=impsign(1--2-), (28)

where
imp – angular distance between the centres of the balls at the instant of collision Eq. (36).

Substituting Eq. (27) with Eq. (28), we obtain the equation for calculating the instant of collision time:

1--1-Δt-2-+2-Δt=impsign(1--2-). (29)

Thus, the instant of collision Δt is equal to:

Δt=1--2--φimpsign1--2-1--2-. (30)

To correct the integration step, there is a return along the phase trajectory backward for time Δt with initial velocity - - and then forward for the same time, but already with corrected velocity +:

1+=1--1-Δt+1+Δt=1--1--1+Δt
2+=2--2-Δt+2+Δt=2--(2--2+)Δt. (31)

The velocities at the instant of collision of bodies change in accordance with:

1+=2+=m11-+m22-m1+m2. (32)

Having substituted Eq. (30) and Eq. (32) with Eq. (31), we obtain an expression for correcting the phase coordinates of the balls:

1+=1--m2m1+m21--2--impsign1--2-
2+=2-+m2m1+m21--2--impsign1--2-. (33)

Taking into account the equality of the ball masses (m1 = m2), we obtain the final expression for correcting the phase coordinates. The condition for the need for such a correction is also given, which must be checked after each integration step:

if 1--2-<imp:
1+=121-+2-+impsign1--2-
2+=121-+2--impsign1--2-
1+=2+=1-+2-2, (34)

where
imp – angular distance between the centres of the balls at the instant of collision Eq. (36);

1-, 2-,1-,2- – uncorrected phase coordinates obtained as a result of one integration step;
1+, 2+,1+,2+ – corrected phase coordinates with the account of body sticking.

An example of a phase trajectory obtained by the Runge-Kutta method with the account of the correction of phase coordinates Eq. (34) is shown in Fig. 5. In this case, because of the zero coefficient of restitution k_d, the bodies stick together after the collision, and because their initial deviations were equal in magnitude and opposite in sign, the bodies stop. Correction in this case ensures getting the correct result.

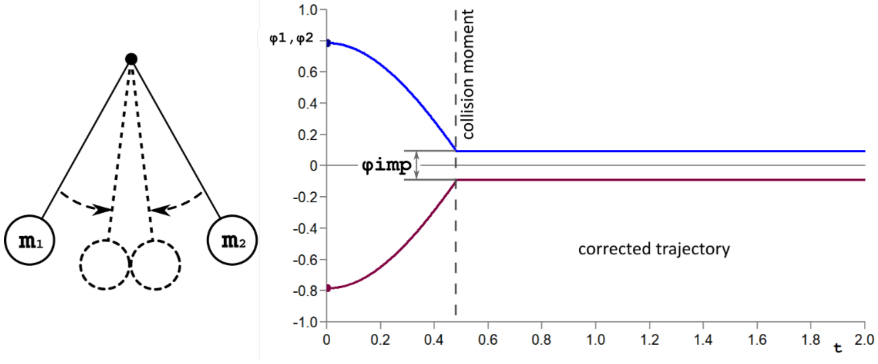

Fig. 5. Phase trajectory obtained by a numerical simulation with the correction of integration step when bodies stick together after the collision. The example is calculated for: 10 = -π/4, 20 = π/4, kd = 0.

5. RESULTS OF NUMERICAL SIMULATION FOR A PERFECTLY INELASTIC COLLISION

The central perfectly inelastic collision (the first case of motion of a system of balls) is considered at a fixed suspension point of the pendulums (differential equations (23)–(24)). To describe the condition of motion after the balls hit each other, an additional condition of a perfectly inelastic collision is used. Taking into account that the masses of the balls are equal (m1= m2 = m), the angular velocities of the balls before the collision are different and equal to 10 and 20, respectively, and after the collision their angular velocities become equal to 1=2=˙, then, according to the law of momentum conservation, we obtain the following expression for the final velocity (kd = 0):

1=2==10+202. (35)

The collision of balls occurs at the moment when the central angle between the threads to which the balls are attached becomes equal to the angle of impact imp:

imp=2-1=2·arctgrl2+2lr. (36)

The simulation of the collision process of a double pendulum was carried out with the correction of the phase coordinates Eq. (33) at the following values of the pendulum system:

l = 1.0 m – distance from the suspension point to the centre of the ball;

r = 0.1 m – radius of the ball;

g = 9.81 – acceleration of free falling.

The results of numerical simulation of a perfectly inelastic collision at various initial values of the deviation of the balls (10, 20) from the lower resting position are presented in Figs. 6–8.

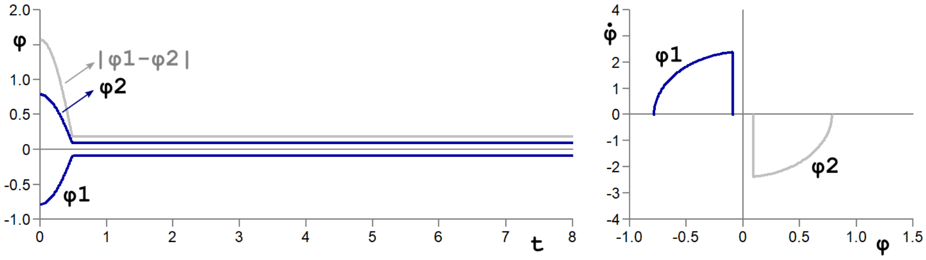

(a) (b)

Fig. 6. Free nondissipative oscillations of the pendulum with perfectly inelastic collisions (kd = 0). Time base (a) and phase portrait (b) are calculated for the following initial coordinates of the balls: 10 = – π/4, 20 = π/4.

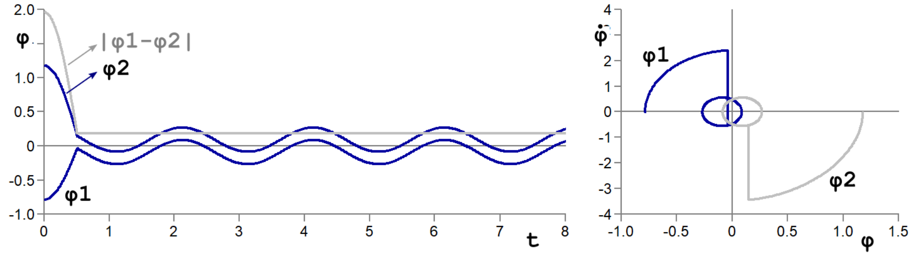

(a) (b)

Fig. 7. Free nondissipative oscillations of the pendulum with perfectly inelastic collisions (kd = 0). Time base (a) and phase portrait (b) are calculated for the following initial coordinates of the balls: 10 = – π/4, 20 = 3π/8.

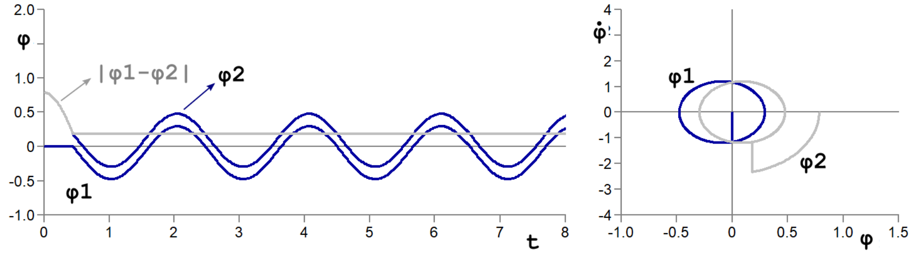

(a) (b)

Fig. 8. Free nondissipative oscillations of the pendulum with perfectly inelastic collisions (kd = 0). Time base (a) and phase portrait (b) are calculated for the following initial coordinates of the balls: 10 = 0, 20 = π/4.

From the analysis of Figs. 6–8, it follows that at the first collision, the balls stick together and further oscillations continue with the initial velocity, which is determined from Eq. (25). Thus, the initial velocity of joint oscillations at the same deviation of the balls from the equilibrium position is equal to V = 0 and oscillations after the collision do not occur (Fig. 6).

6. RESULTS OF NUMERICAL SIMULATION FOR A PERFECTLY ELASTIC COLLISION

The central perfectly elastic collision of the balls is also considered at a fixed suspension point of the pendulums (differential Eq. (23)–(24)). The numerical simulation was carried out taking into account the possible sticking of the balls Eq. (33). To describe the condition of motion after the balls hit each other, the additional condition of a perfectly elastic collision (kd = 1) is used, the angular velocities of the balls in this case are determined by the following expression:

$$1=20; \quad 2=10. \tag{37}$$

The results of the numerical simulation of a perfectly elastic collision at various initial values of the ball deviation (10, 20) from the lower resting position are shown in Figs. 9–11.

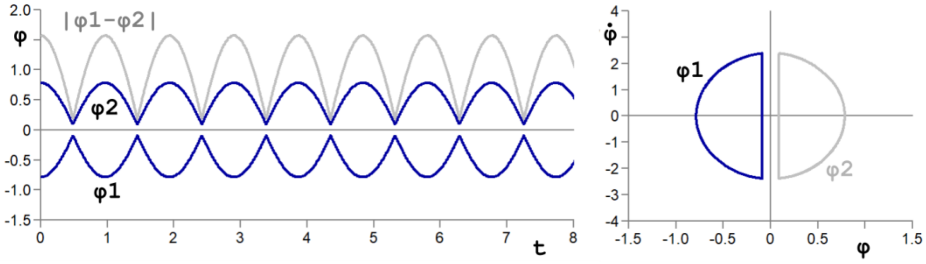

(a) (b)

Fig. 9. Free nondissipative oscillations of the pendulum with perfectly elastic collisions (kd = 1). Time base (a) and phase portrait (b) are calculated for the following initial coordinates of the balls: 10 = – π/4, 20 = π/4.

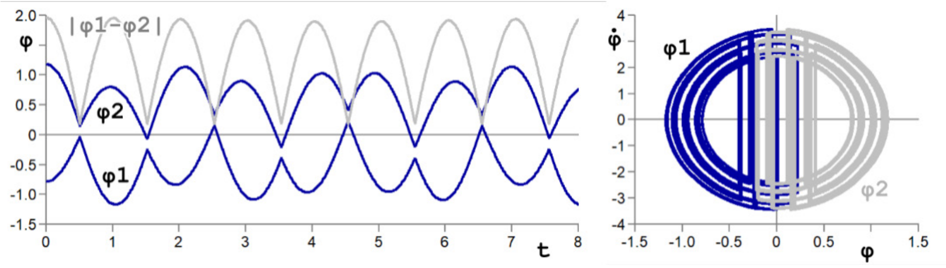

(a) (b)

Fig. 10. Free nondissipative oscillations of the pendulum with absolutely elastic impacts (kd = 1).
Time base (a) and phase portrait (tmax = 50) (b) are calculated for the following initial coordinates of the balls:
10 = – π/4, 20 = 3π/8.

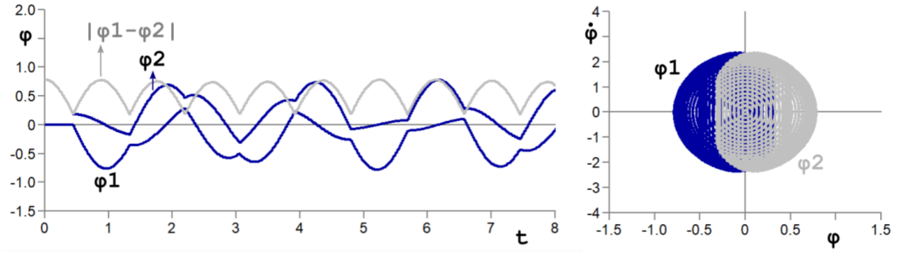

(a) (b)

Fig. 11. Free nondissipative oscillations of the pendulum with absolutely elastic impacts (kd = 1). Time base (a) and phase portrait (t_{max} = 50) (b) are calculated for the following initial coordinates of the balls: 10 = 0, 20 = π/4.

From Figs. 9–11 it follows that in the case of perfectly elastic collision and the absence of dissipation in the system, collisions between the balls continue for an infinitely long time. In the case of deviation of the balls at different angles, the oscillations are not periodic.

7. RESULTS OF NUMERICAL SIMULATION FOR A PARTIALLY ELASTIC COLLISION

The central partially elastic impact of the balls is considered at the value of the coefficient of restitution kd = 0.8 and is described by the system of differential Eq. (23)–(24). Numerical modelling was carried out taking into account the possible sticking of balls Eq. (33). To describe the condition of motion after the balls hit each other, the additional condition of partially elastic collision Eq. (25)–(26) is used.

The results of mathematical simulation of a partially elastic collision at different initial values of the deviation of the balls (10, 20) from the lower resting position are presented in Figs. 12–14.

As can be seen in Fig. 12, at the same initial deviations of the balls, their velocities during the motion are equal in magnitude, but opposite in direction. As a result of the loss of energy at the instant of collisions at the bottom point (kd < 1), the oscillations of the balls attenuate and after a while the balls stop.

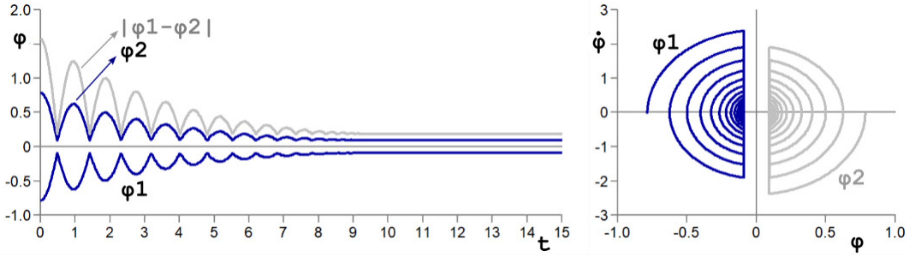

(a) (b)

Fig. 12. Free nondissipative oscillations of the pendulum with partially elastic collisions (kd = 0.8). Time base (a) and phase portrait (b) are calculated for the following initial coordinates of the balls: 10 = – π/4, 20 = π/4.

Figures 13–14 illustrate continuous oscillations resulting from unequal initial deviations of the balls. In this case, due to the loss of energy at the instant of collisions (kd < 1), after a while the balls stick together and continue oscillating as one body without collisions and without loss of energy.

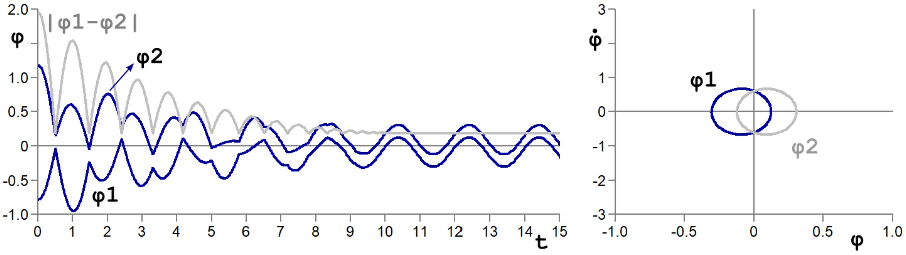

(a) (b)

Fig. 13. Free nondissipative oscillations of the pendulum with partially elastic collisions (kd = 0.8). Time base of transient process (a) and phase portrait of steady state (b) are calculated for the following initial coordinates of the balls: 10 = – π/4, 20 = 3π/8.

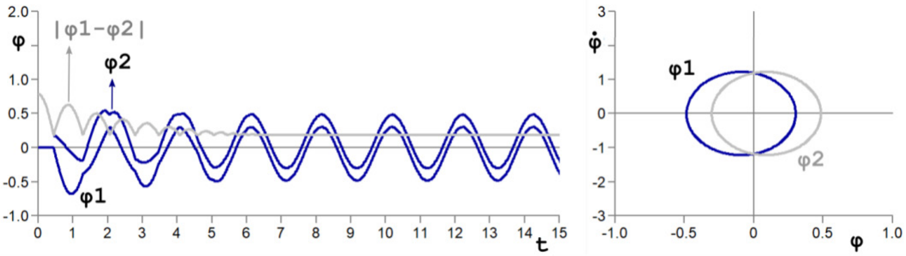

(a) (b)

Fig. 14. Free nondissipative oscillations of the pendulum with partially elastic collisions (kd = 0.8). Time base of transient process (a) and phase portrait of steady state (b) are calculated for the following initial coordinates of the balls: 10 = 0, 20 = π/4.

8. RESULTS OF NUMERICAL SIMULATION FOR A MODEL WITH ROTATING SUSPENSION POINT

The motion of pendulums at a rotating suspension point, which is described by Eq. (17)–(18), is considered for three different angular velocities of rotation of the suspension point: = 2.0 s^{-1}; = 2.8 s^{-1}, = 3.3 s^{-1}. In this case, the radius of the circle is e = 0.1 m and the coefficient of dissipation at the suspension point is b = 0.1. The perfectly elastic collision of the balls was considered, at which the coefficient of restitution was kd = 1. The numerical modelling was carried out taking into account the possible sticking of the balls Eq. (33). The results of numerical integration, presented in Figs.15–17, illustrate the steady-state (stationary) oscillations upon completion of the transient process. As follows from these figures, at a rotating suspension point of the pendulums, their stationary oscillations significantly depend on the initial conditions of motion and the rotation frequency of the suspension point.

Figure 15 shows the time base and phase portrait of stationary periodic forced oscillations with a period of rotation of the suspension point in the case of bodies sticking together. In this case, during the transient process, due to dissipation at the suspension point, the distance between the balls gradually decreases and, as a result, they stick together and continue to oscillate as one body.

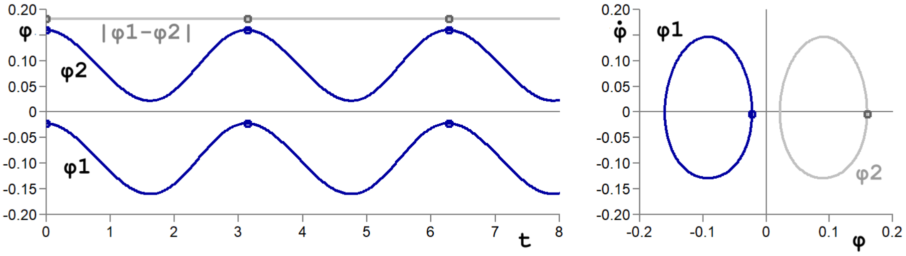

(a) (b)

Fig. 15. Forced (e = 0.1; = 2) dissipative (b = 0.1) oscillations of the pendulum with elastic collisions (kd = 1). Time base (a) and phase portrait (b) of periodic steady state with balls sticking together are calculated from the following initial coordinates: 10=-0.022231, 10=-0.003999, 20=0.159838, 20=-0.003999.

Figure 16 illustrates a stationary subharmonic mode with a period twice as long as the rotation period of the suspension point. In this example, the balls do not stick together, but perform continuous oscillations, periodically colliding with each other.

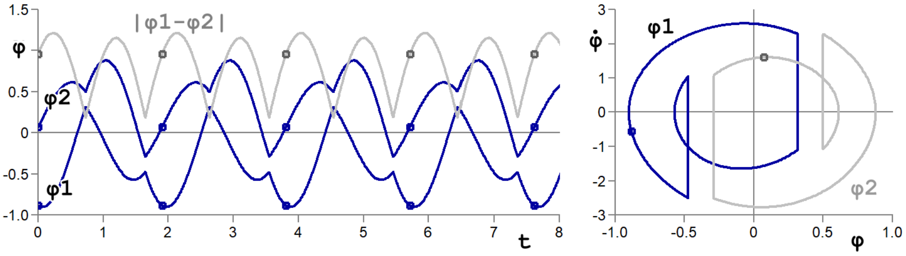

(a) (b)

Fig. 16. Forced (e = 0.1; ω = 3.3) dissipative (b = 0.1) oscillations of the pendulum with elastic collisions (kd = 1). Time base (a) and phase portrait (b) of periodic steady state with ball collisions are calculated from the following initial coordinates: 10=-0.883337, 10=-0.551977, 20=0.073256, 20=1.600822.

Figure 17 illustrates an example of a stationary aperiodic mode of the oscillation of the balls. The time base and Poincaré display points with the rotation period of the suspension point are shown. The points on the Poincaré map are not repeated, which indicates non-periodic oscillations. Similar to Fig. 16, the oscillations of the balls occur without sticking, but with periodic collisions.

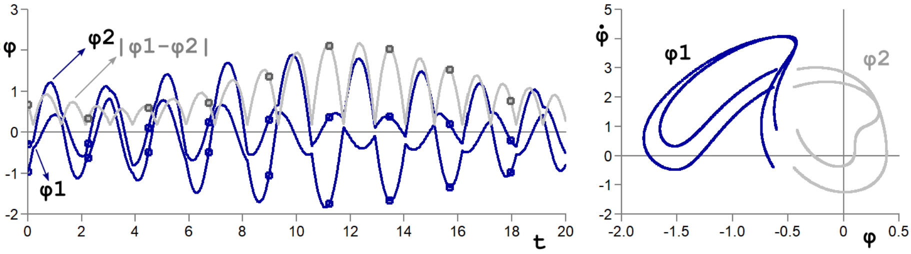

(a) (b)

Fig. 17. Forced (e = 0.1, ω = 2.8) dissipative (b = 0.1) oscillations of the pendulum with elastic collisions (kd = 1). Time base (a) and Poincare map (2000 points) (b) of aperiodic steady mode are calculated from the following initial coordinates: 10=-0.957907, 10=2.10651, 20=-0.282979, 20=0.04077.

9. CONCLUSION

The authors have obtained a system of differential equations for a pendulum system with a rotating suspension point, which allows one to proceed to a system of differential equations with an oscillating suspension point (Kapitza’s equations) and to the equations of a double pendulum with a fixed suspension point.

On the basis of the obtained system of differential equations, the problem of numerical simulation of a system with instantaneous interactions between the balls is solved. The authors have developed an approach that enables performing numerical simulation taking into account the possible sticking of balls. This will allow for further simulation of the process of collisions between the balls in an auto-balancing device during acceleration and deceleration of a rotor equipped with a ball-type auto-balancing device.

ACKNOWLEDGEMENTS

The research has been supported by the project of the Latvian Council of Science “Development of Smart Technologies for Efficient and Well-thought-out Water Operations (STEEWO)” (No. Lzp-2019 / 1-0478).

REFERENCES

1. Saveiev, I.V. (1982). *General Physics Course* (vol. I. Mechanics, Oscillations and Waves, Molecular Physics Science). Main Editorial Office of Physical and Mathematical Literature, M. (in Russian).
2. Grigoriev, A.Yu., Grigoriev, K.A., & Malyavko, D.P. (2015). *Collision of Bodies: Textbook*. SPb.: ITMO University (in Russian).
3. Strautmanis, G., Mezītis, M., Strautmane, V., & Gorbenko, A. (2018). Model of a vertical rotor with an automatic balancer with two compensating masses. In: *Vibroengineering PROCEDIA, vol. 21: 35th International Conference on Vibroengineering* (pp. 202–207), 13–15 December 2018, India, Delhi.

4. Sperling, L., Ryzhik, B., Linz, Ch., & Duckstein, H. (2002). Simulation of Two-Plane Automatic Balancing of a Rigid Rotor. *Mathematics and Computers in Simulation*, 58 (4–6), 351–365.
5. Ryzhik, B., Duckstein, H., & Sperling, L. (2004). Partial Compensation of Unbalance by One- and Two Automatic Balancing Devices. *International Journal of Rotating Machinery, 10* (3), 193–201.
6. Gorbenko, A.N., Klimenko, N.P., & Strautmanis, G. (2017). Influence of Rotor Unbalance Increasing on the Stability of its Autobalancing. *Procedia Engineering, 206*, 266–271. doi: 10.1016/j.proeng.2017.10.472.
7. Goncharov, V., Filimonikhin, G., Nevdakha, A., & Pirogov, V. (2017). An Increase of the Balancing Capacity of Ball or Roller-Type Auto-Balancers with Reduction of Time of Achieving Auto-Balancing. *Eastern-European Journal of Enterprise Technologies, 1* (7), 15–24. doi: 10.15587/1729-4061.2017.92834.
8. Kapitza, P.L. (1951). Dynamic stability of the pendulum at an oscillating suspension point. *ZhETF, 21*, 588–597 (in Russian).
9. Butikov, E.I. (2011). An Improved Criterion for Kapitza's Pendulum Stability. *Journal of Physics A: Mathematical and Theoretical, 44*, 295202.
10. Butcher, J.C. (2008). *Numerical Methods for Ordinary Differential Equations*. John Willey & Sons.
11. Urbahs, A., Banovs, M., Carjova, K., Turko, V., & Feshchuk, J. (2017). Research of the Micromechanics of Composite Materials with Polymer Matrix Failure under Static Loading Using the Acoustic Emission Method. *Aviation, 21* (1), 9–16.
12. Urbahs, A., & Carjova, K. (2019). Bolting Elements of Helicopter Fuselage and Tail Boom Joints Using Acoustic Emission Amplitude and Absolute Energy Criterion. *Journal of Aerospace Engineering, 32* (3), 3–12.
13. Urbahs, A., Carjova, K., & Fescuks, J. (2017). Analysis of the Results of Acoustic Emission Diagnostics of a Structure during Helicopter Fatigue Tests. *Aviation, 21* (2), 64–69.

LATVIAN JOURNAL OF PHYSICS
AND TECHNICAL SCIENCES
2022, N 3

DOI: 10.2478/lpts-2022-0017

SPECIFICS OF POWER LOSSES IN POWER LINES INCLUDING PARALLEL LINES

J. Survilo

Riga Technical University, Power Engineering Institute
12 Azenes Str., Riga, LV-1048, LATVIA
E-mail: josifs.survilo@rtu.lv

Reducing power losses is invested in the trend of combating climate warming. It is necessary to know what parameters of power transmission lines affect the losses in them. In short and medium lines with accounted lumped parameters, the role and influence of the line parameters on losses are visible. In the lines with distributed parameters, at least with one series parameter and one parallel parameter, the role played by them, computing losses in ordinary way as difference between power at line sending and receiving end, is hidden. This is pronounced when considering parallel lines. In two parallel lines the losses can be greater than in a single line. This may occur when the current at the end of the lines is less than the boundary value: the value when two parallel lines and a single line have the same losses. The longer the line and the higher the rated voltage, the stronger the effect. In view of this aspect, it is necessary to know the boundary current. This current can be determined in ordinary way by a series of calculations changing the load value. In some cases, boundary current is affected not only by modulus of the current at the end of the line but also by its angle. It is better to calculate the boundary current by a formula, while studying the role of each parameter.

Keywords*: Distributed parameters, long lines, losses of power lines, medium lines, parallel power lines.*

1. INTRODUCTION

Today, all the possibilities are relevant, which do not worsen the thermal balance of the globe. Even a small reduction in energy loss is worth considering. Attention paid to losses in power systems is huge [1]–[5].

Climate warming is hampered by the use of renewable energy sources. This requires developed networks and modern power lines. Although high temperature conductors increase losses, they promote the use of renewable energy sources, thereby reducing greenhouse gas emissions [6], [7].

This article focuses on losses. The sophisticated approach to the design and operation of power transmission lines [8] contributes to their more rational use and reduction of losses in the face of increasing use of renewable energy sources. With modern calculating technology, the calculation of losses in the power transmission line is not onerous. You just need to subtract the power at the end of a line from the power at the beginning of the line. The power losses are affected by the parameters of the power line as well. The role of these parameters, with such a calculation, is hardly visible and may be unexpected. The alternative determination (ad) of losses makes it possible to more clearly see this influence. Therefore, it is possible to find the reason for the deviation of losses from the expected, more reasonable and quick to select the design and parameters of the line. Thanks to the advances in semiconductor technology, flexible ac transmission system finds application in the electric power industry [9], [10]. It is desirable to configure line performance influencing its parameters as needed that is easier to do if you know their impact.

An AD approach is useful not only for power losses. It can also be used to calculate voltage losses [11] for the same purpose, to more clearly reveal the influence of line parameters.

Talking about power losses, the AD is useful considering the losses in parallel lines.

Parallel transmission lines are widely used in the electric power industry [12]. This allows, firstly, increasing the reliability of power supply [13], facilitating the scheduling of repairs, as well as increasing the power transmission capacity. This is important when transferring the energy from one power system to another [14]. At the same time, when the wires of both lines are suspended on the same supports, the right of way does not increase [15]. Then we have double-circuit lines (DCL) [16], [17] where a total transposition is made, to eliminate the influence of one line on the other [15], [18].

Thus, energy transfer along two parallel lines (TPL) is used quite often.

When one of the TPL for some reason remains in operation, the active losses on the route change. Whether the second line should be switched on afterwards or not, can also be considered from the point of view of active losses.

Here a criterion is the boundary current (BC): if currently the load current is more than BC, the disconnected line must be switched on. This is because the losses in TPL are less when the current at the end of the lines (further – load current (LC)) is more than BC and vice versa.

The issue of losses in parallel lines with distributed parameters is not specifically considered. For instance, in [4], [19]–[21] the losses are studied but not in parallel lines. The Depazo formula is given in [22] but this expression cannot be used to decide whether two or one line should be in operation.

As said above, for a given load, line loss, be it single line or parallel lines, is defined self-explanatory, as the difference in power at the transmitting end of the line and at the receiving end. A series of calculations on the set of currents at the end of the lines is required, to determine the BC. For identical parallel lines (that have the same specific parameters (r_0, x_0, g_0, b_0) and length l), it is necessary to vary only the absolute value of the load current (LC). However, sometimes parallel lines can be removed from one another, and in addition have different lengths and parameters [18], in short, they are non-identical. Then it is necessary to determine BC changing the modulus of LC at a specified angle φ. With the modern development of digital technology, this also is not a serious obstacle. But finding the BC analytically is in itself attractive and, moreover, the role of each line parameter can be estimated. In addition, solving the problem for non-identical lines allows you to solve the problem in a routine way, when the number of parallel lines is more than two. The final expression of BC for identical lines is simple and easy to calculate, but for non-identical lines it is complicated and rather tortuous to find. To derive this expression, it is necessary to intricate AD of power loss in long lines. The expression for BC of identical lines is found as a special case.

Four specific distributed parameters describe the power line: resistance r_0, reactance x_0, conductance g_0 and susceptance b_0. Whether distributed or lumped parameters are used in the calculations or altogether are taken into account depends on the length of the line and its rated voltage. The shorter the line and (or) lower the rated voltage, the fewer parameters are considered distributed or taken into account at all.

Low voltage lines are considered as short (<80 km) where parallel parameters – conductance and susceptance – are skipped (considered equal to zero); these lines are characterised by two series parameters – resistance and reactance; such lines can be considered as two parameter lines. In medium voltage line conductance is considered to be zero; only three parameters are taken into account. The parameters of low voltage short (<80 km) and medium voltage (80 – 250 km) lines [3] are considered as lumped in order to simplify calculations, although in the three parameter lines they can be used as distributed depending on the required accuracy of calculations especially in cases where the line length is respectful. Cable lines do not fit this gradation. In long lines, all four parameters are taken into account such as they are in every line by nature, i.e. as distributed. Component lines (CL) of a TPL (especially of DCL) for the most part are identical.

When the lines CLa and CLb are identical, the BC ($\dot{I}_A$ or $\dot{I}_B$) is the same, no matter which of the two lines is disconnected. When the lines CLa and CLb are non-identical, the BC $\dot{I}_A$ when CLb could be disconnected is different from BC $\dot{I}_B$ when CLa could be disconnected.

The BC can be determined if at least one series parameter (r_0 or x_0) and one parallel parameter (g_0 or b_0) is taken into account.

In the paper, all electrical quantities are considered for one phase: phase current, phase voltage, power and losses for one phase.

All complex quantities are indicated by dot above (e.g., $\dot{H}$), absolute value (modulus) is without dot (H), the real value is indicated by subscript r (H_r), and the imaginary value – by subscript i (H_i).

All units are in SI system: m, A, V, W, VA, Var, Ω, Ω/m, S, S/m unless otherwise stated or for euphony.

2. DETERMINATION OF POWER LOSSES IN POWER LINES WITH LUMPED PARAMETERS

This consideration was made a long time ago. For example, it is described in [23]. Here a line is considered that has not only specific susceptance b_0 but also conductance g_0. With lumped parameters, only short and medium lines are considered, in which conductance is not taken into account [21].

Thus, a simpler T-shaped equivalent circuit is proposed for consideration, which provides a clearer representation of the capacitive currents. To write a simple expression for power loss in such lines, it is assumed that the voltages at the beginning and the end of the line are the same. If such an assumption is unacceptable and an exact solution to the issue is necessary, then digital technology allows solving this issue for medium lines as for long ones, especially since the method with different voltages but with lumped parameters also does not provide an exact solution.

In a line (Fig. 1) LC flows from left to right. The current of lumped capacity in the left half of the line flows from left to right and in the right half – from right to left. Both currents flow to the lumped capacity at the middle of the line.

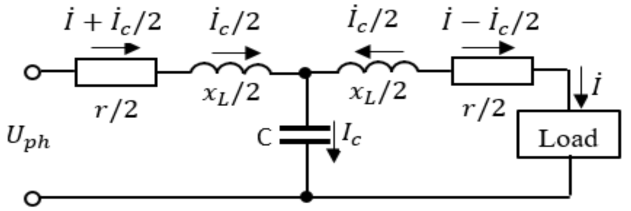

Fig. 1. Lumped power line equivalent circuit (one phase)

Therefore, active losses ΔP in resistance of the line can be obtained by simple determination (SD) as below:

$$\Delta P = \left(\frac{r}{2}\right)\{[I_r^2 + \left(I_i + \frac{I_c}{2}\right)^2] + [I_r^2 + \left(I_i - \frac{I_c}{2}\right)^2]\} = (r/2)[2(I_r^2 + I_i^2) + I_c^2/2] = r(I^2 + I_c^2/4). \quad (1)$$

The expression is simple, later it will be determined how accurate the results it gives.

Short parallel lines always have less power loss than a single line at any load and line length.

For medium voltage lines, this cannot be so categorically asserted. Therefore, for them you need to try to find BC. For identical TPL, as mostly is the case in medium parallel lines, this phase current can be estimated using the diagram in Fig. 1 (where only one CL is depicted).

For identical lines, the current is distributed equally and common active loss is

$$\Delta P_A = 2\left(\frac{r}{2}\right)\{\left[\left(\frac{I_r}{2}\right)^2 + \left(\frac{I_i}{2} - \frac{I_c}{2}\right)^2\right] + \left[\left(\frac{I_r}{2}\right)^2 + \left(\frac{I_i}{2} + \frac{I_c}{2}\right)^2\right] = r\left(\frac{I^2}{2} + \frac{I_c^2}{2}\right). \quad (2)$$

Equating both expressions, we find BC by (SD):

$$I_A = I_c/\sqrt{2}\ . \tag{3}$$

When the modulus I of the LC $\dot{I}$ (irrespective of cosφ) is less than the current $\dot{I}_A$, a single line in operation will have advantage because an active loss now is less than in two such lines connected in parallel.

The higher the capacitive current $\dot{I}_C$, the stronger attention should be paid to the issue.

3. THE CASE OF LONG LINES

Consideration of long lines begins according to the diagram in Fig. 2. The desired quantities of a line ($\dot{U}_1$, $\dot{I}_1$ ...) at the beginning of line rote (left) are indicated. The given values of the quantities at the end of the line ($\dot{U}$, $\dot{I}$ ...) are indicated on the right.

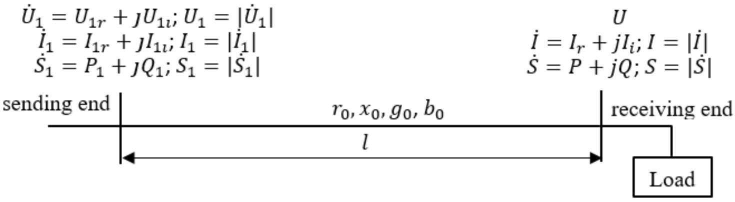

Fig. 2. Power line and significant quantities.
All quantities are for one phase.

For consideration, we need the following relations, some of them are known [24]; others are taken from [11] and some others – shown in Fig. 2:

$$\begin{gathered}\dot{z}_0 = r_0 + jx_0\ ;\dot{y}_0 = g_0 + jb_0; \dot{z} = \dot{z}_0 l; \dot{y} = \dot{y}_0 l; \dot{Z}_\lambda = \sqrt{\dot{z}_0/\dot{y}_0} = Z_{\lambda r} + jZ_{\lambda i};\\ Z_\lambda = |\dot{Z}_\lambda|;\ \dot{\gamma} = \sqrt{\dot{z}\dot{y}} = \alpha + j\beta; \dot{U}_\lambda = \dot{I}\dot{Z}_\lambda{=}U_{\lambda r} + jU_{\lambda i}; U_\lambda = |\dot{U}_\lambda|; \dot{I}_\lambda = \frac{U}{\dot{Z}_\lambda} = I_{\lambda r} + jI_{\lambda i};\\ I_\lambda = |\dot{I}_\lambda|;\ U_1 = \dot{A}U + \dot{B}\dot{I};\ \dot{I}_1 = \dot{C}\,\dot{U} + \dot{D}\,\dot{I};\ \dot{S} = U\hat{I}; \dot{S}_1 = \dot{U}_1\hat{I}_1; \Delta\dot{S} = \dot{S}_1 - \dot{S};\\ \dot{A} = \mathrm{ch}\,(\dot{\gamma}); \dot{B} = \dot{Z}_\lambda \mathrm{sh}\,(\dot{\gamma}); \dot{C} = \mathrm{sh}(\dot{\gamma})\,/\dot{Z}_\lambda; \dot{D} = \dot{A}.\end{gathered} \tag{4}$$

As previously stated, relations (4) make sense only if $\dot{z}_0$ and $\dot{y}_0$ are not equal to zero. This can only be possible if the power transmission line is characterised at least by one serial parameter (r_0, x_0) and one parallel parameter (g_0, b_0).

Further, you should pay attention to avoid mistakes by confusing the vector of a quantity (e.g., $\dot{H}$) with modulus H of this quantity.

Based on formula (20) in [11], active loss in line consists of five terms:

$$\Delta P = c_1 + c_2 + c_{III} + c_{IV} + C_V, \tag{5}$$

where each term is

$$\begin{gathered}c_1 = Z_{\lambda r} sh(2\alpha)(I_\lambda^2 + I^2)/2; \quad c_2 = Z_{\lambda i}\, sin\,(2\beta)(I_\lambda^2 - I^2)/2;\\ c_{III} = [sh^2(\alpha) - sin^2(\beta)]P;\ c_{IV} = (Z_{\lambda r}^2 - Z_{\lambda i}^2)[sh^2(\alpha) + sin^2(\beta)]P/Z_\lambda^2;\end{gathered} \tag{6}$$

$$c_V = 2Z_{\lambda r}Z_{\lambda i}[sh^2(\alpha) + sin^2(\beta)]Q/Z_\lambda^2. \quad (7)$$

If we replace P with UsI in c_{III} and in C_{IV} and replace Q with $U\sqrt{1-s^2}$ (-w)I in c_V then for load at the end of the lines with characteristics s and w (see below) we get:

$$\begin{aligned} &c_{III} = [sh^2(\alpha) - sin^2(\beta)]UsI;\ c_{IV} = (Z_{\lambda r}^2 - Z_{\lambda i}^2)[sh^2(\alpha) + sin^2(\beta)]UsI/Z_\lambda^2; \\ &c_V = 2Z_{\lambda r}Z_{\lambda i}[sh^2(\alpha) + sin^2(\beta)]U\sqrt{1-s^2}\,(-\mathrm{w})I/Z_\lambda^2; \end{aligned} \quad (8)$$

$$s = \cos(\varphi),\ w = sign(I_i), \quad (9)$$

where φ is a power factor of the LC (at the right in Fig. 2), I_i – imaginable (reactive) LC.

We combine C_{III} with C_{IV} and denote the sum by c_3, denote term c_V by c_4, then we get

$$\begin{aligned} &c_3 = c_{III} + c_{IV} = \{[sh^2(\alpha) - sin^2(\beta)] + (Z_{\lambda r}^2 - Z_{\lambda i}^2)[sh^2(\alpha) + sin^2(\beta)]/Z_\lambda^2\}UsI \\ &c_4 = 2Z_{\lambda r}Z_{\lambda i}[sh^2(\alpha) + sin^2(\beta)]U\sqrt{1-s^2}\,(-w)I/Z_\lambda^2. \end{aligned} \quad (10)$$

Separating coefficients a from c_1 ... c_4 so that they do not contain I_λ, I, we get a_1 ... a_4 for LC characterised by s and w:

$$\begin{aligned} &a_1 = Z_{\lambda r}sh(2\alpha)/2;\ a_2 = Z_{\lambda i}\sin(2\beta)/2; \\ &a_3 = \{[sh^2(\alpha) - sin^2(\beta)] + (Z_{\lambda r}^2 - Z_{\lambda i}^2)[sh^2(\alpha) + sin^2(\beta)]/\,Z_\lambda^2\}Us; \\ &a_4 = 2Z_{\lambda r}Z_{\lambda i}[sh^2(\alpha) + sin^2(\beta)]U\sqrt{1-s^2}\,(-w)/Z_\lambda^2. \end{aligned} \quad (11)$$

Now active losses can be determined by intricate (observing (5)–(11)) expressions (ID):

$$\Delta P = c_1 + c_2 + c_3 + c_4 = a_1\left(I_\lambda^2 + I^2\right) + a_2(I_\lambda^2 - I^2) + a_3I + a_4I. \quad (12)$$

Separating in (12) I_λ^2 and I^2 we rewrite it:

$$\Delta P = a'I^2 + b'I + c';\ a' = a_1 - a_2;\ b' = a_3 + a_4;\ c' = h'I_\lambda^2;\ h' = a_1 + a_2. \quad (13)$$

Thus, in an AD of power loss in long line, the power loss is defined by: 1) the square of LC modulus, 2) the first degree of the modulus, taking into account the angle φ (hidden in the coefficient b') between the current and voltage and 3) the term defined only by the parameters of the line; in other words, in long line, the power loss is a trinomial [25] of LC modulus with a specific angle φ of LC.

From expression (13), we see that a constant term that does not depend on LC participates in the loss of power, which makes feel itself more at low LCs. To decrease the current $\dot{I}_\lambda$, it is necessary to increase $\dot{Z}_\lambda$ (see (4)), i.e. increase $\dot{z}_0$ or decrease $\dot{y}_0$ (their imaginary components) taking into account dependence of h' on $\dot{z}_0$ and $\dot{y}_0$.

If the line is designed to transmit high power, then the first term plays the main role in the losses where the hyperbolic sine plays the predominant role and it is proportional here to phase resistance r_0 (see (34) later) but $\dot{Z}_\lambda$ changes little with r. The second term has its share as well, where square of hyperbolic sine and sine are decisive.

Other influences can be analysed in the same way. Similarly, an expression for reactive power loss can be derived. The influence of parameters on voltage loss can be analysed based on (13) in [11].

Parallel lines are considered based on Fig. 3. All expressions (4)–(13) are valid for component lines CLa or CLb by adding to the subscript of a quantity letter a or b. The quantities of TPL working together contain letter p in subscript.

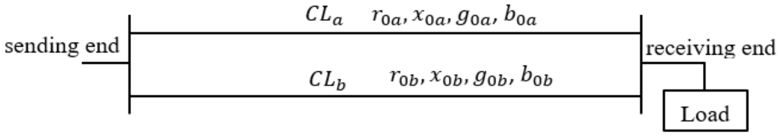

Fig. 3. Two parallel lines, any of them can be switched off.

We shall look for such an LC, for example, I_A, at which the loss ΔP_{Aa} of CLa single in operation is equal to the loss ΔP_{Ap} of TPL, CLa and CLb:

$$\Delta P_{Aa} = \Delta P_{Ap} \tag{14}$$

or, in a more general case, equal to the share k_A of loss ΔP_{Ap}:

$$\Delta P_{Aa} = k_A \Delta P_{Ap}. \tag{15}$$

Losses ΔP_{Aa} and ΔP_{Ap} are for LC, characterised by s and w (see (9)), and defined based on expression (13):

$$\Delta P_{Aa} = a'_a I_A^2 + b'_a I_A + c'_a; \tag{16}$$

$$\Delta P_{Ap} = a'_p I_A^2 + b'_p I_A + c'_p. \tag{17}$$

Based on expressions (15)–(17), a quadratic equation can be drawn up:

$$\left(a'_a - a'_p k_A\right) I_A^2 + \left(b'_a - b'_p k_A\right) I_A + \left(c'_a - c'_p k_A\right) = 0. \tag{18}$$

Denoting below, we obtain current I_A:

$$A_A = a'_a - a'_p k_A;\ B_A = b'_a - b'_p k_A;\ C_A = c'_a - c'_p k_A; \tag{19}$$

$$I_A = \left(-B_A + \sqrt{B_A^2 - 4A_A C_A}\right)/(2A_A). \tag{20}$$

Without going into deep substantiation, the plus sign in front of the square root can be explained as follows. The coefficient A_A is always positive, since the square of the load current in two parallel lines will always provide less losses than the square of the same current in one line. The coefficient C_A is always negative, since the no-load losses in two lines are always greater than in one. Thus, $|\sqrt{B_A^2 - 4A_AC_A}\ |>|-B_A|$. In the vicinity of $k_A = 1$ the current is positive, a plus sign is needed in front of the square root.

If the lines CLa and CLb are non-identical and the line CLb is left in the work, then the indices a and A are replaced by b and B to denote corresponding quantities for CLb.

To use formula (20), you need to know the coefficients a'_a, b'_a, c'_a, the current $I_{\lambda a}$ and a'_p, b'_p, c'_p, $I_{\lambda p}$. The necessary quantities for CLa and CLb can be found observing (4), (11) and (13); the quantities $\dot{A}_p$, $\dot{B}_p$, $\dot{C}_p$, $\dot{Z}_{\lambda p}$ for TPL – out of those of CLa and CLb (see Section V in [11]). After that coefficients a_{1p} ... a_{4p} can be determined using the following equalities [26]:

$$\begin{aligned} \dot{e} &= sh(\dot{\gamma}_p) = sh(\alpha_p + j\beta_p) = \cos(\beta_p)\, sh(\alpha_p) + jsin(\beta_p)ch(\alpha_p); \\ \dot{f} &= ch(\dot{\gamma}_p) = ch(\alpha_p + j\beta_p) = \cos(\beta_p)\, ch(\alpha_p) + jsin(\beta_p)sh(\alpha_p). \end{aligned} \tag{21}$$

Hyperbolic tangent of argument α_p, tangent of argument β_p and arguments themselves are:

$$\mathrm{th}(\alpha_p) = real(\dot{e})/real(\dot{f});\ \ tang(\beta_p) = imag(\dot{e})/real(\dot{f}); \tag{22}$$

$$\alpha_p = arcth(\alpha_p);\ \beta_p = arctang(\beta_p). \tag{23}$$

The coefficients a_{1p} ... a_{4p} for arguments α_p and β_p are determined on the base of (11).

After determination of BC, we can find out how much the loss in the single CLa (or CLb) differs from the loss in the TPL for a given LC $\dot{I}_d$. If you are willing to know how only the absolute value I_d of current $\dot{I}_d$ is affected, then in (16), (17) the modulus of current I_d must be inserted instead of the BC I_A. Such a case may arise, when you want to find discrepancy $\varDelta\varPi_d$ which is the difference of losses of TPL and of single CLa at current $I_{Ad} \neq I_A$; $\varDelta\varPi_d$ for BC I_A can be designated $\varDelta\varPi_{Al}$ if $I_{Ad} < I_A$ and $\varDelta\varPi_{Am}$ if $I_{Ad} > I_A$:

$$\varDelta\varPi_{Al} = \varDelta P_{Apl} - \varDelta P_{Aal};\ \varDelta\varPi_{Am} = \varDelta P_{Aam} - \varDelta P_{Apm}, \tag{24}$$

where $\varDelta P_l$ is by (16), (17) at the current $I_{Ad} = I_{Al} = q_l I_A$, $q_l < 1$; $\varDelta P_m$ – at the current $I_{Ad} = I_{Am} = q_m I_A$, $q_m > 1$. At boundary current I_A=I_{Aa}, discrepancy is zero and $q = q_l = q_m = 1$.

If the losses for the vector $\dot{I}_d$ of a given LC are of interest, such coefficients a_{3ad}, a_{4ad} and module I_d should be used instead of a_{3a}, a_{4a} in expression (11) for current $\dot{I}_d$ characterised by s_d and w_d:

$$a_{3ad} = \{[sh^2(\alpha_a) - sin^2(\beta_a)]+ (Z^2_{\lambda ra} - Z^2_{\lambda ia})[sh^2(\alpha_a) + sin^2(\beta_a)]/ Z^2_{\lambda a}\}Us_d;$$
$$a_{4ad} = 2Z_{\lambda ra}Z_{\lambda ia}[sh^2(\alpha_a) + sin^2(\beta_a)]U\sqrt{1 - s_d^2}\,(-w_d)/Z^2_{\lambda a} \qquad (25)$$

or

$$a_{3ad} = a_{3a}s_d/s;\ a_{4ad} = a_{4a}\sqrt{1 - s_d^2}\,(-w_d)/\sqrt{1 - s^2}\,(-w), \qquad (26)$$

where s_d and w_d by (9) for the given current $\dot I_d$.

4. THE CASE OF TWO IDENTICAL LONG LINES

To derive the BC formula, it is necessary to represent first two terms in (6) in a different form:

$$c_{1a}=c_{10a} + a_{1a}I^2;\ c_{2a}=c_{20a} - a_{2a}I^2; \qquad (27)$$

$$c_{10a} = a_{1a}I^2_{\lambda a};\ c_{20a} = a_{2a}I^2_{\lambda a}. \qquad (28)$$

Then formula (12) for the BC I_A or (I_B) in a single CLa (or CLb) takes the form:

$$\Delta P_{Aa} = c_{10a} + a_{1a}I_A^2 + c_{20a} - a_{2a}I_A^2 + a_{3a}I + a_{4a}I. \qquad (29)$$

For identical CLa and CLb the loss will be

$$\Delta P_A = 2[c_{10a} + a_{1a}(\tfrac{I_A}{2})^2 + c_{20a} - a_{2a}(\tfrac{I_A}{2})^2 + a_{3a}I/2 + a_{4a}I/2]. \qquad (30)$$

Equating the losses ΔP_{Aa} and ΔP_A we get:

$$a_{1a}I_A^2 - a_{2a}I_A^2=2(c_{10a} + c_{20a}) \qquad (31)$$

and with (28) in mind, BC is determined by short expression

$$I_A=\sqrt{2}I_{\lambda a}\sqrt{(a_{1a} + a_{2a})/(a_{1a} - a_{2a})}. \qquad (32)$$

With identical lines, BCs are equal, $I_A = I_B$, and are the same regardless of s and w, i.e. TPL have a single value of BC depending only on the parameters of the lines.

When calculating losses by (16), (17), it should be remembered that

$$I_{\lambda p} = 2I_{\lambda a};\ a_{1p} = a_{1a}/2;\ a_{2p} = a_{2a}/2;\ a_{3p} = a_{3a};\ a_{4p} = a_{4a}. \qquad (33)$$

This is derived assuming that for identical lines $\dot z_{0p} = \dot z_{0a}/2$, $\dot y_{0p} = 2\dot y_{0a}$. Further observing (4): $\dot Z_{\lambda p} = \dot Z_{\lambda a}/2$, $\dot\gamma_p = \dot\gamma_a$. Hence (see (11)), owing to $\dot z_{\lambda pr}$ and $\dot z_{\lambda pi}$, a_{1p} and a_{2p} decrease but a_{1p} and a_{2p} do not change because the influence of $\dot z_{\lambda pr}$ and $\dot z_{\lambda pi}$ is compensated by $Z^2_{\lambda p}$.

5. THE VALUES IN REALITY

Calculations are made for one phase.

A. 110 kV lines

Let us consider what the values can be in the medium voltage line. We take two identical 110e3 V line l=100e3 m long with phase voltage $= 110e3/\sqrt{3}$. With wire AC120/27 [23] specific phase parameters are: resistance r_0 =2.53e-4 Ω, reactance x_0 =4e-4 Ω, conductance g_0=0 S, susceptance b_0=2.7e-9 S.

SD is employed according to (1)–(3). For the entire line: phase conductor resistance $r = r_0 l = 25.3$; $x = 40$; phase susceptance b of the line is b=$b_0 l$=2.7e-9·100e3= =270e-6. Capacitive phase current is $I_c = bU_{ph}$=270e-6·110e3/$\sqrt{3}$=17.1474 A . BC by (3) is $I_A = I_c/\sqrt{2}$ =12.125. Line active loss by (1) is $\Delta P_{Aa} = 25.3(12.125^2+$ $+17.1474^2/4)$=5.5793e3; active loss ΔP_A of TPL for I_A according to (2) has the same value.

Let us calculate this loss by AD (16), (17) for the same current 12.125 A. We obtain ΔP_{Aa}=6.186e3; ΔP_A=6.8077e3e3.

We see two deviations from the values of SD by (1) and (2): they are not equal to each other and to those of SD. This is because by AD (20) the BC differs from that calculated by SD (2). The BC by (20) is $I_A = I_B$=14.0108 and (29): (30) $\Delta\dot{P}_{Aa} = \Delta\dot{P}_{Bb}$=7.4298e3; $\Delta P_A = \Delta P_B$ have the same value. For current 12.25, ΔP_{Aa} by SD divided by ΔP_{Aa} by AD is 5.5793e3/6.8077e3=0.82; for current I_C = 17.1474, the ratio is 0.94; for $2I_C$ – 0.98.

Usually in practice LC is higher, and the accuracy of active loss calculation by SD is sufficient. Ratio of BCs is 12.125/14.0108=0.874.

B. 330 kV lines

I. Calculations of five sets of line parameters are made with the main purpose of determining their influence on losses in the line (Table 1). Losses $\Delta\dot{S}$ were calculated in ordinary way by formula (4) and to check the correctness of AD of the active losses – also by formula (13). The influence of specific parameter digressions is made by comparison with the basic case. The role of the parameters is visible if we take into account their ratios at their practical values in the electric power systems. In this case based on (25) – (28) in [11], we have the following approximate relations:

$$\begin{gathered}\psi \approx -r_0/x_0;\, \gamma_0 \approx \beta_0 \approx \sqrt{b_0 x_0}\,;\, \alpha_0 \approx \beta_0\psi/2 \approx r_0\sqrt{\frac{b_0}{x_0}}/2; \\ Z_\lambda \approx \sqrt{x_0/b_0}\,;\; U_\lambda = I\sqrt{x_0/b_0}\,;\, I_\lambda = U\sqrt{b_0/x_0}\,.\end{gathered} \tag{34}$$

A decrease in susceptance b_0 was expected to result in greater diminishing in losses in the absence of load current (at I=0) because I_λ decreased. This did not happen due to the coefficients a_1, a_2 (see (11)) and their dependence on b_0 through β_0 and α_0.

We see observing (34) that β_0, α_0 and I_λ diminish proportionally to $\sqrt{b_0}$. Effect of I_λ is reduced by increasing effect of h' (see (13)).

The greatest influence on losses is exerted by the resistance r_0, since fading decrement α is proportional to r_0 but a_1, a_3, a_4 are proportional to $sh(2\alpha)$, $sh(\alpha)$ which are proportional to small values of α. At no load, r_0 decrease loses its power.

Table 1. Impact of Line Parameters of Specific Quantities

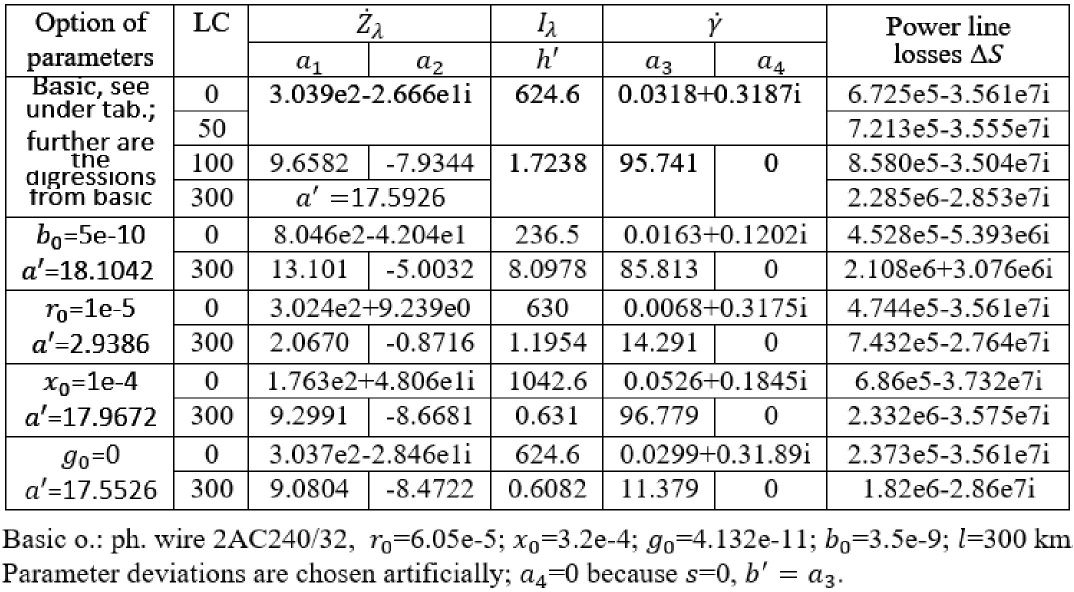

Option of parameters	LC	$\dot{Z}_\lambda$		I_λ	$\dot{\gamma}$		Power line losses ΔS
		a_1	a_2	h'	a_3	a_4	
Basic, see under tab.; further are the digressions from basic	0	3.039e2-2.666e1i		624.6	0.0318+0.3187i		6.725e5-3.561e7i
	50						7.213e5-3.555e7i
	100	9.6582	-7.9344	1.7238	95.741	0	8.580e5-3.504e7i
	300	a' =17.5926					2.285e6-2.853e7i
b_0=5e-10 a'=18.1042	0	8.046e2-4.204e1		236.5	0.0163+0.1202i		4.528e5-5.393e6i
	300	13.101	-5.0032	8.0978	85.813	0	2.108e6+3.076e6i
r_0=1e-5 a'=2.9386	0	3.024e2+9.239e0		630	0.0068+0.3175i		4.744e5-3.561e7i
	300	2.0670	-0.8716	1.1954	14.291	0	7.432e5-2.764e7i
x_0=1e-4 a'=17.9672	0	1.763e2+4.806e1i		1042.6	0.0526+0.1845i		6.86e5-3.732e7i
	300	9.2991	-8.6681	0.631	96.779	0	2.332e6-3.575e7i
g_0=0 a'=17.5526	0	3.037e2-2.846e1i		624.6	0.0299+0.31.89i		2.373e5-3.561e7i
	300	9.0804	-8.4722	0.6082	11.379	0	1.82e6-2.86e7i

Basic o.: ph. wire 2AC240/32, r_0=6.05e-5; x_0=3.2e-4; g_0=4.132e-11; b_0=3.5e-9; l=300 km
Parameter deviations are chosen artificially; a_4=0 because s=0, $b' = a_3$.

A decrease in reactance x_0 leads to a decrease of Z_λ and to an increase of I_λ; a_1, a_2 change little, therefore, ΔP at I=0 little changes. For the same reason ΔP at I=300 hardly changes. If we are talking about losses, then x_0 has little effect.

Decreasing the conductance g_0, impedance y_0 does not change considerably, since the main role is played by b_0. As a result $\dot{Z}_\lambda$ and $\dot{\gamma}$ do not change much, which results that modules of a_1 and a_2 are even closer than in a basic case, so the effect is felt by h' and less felt by a'; as a result ΔP at I=0 diminishes considerably and ΔP at I=300 – only slightly.

II. For some LC the losses of TPL or single CLa or CLb were calculated. Phase wire of CLa is 2AC240/32: r_{0a}=6.05e-5; x_{0a}=3.2e-4; g_{0a}=4.132e-11; b_{0a}=3.5e-9; l_a=300 km; phase wire of CLb is 2AC300/39: r_{0b}=4.9e-5; x_{0b}=3.2e-4; g_{0b}=2.984e-11; b_{0b}=3.5e-9; l_b=200 km.

The calculation was carried out for 9 options of initial conditions: 1) s=1; q=1; 2) s=1; q_l=0.7; 3) s=1; q_m=1.3; 4) s=0.8; w=-1; q=1; 5) s=0.8; w=-1; q_l=0.7; 6) s=0.8; w=-1; q_m=1.3; 7) s=0.8; w=1; q=1; 8) s=0.8; w=1; q_l=0.7; 9) s=0.8; w=1; q_m=1.3. Options 1) – 3) are made with active LC (s=1); options 4) – 6) – with inductive LC (w=-1), options 7) – 9) – with capacitive LC (w=1). Losses $\Delta\dot{S}$ were calculted in ordinary way to show real and imaginary component. The real component was checked by AD.

In order not to abuse numbers, Table 2 shows options 1), 2), 3), 4). I_A is BC when in operation is TPL or single CLa. I_{Ad}= $I_A$when q=1; I_{Ad}= $I_{Al} = 0{,}7I_A$; I_{Ad}= $I_{Am} = 1.3I_A$; $\Delta\dot{S}_{Ap}$ is power loss of TPL at LC I_A, $\Delta\dot{S}_{Aa}$ – of single Cla at LC I_A. $\Delta\Pi_{Al} = \Delta P_{Ap} - \Delta P_{Aa}$

is discrepancy of active losses of TPL and single CLa at a current $I_{Ad} = I_{Al}$; $\mathit{\Delta\Pi}_{Am} = \Delta P_{Aa} - \Delta P_{Ap}$ is discrepancy of active losses of single CLa and TPL at current $I_{Ad} = I_{Am}$. The CLa with more resistance than CLb takes less BC. When *w*=1, the CLa takes still less BC than CLb.

Table 2. Results of Calculating Currents and Power Losses in TPL and Single Line

	s=1; q=1	s=1; q_l=0.7	s=1; q_m=1.3	s=0.8; w= -1; q=1
I_A	141.3	141.3	141.3	180.9
I_{Ad}	141.3	98.91	183.7	180.9
$\Delta\dot{S}_{Ap}$	1.037e6-6.032e7i	9.711e5-6.061e7i	1.126e6-5.99e7i	9.047e5-6.258e7i
$\Delta\dot{S}_{Aa}$	1.037e6-3.421e7i	8.541e5-3.506e7i	1.284e6-3.319e7i	9.047e5-3.718e7i
$\mathit{\Delta\Pi}_{Al}$	3.725e-8≈0	1.17e5	-1.576e5	0
$\mathit{\Delta\Pi}_{Am}$	-3.725e-8≈0	-1.17e5	1.576e5	0
I_B	437.7	437.7	437.7	374.9
I_{Bd}	437.7	306.4	569	374.9
$\Delta\dot{S}_{Bp}$	2.133e6-5.46e7i	1.511e6-5.793e7i	2.972e6-5.001e7i	1.363e6-6.184e7i
$\Delta\dot{S}_{Bb}$	2.133e6-1.324e7i	1.186e6-1.92e7i	3.413e6-5.248e6i	1.363e6-2.008e7i
$\mathit{\Delta\Pi}_{Bl}$	-2.98e-8≈0	3.255e5	-4.416e5	-1.49e-8≈0
$\mathit{\Delta\Pi}_{Bm}$	2.98e-8≈0	-3.255e5	4.416e5	1.49e-8≈0
Identical lines: r_0=6.05e-5; x_0=3.2e-4; g_0=8.264e-11; b_0=3.5e-9; l=300 km				
I_A	276.5	276.5	276.5	276.5
I_{Ad}	276.5	193.6	359.5	276.5
$\Delta\dot{S}_{Ap}$	2.044e6-6.87e7i	1.693e6-7.018e7i	2.516e6-6.661e6	1.493e6-7.468e7i
$\Delta\dot{S}_{Aa}$	2.044e6-2.967e7i	1.35e6-3.289e7i	2.98e6-2.522e7i	1.493e6-3.565e7i
$\mathit{\Delta\Pi}_{Al}$	2.98e-8≈0	3.43e5	-4.641e5	2.236e-8≈0
$\mathit{\Delta\Pi}_{Am}$	-2.98e-8≈0	-3.43e5	4.641e5	-2.236e-8≈0

With active LCs (*s*=1) BCs are I_A= 141.3, I_B=437.4. When LC contains inductive current (*s*=0.8, *w*=-1) then I_A=180.9, I_b= 374.9. With the same modulus but capacitive LC (*s*=0.8, *w*=1) – I_A=111.1, I_B=509.1.

Let us recall that losses at BC are losses when q=1 i.e. $real(\Delta\dot{S}_{Ap}) = real(\Delta\dot{S}_{Aa}) = \Delta P_A$. Observing Table 2 and the rest five calculated cases, the ratio between discrepancies $\mathit{\Delta}\Pi$ and the losses ΔP at BC is obtained: with an active LC (s=1) $\mathit{\Delta\Pi}_{Al}/\mathit{\Delta}P_A$=0.11; $\mathit{\Delta\Pi}_{Am}/\mathit{\Delta}P_A$=0.15; $\mathit{\Delta\Pi}_{Bl}/\mathit{\Delta}P_B$=0.15; $\mathit{\Delta\Pi}_{Bm}/\mathit{\Delta}P_B$=0.21; with inductive LC (*s*=0.8, *w*=-1) $\mathit{\Delta\Pi}_{Al}/\mathit{\Delta}P_A$=0.16; $\mathit{\Delta\Pi}_{Am}/\mathit{\Delta}P_A$=0.24; $\mathit{\Delta\Pi}_{Bl}/\mathit{\Delta}P_B$=0.21; $\mathit{\Delta\Pi}_{Bm}/\mathit{\Delta}P_B$=0.27; with capacitive LC (*s*=0.8, *w*=1) $\mathit{\Delta\Pi}_{Al}/\mathit{\Delta}P_A$=0.09; $\mathit{\Delta\Pi}_{Am}/\mathit{\Delta}P_A$=0.11; $\mathit{\Delta\Pi}_{Bl}/\mathit{\Delta}P_B$=0.12; $\mathit{\Delta\Pi}_{Bm}/\mathit{\Delta}P_B$=0.17.

For identical lines with Cla parameters those figures are: $\mathit{\Delta\Pi}_{Al}/\mathit{\Delta}P_A$=0.17; $\mathit{\Delta\Pi}_{Am}/\mathit{\Delta}P_A$=0.23. The discrepancy is more with the greater LC deviation from BC: for $q_l = 0.5$, $\mathit{\Delta\Pi}_{Al}/\mathit{\Delta}P_A$=0.25; for $q_m = 1.5$, $\mathit{\Delta\Pi}_{Am}/\mathit{\Delta}P_A$=0.41; for $q_m = 2$, $\mathit{\Delta\Pi}_{Am}/\mathit{\Delta}P_A$=0.99.

With significant LC deviations from BC, it is necessary to pay attention to the losses.

In cable lines, these issues manifest themselves with less voltages and distances.

6. CONCLUSIONS

1. Active power losses in transmission lines, with at least one series (r_0, x_0) and one parallel (g_0, b_0), distributed parameter taken into account, can be alternatively determined as trinomial of the modulus of the load current at the end of the line with the given angle φ between voltage and current. Losses consist of three terms: one term is proportional to the square modulus, the second term is proportional to the modulus and dependent on angle φ and the third term is independent of the load current. The proportionality coefficients and the third term are functions of the line parameters.

   These lines operating in parallel can be characterised by a boundary current such that one line operating at a load below boundary current has less losses than two lines operating in parallel at the same load and vice versa. If two lines are identical, the formula of boundary current is short and not dependent on angle φ.
2. An alternative determination of losses allows you to identify the influence of each parameter and to derive the expression for boundary current.
3. Specific resistance r_0 has the greatest influence on losses since fading decrement α is almost proportional to it; specific reactance x_0 has almost no effect; conductance g_0 affects mainly at low load currents; the decrease in susceptance b_0 does not lead to a strong decrease in losses, since other quantities are influenced here.
4. In medium lines, a simple determination of active losses already at a load current over twice the capacitive line current has an error under -2 %. For normal line load currents, the accuracy of simple loss determination is sufficient. By simple determination, the boundary current of identical lines over the entire range of medium line lengths is ≈86 % of the true value.
5. Losses from inadequate operation of parallel lines can reach a significant amount compared to minimal losses.

ACKNOWLEDGEMENTS

The research has been supported by “Future-Proof Development of the Latvian Power System in an ntegrated Europe (FutureProof)”, project No. VPP-EM-INFRA-2018/1-0005.

REFERENCES

1. Jiguparmar. (2019). *Total Losses in Power Distribution and Transmission Lines.* Available at www.electrical-engineering-portal-com/total-losses-in-power-distribution-and-transmi...
2. Electrical Power Energy. (2019). *What are the Losses of Transmission Line?* Available at www.electricalpowerenergy.com/2019/03/losses-of-transmission-line
3. Benedict, E., Collins, T., Gotham, D., Hoffman, S., Karipides, D., Pekarek, S., & Ramabhadran, R. (1992). *Losses in Electrical Power Systems.* Purdue School of Electrical Engineering. ECE Technical Reports. Available at https://docs.lib.purdue.edu/ ecetr/226.

4. Nguyen, M.H., & Saha, T. K. (2009). Power Loss Evaluations for Long Distance Transmission Lines. In: *Australian Geothermal Conference 2009* (pp. 317 –312), 11–13 November 2009. The University of Queensland, St. Lucia, Brisbane – QLD Australia. Available at https://www.geothermal-energy.org/ pdf/IGAstandard/…
5. Anyaka, B. O., & Olawoore, O. I. (2014). Minimization of Power Losses in Transmission Lines. *Computer Science. IOSR Journal of Electrical and Electronics Engineering.* Available at https://www.semanticscholar.org/ paper//minimization
6. Kenge, A.V., Kulkarni, S.S., & Patil, S.S. (2014). Increase in power carrying capacity of transmission line by using high ampacity conductors. In: *The 3rd IRF International Conference* (pp. 26–29), 2 March 2014. Pune: Sandip Institute of Engineering and Management.
7. Beryozkina, S., & Sauhats, A. (2015). Research and simulation of overhead power line uprating using advanced conductors. In: *International Scientific Conference on Power and Electrical Engineering of Riga Technical University* (pp. 69–72), 14 October 2015, Riga, Latvia. doi: 10.1109/RTUCON.2015.734161.
8. Sauhats, A., Petricenko, L., Beryozkina, S., & Jankovskis, N. (2016). Stochastic Planning of Distribution Lines. In: *Conference on the European Energy Market* (EEM 2016), (pp. 895–899), 6–9 June 2016. Porto, Portugal. doi:10.1109/EEM.2016.7521349.
9. Schlabbah, J., Rofalski, K-H. (2008). *Power System Engineering* (pp. 159–171). Weinheim: WILEY-VCH publishing house GmbH & Co. KgaA.
10. Global Market Monitor. (2020). *Japan Flexible AC Transmission Systems (FACTS).* Market Report. Available at https://www.globalmarketmonitor.com/reports/438855…
11. Survilo, J. (2019). Influence of power line parameters on their properties. In: *International Scientific Conference on Power and Electrical Engineering of Riga Technical University* (pp. 17–22), 14 October 2019. Piscataway: IEEE, 2019. doi: 10.1109/RTUCON48111.2019.8982262..
12. Quora. (2016). *Why are Electrical Lines Connected in Parallel? – Quora.* Available at https://www.quora.com/ why-are-electrical-lines-connected-in-parallel.
13. Al-Shaalan, A. M. (2019). Reliability Evaluation of Power Systems. *Systems Reliability.* DOI:10.5772/intechopen.85571.
14. Sauhats, A., Kovalenko, S., & Zicmane, I. (2018). Controlled load as one of the ways of providing savings in the electricity market. In: *2018 IEEE Conference on Environment and Electrical Engineering* (pp. 153–165), 12–15 June 2018. Piscataway, Palermo, Italy. doi: 10.1109/EEEIC.2018.
15. Tziouvaras, D.A., Altuve, H.J., & Calero, F. (2014). Protecting mutually coupled transmission lines: Challenges and solutions. In: *68th Annual Georgia Tech Protective Relaying Conference*, 30 April–2 May 2014. Atlanta Georgia. Available at http://dx.doi.org/ 10.1109/CPRE.2014.6798993.
16. *Quora. (2017). What are Double Circuit Transmission Lines?-Quora. Available at* https://www.quorq.com/ *what-are-double-circuit-transmission-lines*
17. Hase, Y. (2008). *Handbook of Power System Engineering*. England: John Wiley & Sons Ltd.
18. Calero, F. (2015). *Mutual Impedance in Parallel Lines – Protective Relaying and Fault Location Considerations.* Schweizer Engineering Laboratories, Inc. Available at https://selinc.com/api/download/3488.
19. *May, T., & Yeap, Y. (2016)*. Comparative Evaluation of Power Loss in HVAC and HVDC Transmission System. In: *TENCON 2016-2016 IEEE Region 10 Conference*, 22–26 November 2016. Available at https://researchgate.net/publication/313587347_Comparative_evaluation_of_po...
20. *PJM. (2013). Basics of Electricity Power Flow on AC Transmission Lines.* Available at https://www.pjm.com/-/media/training/nerc-certifications/trans-exam-materials/bet/bet-I...

21. Electrical Engineering Portal. (2018). *Losses in the Power Transmission System and Short, Medium and Long Line Model Analysis.* Transformers/transmission and Distribution. Available at https://electrical-engineering-portal.com/losses-power-transmission- system
22. Anumaka, M. (2012). Analysis of Technical Losses in Electrical Power System (Nigerian 330 kV Network as a case study). *IJRRAS, 12* (2), 320–327. Available at https://www.researchgate.net/publication/294260716...
23. Vanags, A. (2007). *Electrical networks and systems, I.* Riga: RTU.
24. Vanags, A., & Krishans, Z. (2005). *Electrical networks and systems, II.* Riga: RTU.
25. Wikipedia. (n.d.). *Trinomial.* Available at https://en.wikipedia.org/wiki/Trinomial
26. MathWorld. (n.d.). *Hyperbolic Functions.* Available at http://mathworld.wolfram.com/HyperbolicFunctions.html

sciendo

LATVIAN JOURNAL OF PHYSICS
AND TECHNICAL SCIENCES
2022, N 3

DOI: 10.2478/lpts-2022-0018

TECHNOLOGICAL ASSURANCE OF TI-6AL-4V PARTS PRODUCED BY ADDITIVE MANUFACTURING USING SELECTIVE METAL LASER SINTERING

A. Kromanis, A. Vevers

Metal 3d Ltd.
15a Mukusalas Str., Riga, LV-1024, LATVIA
E-mail: info@metal3d.lv

The research relates to a technological assurance of Ti6-Al-4V parts produced by additive manufacturing (AM) by means of a metal laser sintering, especially by a fibre laser 3D printer. The influence of technological parameters such as layer thickness, hatch spacing, laser travel speed and laser power have been analysed as well as the influence of thermal treatment as a post processing method has been studied. Technological parameters in combination with a thermal treatment present a challenge in order to manufacture satisfactory products in terms of mechanical properties. The research guides through different phases of experiments to distinguish the best technological parameters. The following research may be used for further investigation of technological assurance for additive manufacturable parts as well as forms the springboard for further research in development of new titanium composites using additive manufacturing methods.

Keywords: 3D printing, additive manufacturing, grade 5, tensile strength, titanium, Ti-6Al-4V.

1. INTRODUCTION

Ti-6Al-4V alloy, known as Ti64 and Ti-6Al-4V Grade 5 and Ti-6Al-4V Grade 23, is a titanium alloy with high strength, low density, high fracture toughness, resistant to corrosion and suitable for biomedical applications, e.g., biocompatible [1], [2]. Various additive manufacturing techniques may be implemented for forming Ti-6Al-4V parts. Three mostly developed techniques are directed energy deposition

(DED), selective laser melting (SLM) and electron beam melting (EBM) [3]. DED, SLM and EBM are powder based AM techniques. Nevertheless, it does not exclude other AM techniques such as wire based AM techniques where instead of a powder material as a feed material a wire-type material is used. It may be certainly pointed out that a wire based AM techniques are obtaining certain attention in the field of AM manufacturing of Ti-6Al-4V [4]–[6]. In addition, the AM process by itself involves complex multi-physics, non-equilibrium phenomena, which are affected by a group of process parameters, such as power, scan speed, scan strategy, layer height, hatch spacing, etc. [3]. In the present research, an SLM technique has been used and the influence of the process variables such as layer thickness, hatch spacing, travel speed and laser power has been studied. One of the main considerations or questions in the AM is if identical or improved material properties can be achieved as compared to the parts made by traditional manufacturing methods. Mechanical properties, particularly tensile strength and elongation, are the mostly used parameters to evaluate the built Ti-6Al-4V part. Hence, the influence of the process variables on a tensile strength and elongation of the 3D printed parts has been researched.

2. MATERIALS FOR ADDITIVE MANUFACTURING

Reseacrh was performed on Ti6-Al4-V powder having chemical composition according to ASTM F2924-14 (see Table 1) [10]. Powder size was in the range of 20 to 50 micrometres, which is the average diameter of the powder particle within the powder. Certain amount, but not significant amount of particles has a diameter exceeding the aforementioned range.

Table 1. Chemical Composition (Nominal), wt%, for Ti6Al4V (Grade 5) according to ASTM F2924-14

Ti	**Al**	**V**	**Fe**	**O**	**C**	**N**	**H**	**Y**	**Others, each**	**Other, total**
Balance	5.50–6.75	3.5–4.5	<0.3	<0.20	<0.08	<0.05	<0.015	<0.005	<0.10	<0.40

The main concern for parts made by additive manufacturing is their compliance with physical and mechanical properties against the standard and parts made by conventional manufacturing methods such as casting, rolling, etc. AM allows for the creation of parts with complex shapes, but the process itself inherits that the part is made in a line by line and layer by layer manner. This step-by-step approach or building process brings uncertainty on uniformity of the created AM part. Therefore, a lot of attention is paid to post-processing and quality control of the AM parts. Table 2 provides information on physical and mechanical properties for Ti-6Al-4V (Grade 5), which serves as a benchmark to be reached by AM parts. Hence, the main aim of the research has been to provide a set of technological parametrs which will allow to manufacture AM parts that comply with the physical and mechanical properties of Ti-6Al-4V (Grade 5) made by conventional manufacturing methods. If it is proved that it is possible to obtain the same physical and mechanical properties with the AM as it is with conventional manufacturing methods, then further implementation of AM technologies will be possible for titanium alloys, especially for Ti-6Al-4V alloy.

Table 2. Physical and Mechanical Properties for Ti-6Al-4V (Grade 5)

	Young's modulus, GPa	**Shear modulus, GPa**	**Bulk modulus, GPa**	**Poisson's ratio**	**Yield stress, MPa (tensile)**	**Ultimate stress, MPa (tensile)**	**Uniform elongation, %**
Min	104	40	96.8	0.31	880	900	5
Max	113	45	153	0.37	920	950	18

2.1. 3D Printer for SML

The 3D printer used for the experiments of the research was Aurora Labs Titanium Pro S1 machine. This 3D printer utilises powder bed fusion-laser process. Moreover, this Aurora Labs Titanium Pro S1 machine was modified from its original by replacement of the laser. Aurora Labs Titanium Pro S1 laser system was replaced with MaxPhotonics 200W-300L fiber laser. Maximum laser power of the system is 250W. Focal distance is 75 mm. Laser spot size is 90 micrometres. Build envelope is 200x200x500 mm. Layer thickness can be varied from 30 to 100 micrometres. Laser travel speed can be adjusted in the range from 0 to 100 mm/s. Powder extruder was modified to inject powder from all three extruders in a zone in front of recoater blade. This modification allows maintaining time for powder extrusion for each layer under 30 seconds, thus increasing an overall printing speed.

2.2. Technological Parameters for SLM

Experiments of the research included multiple sequential steps as shown in Fig. 1. The first step includes definition of the experimental parameters. The 3D printing is defined by the following parameters: a layer thickness; a hatch spacing; a laser travel speed; and a laser power. The AM part is built by selectively moving a laser beam in a line by line path. The spacing between these lines is defined as a hatch spacing and is measured in mm. When the laser beam completes all paths within one layer, the next layer of the powder is applied, and the selective laser beam movement is repeated for this next layer of the material. The thickness of one such a layer is defined as layer thickness and is measured in mm. The laser beam moves by predefined path at a certain pre-set speed. This speed is defined as a laser travel speed and is measured in m/s. The laser beam radius is 0.09 mm. The laser beam radius is a constant parameter and cannot be adaptively controlled. Therefore, its further influence on technological assurance was not studied. The interrelationship of aforementioned parameters can be summarised by such a parameter as an energy density E (in J/mm3). Energy density is the absorbed energy density and can be calculated using the following equation [3]:

$$E=\propto\cdot Pv\cdot h\cdot t, \tag{1}$$

where P is the laser power (W), v is the scan speed (mm/s), h is the hatch spacing (mm), t is the layer thickness (mm) and α is absorptivity. Regarding absorptivity it is known that, under conditions associated with laser powder additive manufacturing, absorptivity values can vary greatly, and differ from both powder-layer measurements and liquid metal estimates from the literature [9]. As the absorptivity parameter by itself may not be adaptively changed and at the same time it can be considered as part of laser power describing parameter, for given experiments the following updated equation was used:

$$E=Pv\cdot h\cdot t. \tag{2}$$

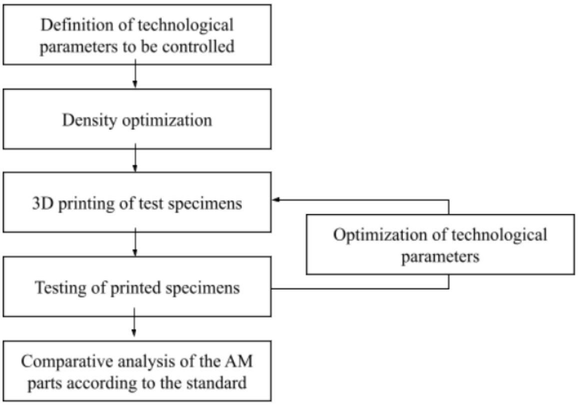

Fig. 1. Block scheme on planning and conducting experiments as well as adjusting technological parameters.

3. DENSITY OPTIMIZATION FOR THE AM PARTS

Density optimization is the first critical step in building additively manufactured parts with high quality and good mechanical properties [10]. Also, other publications [7], [8] suggest that the density optimization is the first and most important step for creation of parts using additive manufacturing techniques. Accordingly, the set of experiments was prepared in order to define the best technological parameters for optimal density. In each set of experiments, five samples were printed as one batch (see Fig. 2). The dimensions of each sample were 10x10x10 mm. Each sample was printed under a different setup of parameters.

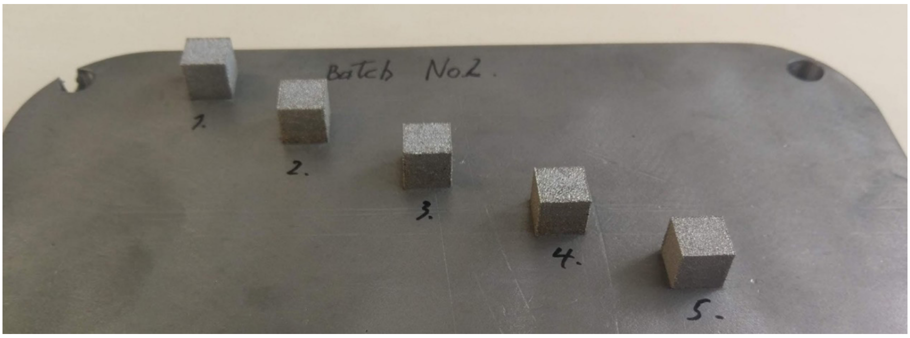

Fig. 2. 3D printed samples for density optimization.

After 3D printing of each batch a material density or porosity was measured. Measurements were performed using optical measurement methods. The setup of parameters and resultant density and porosity are provided in Table 3.

Table 3. Setup of 3D Printing Parameters and Resulting Material Density and Porosity

Sample No.	Layer thickness, mm	Hatch spacing, mm	Travel speed, mm/s	Laser power, W	Energy density, J/mm3	Optically measured porosity, %	Optically measured density, %
1.1	0.05	0.3	100	55	36.7	11	89
1.2	0.05	0.3	100	65	43.3	10	90
1.3	0.05	0.3	100	50	33.3	7	93
1.4	0.05	0.25	100	50	40.0	9	91
1.5	0.05	0.25	100	90	72.0	9	91
2.1	0.05	0.25	90	55	48.9	11	89
2.2	0.05	0.25	90	65	57.8	10	90
2.3	0.05	0.25	90	50	44.4	12	88
2.4	0.05	0.2	90	50	55.6	8	92
2.5	0.05	0.2	90	90	100.0	18	82
3.1	0.08	0.25	80	70	43.8	20	80
3.2	0.08	0.25	80	80	50.0	0.2	99.8
3.3	0.08	0.25	80	90	56.3	7	93
3.4	0.08	0.2	80	80	62.5	18	82
3.5	0.08	0.2	80	90	70.3	2	98
4.1	0.05	0.2	80	50	62.5	14	86
4.2	0.05	0.2	80	60	75.0	8	92
4.3	0.05	0.15	80	50	83.3	2	98
4.4	0.05	0.15	80	55	91.7	2	98
4.5	0.05	0.15	80	80	133.3	2	98
5.1	0.05	0.2	80	90	112.5	2	98
5.2	0.05	0.2	80	100	125.0	0.2	99.8
5.3	0.05	0.15	80	90	150.0	2	98
5.4	0.05	0.15	80	100	166.7	3	97

The density optimization experiments showed that the best performance, e.g., most dense AM part, was achieved using the laser travel speed at 80 mm/s. Results as shown in Table 3 under the higher laser travel speed (90 and 100 mm/s) allowed concluding that too high travel speed did not allow creating a sufficient melting of the powder material forming more porous material. Even an increase in the laser power could not compensate for this lack of density as the laser movement did not allow for sufficient melting. This may be considered a drawback of 3D printing because an increase in the laser power will not allow for a sufficient increase in the laser travel speed, thus increasing overall productivity. Moreover, the material itself, which is Ti6Al4V, has low thermal conductivity, decreasing the effectiveness of laser thermal influence on the material.

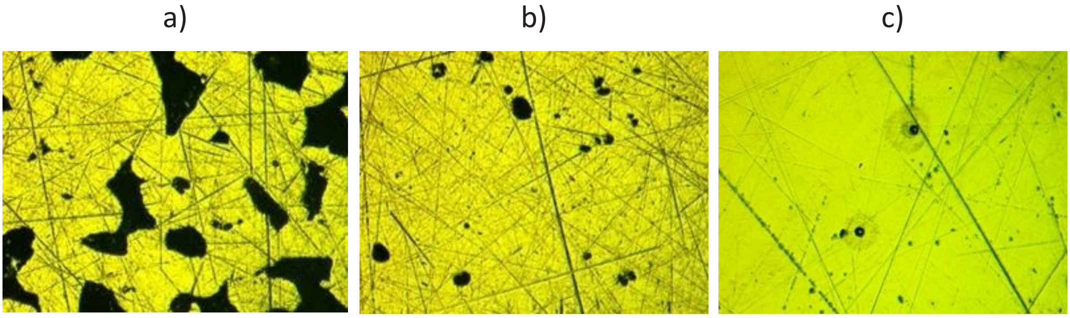

Fig. 3. a) a microstructure of sample No. 3.1 with density of 79.56 %;
b) a microstructure of sample No. 3.5 with a density of 98 %;
c) a microstructure of sample No. 5.2 with density of 99.8 % enlarged by 50x.

Due to this low thermal conductivity of the material, better density was obtained under smaller hatch spacing which was from 0.15 to 0.20 mm. Hatch spacing of 0.25 to 0.3 mm did not provide sufficient results, which was density of the AM part. The layer thickness for density optimization was chosen based on the powder material properties, especially on the average diameter of the particles in the powder material. Powder size is 20–50 micrometres [11], which is an average diameter of the powder particle within the powder. Hence, the minimum layer thickness shall be 0.05 mm. For density optimization, the layer thickness was chosen between 0.05 to 0.08 mm. Results (see Table 3) showed that the layer thickness had least influence on the density. As the layer thickness of 0.05 mm was absolute minimum for given powder material, it was decided to proceed with increased layer thickness. Nevertheless, some experiments were continued with the layer thickness of 0.05 mm (see Table 4) to obtain confirmation that this level of the layer thickness was not the most appropriate one for further increase of mechanical and physical properties of AM parts made of Ti6Al4V powder.

4. EXPERIMENTS ON INCREASING MECHANICAL PROPERTIES OF AM PARTS

Experiments on density optimization provided preliminary results or suggestions on technological parameters suitable for obtaining AM parts with a satisfactory structure. The next step involved a 3D printing of parts in the form of test bones for tensile strength tests. The parts were made in a step-by-step approach. The test specimens were divided in the batches of the specimens. After each 3D print of specimen batch, thermal treatment and tensile strength tests were performed. The obtained results were analysed and technological parameters were adapted in order to produce the next batch of specimens with increased mechanical properties. The following approach is also illustrated in Fig. 1.

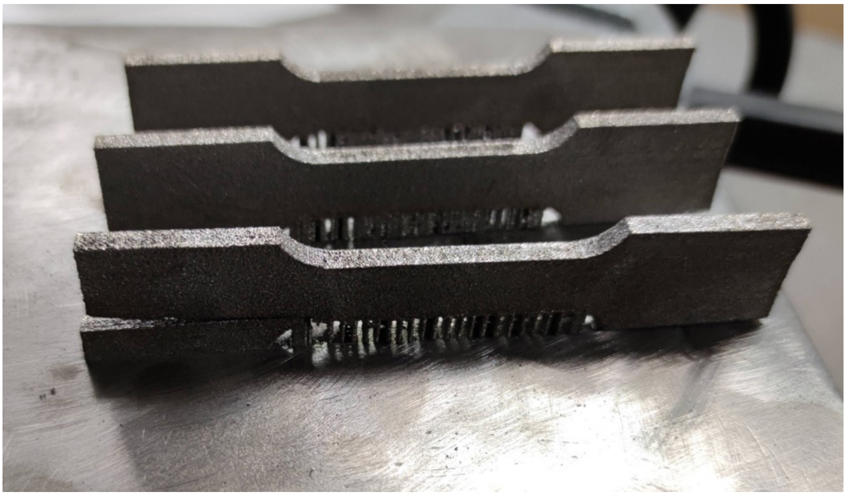

Fig. 4. 3D printed tests specimens comprising supports as well as illustrating a printing defect – delayering in the forefront specimen.

Multiple batches of specimens were printed as shown in Table 4. Each batch comprised three specimens as shown in Fig. 4. Table 4 provides average values of mechanical parameters for each batch.

Table 4. 3D Printing Parameters, Heat Treatment Parameters and Resulting Mechanical Properties of 3D Printed Specimens

Batch No.	Layer thickness, mm	Hatch spacing, mm	Travel speed, mm/s	Laser power, W	Energy density, J/mm3	Heat Treat-ment	Average tensile strength, MPa	Average elonga-tion, A%
Standard	---	---	---	---	---	---	**900-950**	**5-18**
11	0.05	0.25	100	65	52.0		639	0.6
12	0.08	0.25	100	80	40.0		558	0.6
13	0.08	0.15	80	75	78.1		497	0.7
14	0.08	0.15	80	75	78.1	1	329	0.5
15	0.07	0.15	80	70	83.3	2	382	0.4
16	0.07	0.15	80	70	83.3		603	0.6
17	0.07	0.1	80	70	125.0		610	0.6
18	0.07	0.1	80	70	125.0	2	632	0.7
19	0.07	0.1	80	70	125.0	3	850	2.9
20*	0.07	0.1	80	80	142.9	3	1030	7.8

** Specimens machined out of 3D printed stock of material*

Various heat treatment strategies were chosen based on studies of prior literature. Heat treatment strategy No. 1 involved a heat treatment of the sample in the furnace for 1 hour up to 1223 ° K which was followed by cooling down the sample within the same furnace – furnace cooling. Heat treatment strategy No. 2 involved a heat treatment of the sample in the furnace for 1 hour up to 1223 ° K which was followed by cooling down the sample outside the furnace – air cooling. The sample was subject to further heat treatment (stress relief) in the same furnace for 4 hours up to 813 ° K, which was continued by cooling down the sample in the air – air cooling. Heat treatment strategy No. 3 involved a heat treatment of the sample in the furnace for 1 hour up to 1223 ° K in inert environment which was followed by cooling down the sample within the furnace.

Tensile strength tests were performed on Zwick/Roell Z600 testing machine under displacement control at a rate of 1.5 mm/min. This speed approximately corresponds to strain rate of 2.7 %/min. MacroXtens extensometer from Zwick was used for strain measurement (see Fig. 5). The gage length of the extensometer was set to 17 mm.

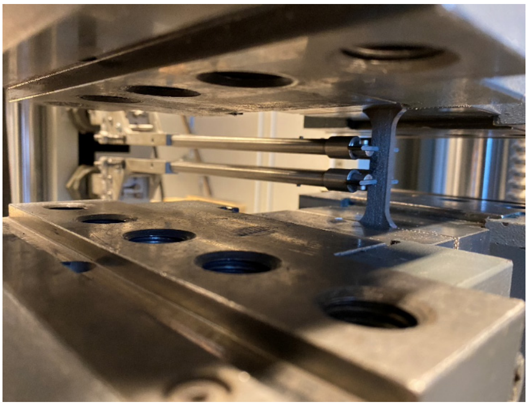

Fig. 5. Tensile strength test setup with an extensometer attached to the test sample.

Elastic modulus was determined in the linear behaviour region. Failure stress and failure strain at failure were determined from the maximum values on the test curves prior to the actual failure.

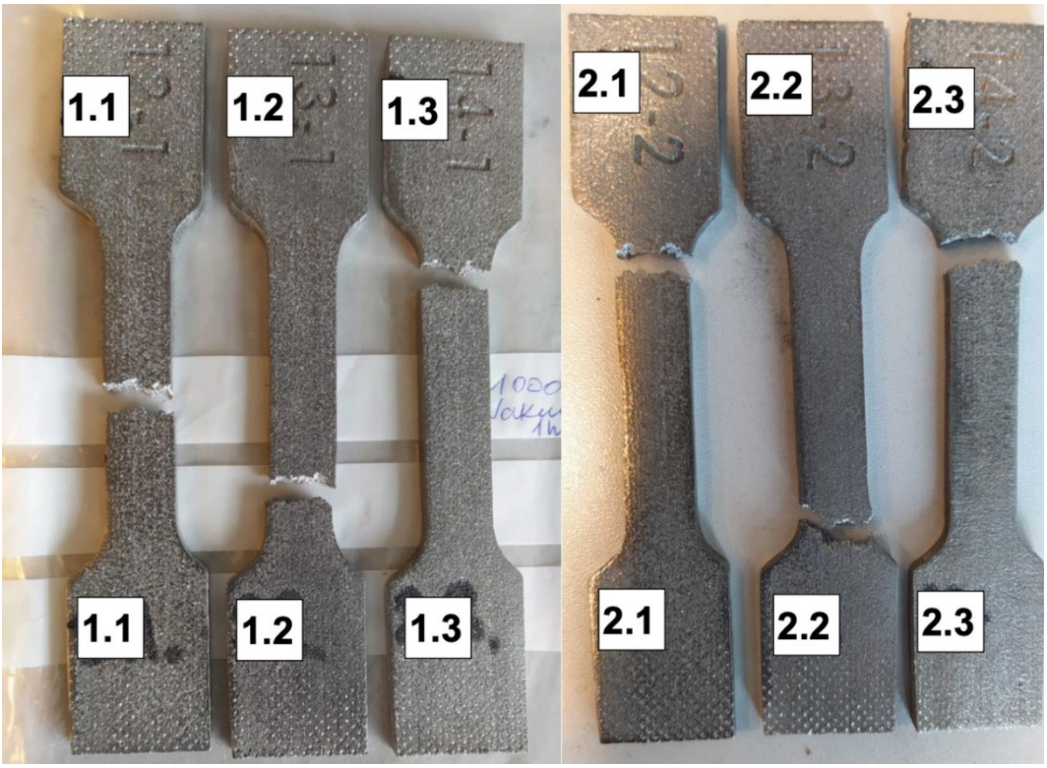

Fig. 6. Specimens after the tensile strength test.

As shown in Fig. 6, for tested samples 17.1 to 17.3 and 19.3 the failure occurred near the grips of the testing machine. Such behaviour is quite rare for standard metallic material samples with rectangular cross-section and a dog-bone shape. The fracture surface shape for samples resembles failure of a brittle anisotropic material. Hence, failure behaviour of these samples can be classified as "brittle". Breakage zone can be seen in Fig. 8. It is well known that brittle materials are prone to failure in the grips of a testing machine.

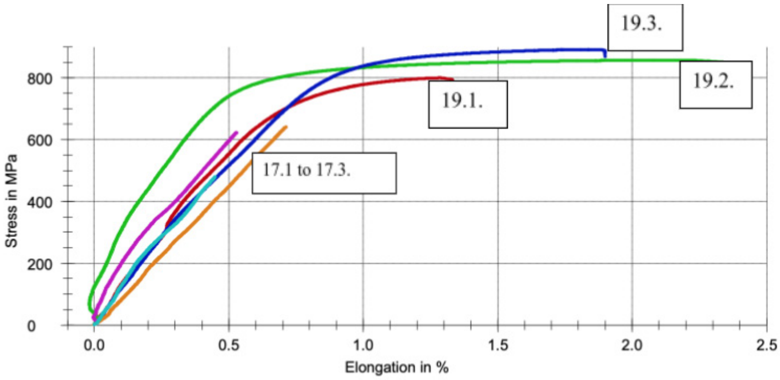

Fig.7. Stress-elongation curve for specimens 1.1 to 2.3.

Although the test specimen length was relatively short, the used macro extensometer was suitable for strain measurements. Some small oscillations of strain data were visible on the test curves, most probably due to some minor sliding from the grips of the testing machine. However, this should not have any effect on the final results (See. Fig. 7 for tensile test results from batch No. 17 and Batch No. 19).

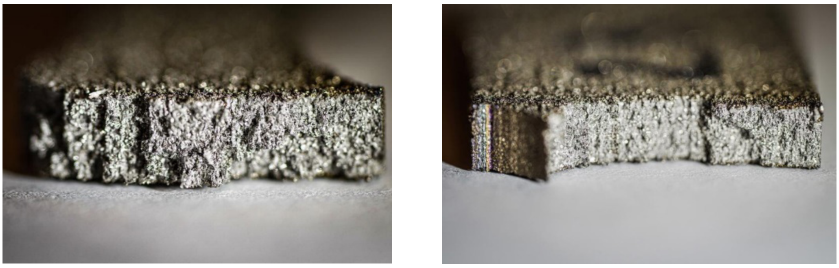

Fig. 8. Zoomed-in photos of broken test samples illustrating the breakage line and surfaces.

5. CONCLUSIONS

The energy density is defined by such laser parameters as layer thickness, hatch spacing, laser travel speed and laser power. Accordingly, the energy density influences a microstructure as well as mechanical properties of a 3D printed part. Further increase of mechanical properties of AM parts may be accomplished by thermal treatment, especially by a thermal treatment in an inert environment. The best results on mechanical properties have been obtained by setting a layer thickness at 0.07 mm, hatch at 0.1 mm, laser travel speed at 80 mm/s and laser power at 70 W. Post processing, especially thermal treatment, significantly influences the physical properties of 3D printed parts. The research has proven that thermal treatment shall be performed in an inert environment without presence of oxygen as Ti6Al4V is keen to oxidate.

ACKNOWLEDGEMENTS

Research has been developed within ERDF project 1.1.1.1/19/A/058 “Development and Testing of New Additive Manufacturing Material”.

REFERENCES

1. Donachie, M.J. (2000). *Titanium: A technical guide* (2nd ed.). Ohio: ASM International, Materials Park.
2. Cui, C., Hu, B., Zhao, L., & Liu, S. (2011). Titanium Alloy Production Technology, Market Prospects and Industry Development. *Mater. Des., 32* (3),1684–1691.
3. Liu, S., & Shin, Y.C. (2019). Additive Manufacturing of Ti6Al4V Alloy: A Review. *Materials and Design, 164,* 107552, 1–23.
4. Bermingham, M.J., Nicastro, L., Kent, D., Chen, Y., & Dargusch, M.S. (2018). Optimising the Mechanical Properties of Ti-6Al-4V Components Produced by Wire + Arc Additive Manufacturing with Post-process Heat Treatment. *J. Alloys Compd., 753*, 247–255.
5. Zhang, J., Wang, X., Paddea, S., & Zhang, X. (2016). Fatigue Crack Propagation Behaviour in Wire + Arc Additive Manufactured Ti-6Al-4V: Effects of Microstructure and Residual Stress. *Mater. Des., 90*, 551–561.
6. Hönnige, J.R., Colegrove, P.A., Ahmad, B., Fitzpatrick, M.E., Ganguly, S., Lee, T.L., & Williams, S.W. (2018). Residual Stress and Texture Control in Ti-6Al-4V Wire + Arc Additively Manufactured Intersections by Stress Relief and Rolling. *Mater. Des.*, *150*, 193–205.
7. Murr, L.E., Gaytan, S.M., Ramirez, D.A., Martinez, E., Hernandez, J., Amato, K.N., … & Wicker, R.B. (2012). Metal Fabrication by Additive Manufacturing Using Laser and Electron Beam Melting Technologies. *Journal of Materials Science & Technology*, *28*, 1–14.
8. Herzog, D., Seyda, V., Wycisk, E., & Emmelmann, C. (2016). Additive Manufacturing of Metals. *Acta Materialia, 117,* 371–392.
9. Trapp, J., Rubenchik, A.M., Guss, G., Matthews, M.J. (2017). In Situ Absorptivity Measurements of Metallic Powders during Laser Powder-Bed Fusion Additive Manufacturing. *Applied Materials Today, 9*, 341–349.
10. Wang, Y.M., Kamath, C., Voisin, T., & Li, Z. (2017). Density Optimization, Microstructure and Mechanical Properties of Ti-6Al-4V Manufactured by Laser Powder-Bed-Fusion. *Rapid Prototyping Journal*. Lawrence Livermore National Laboratory, LLNL-JRNL-737675. Available at https://www.osti.gov/pages/servlets/purl/1491650
11. Sandvik Datasheet Osprey. (n.d.). *Ti-6Al-4V Powder for Additive Manufacturing.* Available at https://www.metalpowder.sandvik/siteassets/metal-powder/datasheets/osprey-ti-6al-4v-grade-5-and-grade-23.pdf